Université d'Ottawa · University of Ottawa

Mechanisms Governing the Growth of Self-Assembled Quantum Dots

by

Bruno J. Riel

Thesis
presented to the Faculty of Graduate and Postdoctoral Studies
of the University of Ottawa
in the fulfilment of the thesis requirements
for the degree of

Doctor of Philosophy in Physics

University of Ottawa
Ottawa, Ontario
May, 2002

Abstract

We produced self-assembled quantum dot (QD) samples of InAs on GaAs by molecular beam epitaxy (MBE). With these, we explored growth effects as a function of InAs coverage for three arsenic pressures, and as a function of arsenic pressure at a specific InAs coverage. During growth, the samples were studied using reflection high energy electron diffraction (RHEED). These RHEED measurements were compared to low energy electron diffraction (LEED) measurements. To perform this ex-situ LEED characterisation, some samples were covered with an amorphous arsenic cap. This cap was thermally evaporated producing a clean, non-oxidised surface that was studied using LEED. We obtained non-ambiguous identification of the GaAs (001) surface reconstructions as well as timing information for the 2D to 3D transition during the growth of InAs on GaAs.

Post growth characterisation of two sets of self-assembled QD samples, twelve samples in all, revealed the following: As a function of increasing the arsenic pressure used in QD growth, the photoluminescence (PL) of capped QDs is first redshifted at low arsenic pressures, and then blueshifted at high arsenic pressures. Scanning electron microscopy and atomic force microscopy of uncapped QDs show that as the arsenic pressure increases, the QD density increases while the average QD width and height decrease monotonically; these trends are consistent with the shift in PL for the high arsenic pressure samples, but are inconsistent with the shift in PL for the low pressure samples. This leads us to proposing a mechanism by which QDs may be modified as they are overgrown with capping material. We discuss the effects of adjusting the arsenic pressure on the formation of QDs and the mechanism by which QDs may be modified during capping.

Statement of Originality and Collaborative Aspects of this Work

To the best of my knowledge, the work presented in this thesis is original. Literature searches have revealed that the results contained herein are unique. Publications reporting earlier attempts at addressing similar aspects of the formation of self-assembled quantum dots are reviewed and discussed in the thesis.

The work was carried out at the Institute for Microstructural Sciences of the National Research Council, Canada, and at the Department of Physics of the University of Ottawa. This project was extensive and could not have been carried out by a single researcher. Although the author formulated the experimental protocol, grew the samples by molecular beam epitaxy (MBE), laid out the course of characterisation, and analysed the characterisation data, some measurements were carried out by IMS/NRCC personnel: The photoluminescence (PL) spectra, the atomic force microscopy (AFM) images, and the scanning electron microscopy (SEM) images were acquired by Karin Hinzer[1], Simona Moisa[2] and Jeff Fraser[3] respectively. All other characterisation, reflection high energy electron diffraction (RHEED), low energy electron diffraction (LEED), thermal desorption spectroscopy (TDS) and Auger electron spectroscopy (AES), was performed by the author.

---

[1] Present address: Nortel Networks, Ottawa, Canada K1Y 4H7.
[2] IMS/NRCC, Building M-50, 1200 Montreal Rd, Ottawa, Ontario, K1A 0R6.
[3] *Ibid.*

Acknowledgements

I would like to extend my most profound gratitude to Dr. Peter Piercy who has guided me, not only through my doctoral work, but throughout all my graduate studies. His generosity enabled me to work on this doctoral project, even if it took me away from his lab. It is my hope that this thesis does not represent the end of our collaborative efforts, but a new beginning.

I wish to express my deepest appreciation to Dr. Zbig Wasilewski who, day to day, saw that I continued on the path that would take me to this thesis. He allowed me to gain "hands-on" experience in MBE, but more importantly he saw in me a potential that even I did not see.

I also want to offer sincere thanks to Dr. Simon Fafard who introduced me to quantum dots and communicated to me his intimate knowledge of the field. He shared with me the experimental procedures that were at the core of his success in the production of quantum dots.

I would like to thank Dr. Karin Hinzer, Jeff Fraser and Simona Moisa for performing critical characterisation work and for their encouragement; Dr. Paul Finnie, Dr. Philip Poole, and Dr. Jean Marc Barribeau for the helpful discussions and for their support; Dr. Pawel Hawrylak, Dr. Geof Aers and Dr. Chandre Dharma-wardana for answering my theoretical questions; Dashan Wang for his help in the lab; Dr. John McCaffrey for helping me in getting published; and Dr. Sylvain Raymond for his help and for his friendship.

I also thank all the people at IMS who made going to work feel like going home, Tim Gorjanc, Jennifer Lam, Claudine Allen, Jamie Ramsey, Dan Pak, Martha Tomlinson, Andrew Bezinger, Charles Lacelle, Dr. Sylvain Charbonneau, Dr. Robin Williams, and Dr. Margaret Buchanan.

A special word of thanks to Dr. James Gupta: He contributed to my work above and beyond the call of duty, he read many passages in this thesis and suggested considerable improvements. I thank him for his encouragement and his friendship.

I thank Aiguo Cai for his support and encouragement, for taking my mind off my work and into China when I needed a break, and for being a friend who became family.

Finally I would like to thank Karin and both our families. Not only did Karin actively participate in this work, she gave me the support that I needed to complete this long journey. She and I thank our families for understanding when our path kept us away from theirs, and for supporting and encouraging us all along the way.

À Karin

Table of Contents

List of Abbreviations

AFM	atomic force microscopy
AES	auger electron spectroscopy
CBO	conduction band offset
BO	band offset
IMS/NRCC	Institute for Microstructural Sciences of the National Research Council Canada
IDL	incorporation-diffusion length
LEED	low energy electron diffraction
MBE	molecular beam epitaxy
ML	monolayer
PL	photoluminescence
QD	quantum dot
QDs	quantum dots
RHEED	reflection high energy electron diffraction
SEM	scanning electron microscopy
SK	Stranski-Krastanov
STM	scanning tunnelling microscopy
TEM	transmission electron microscopy
TDS	thermal desorption spectroscopy
VBO	valence band offset
WL	wetting layer

List of Figures

1 Introduction

After the general introduction provided by Chapter 1, Chapter 2 presents the materials used in our growth experiments, InAs and GaAs, and a model describing an InAs quantum dot imbedded in GaAs. Chapter 3 then presents the growth theory relevant to the fabrication of self-assembled quantum dots. In Chapter 4, we present the control parameters used in the growth of such self-assembled quantum dots. We then go on to review the effects of the group V pressure, including the concept of adatom incorporation-diffusion length. We also review the effects of overgrowing quantum dots. In Chapter 5, we present molecular beam epitaxy (MBE), including a description of the reactor used to grow our samples, and the growth procedure used to produce our samples. In Chapter 6, we present low energy electron diffraction (LEED) and reflection high energy electron diffraction (RHEED) characterisation of the surfaces observable during these growths. We present together the physical principles behind LEED and RHEED, and the measurements that were obtained with both techniques. In Chapters 7 and 8, we present the characterisation measurements of the two sets of samples that we produced to study the effects of the arsenic pressure on the formation of quantum dots. Here also, we present the principles behind the techniques along with the measurements that were obtained; these techniques include photoluminescence (PL), scanning electron microscopy (SEM) and atomic force microscopy (AFM). Finally, in Chapter 9, we discuss the results presented in Chapters 7 and 8, considering kinetic processes involved in the formation of the quantum dots, as well as the modification of the quantum dots during their overgrowth with capping material.

In this first chapter, we provide a very general context for the subject matter presented in the rest of the thesis. We first give a brief overview of the fabrication of quantum-confinement heterostructures in general, and quantum dots specifically. This includes both technical aspects of their fabrication as well as historical commentary. We then give some examples of the applications of such structures that drive quantum dot research. These examples will include computing and memory devices, as well as quantum-dot based lasers used as light sources in telecommunications.

1.1 A Brief Overview of the Fabrication of Quantum-Confinement Heterostructures

In the late 1960's, Alfred Y. Cho and John Arthur of Bell Labs developed a technique known as Molecular Beam Epitaxy (MBE) [1]. The basic principle of MBE consists in directing the co-evaporation of epitaxial constituent molecular species onto a substrate which is maintained at a controlled temperature. This is performed in ultra pure conditions; excepting the desired constituent molecular fluxes, the MBE system is maintained at ultra high vacuum. This is done in order to minimise the partial pressure of unwanted species and to ensure the collision-free travel of the molecular beams from the heated sources to the substrate surface where they form a high purity epitaxial film. The epitaxial growth occurs in two steps: First, the incident atoms stick to the crystal surface, and then they move on the surface to the point of incorporation at a step edge or an island. A slow growth rate (~1 μm/h) ensures the dissociation and migration of the impinging species on the crystal surface without formation of defects. In this way, atomically thin layers of compound semiconductor crystals can be grown on the surface of bulk crystal substrates. If these epitaxial layers are not overly dissimilar, either chemically or crystallographically to the substrate, the deposited layers

will form a single crystal structure called an epitaxial wafer. Materials grown by MBE have been used in the research of compound semiconductors, such as gallium arsenides, indium phosphides, nitrides, silicon-germanium, silicon-carbide and other advanced materials.

MBE has become a key tool for the production of the base components for the manufacture of many electronic and optoelectronic semiconductor devices. The engineering of band structures of junction semiconductors has proven very fruitful; transistors are the cornerstone of the high-tech world. MBE-grown epitaxial wafers are used for the mass production of devices such as heterojunction bipolar transistors (HBT), metal semiconductor field effect transistors (MESFET), pseudomorphic and high electron mobility transistor (PHEMT), and lasers. The applications of such devices range from high-speed optical fibre networks and wireless communications, to computers, reaching even into mass market consumer electronics such as cellular telephones and DVD players.

If an epitaxial wafer comprises a region of lower bandgap bordered on either side by material of higher bandgap, thereby defining a potential well, it will confine charge carriers within the region of lower bandgap. In this manner, charge carriers can be confined in one, two or three dimensions. If the confinement region is of a size comparable to the de Broglie wavelength of the charge carriers, such structures are then respectively referred to as 2D, 1D or 0D structures. The more evocative descriptions of these low dimensional structures: *quantum wells*, *quantum wires*, and *quantum dots* (or sometimes *quantum boxes*), depicted in Figure 1, are perhaps more intuitively meaningful. These three types of structures can be categorised as quantum-confinement heterostructures, and the materials used in their fabrication are combinations of elements from row IV, III and V, or II and VI of the periodic table.

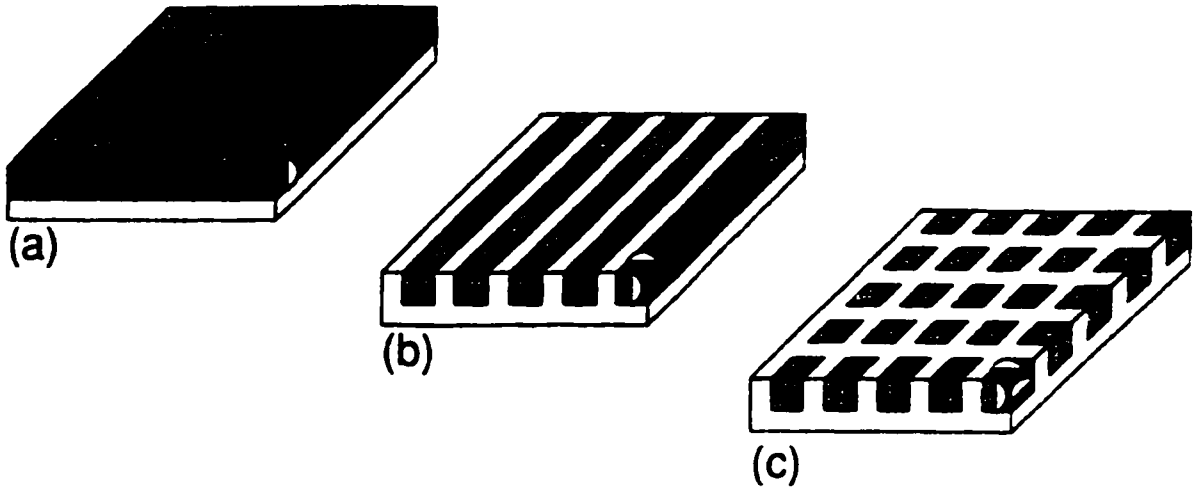

Figure 1. Schematic representation of a) quantum wells, b) quantum wires and c) quantum dots.

Quantum wells are the most straightforward of confinement structures to produce. This is done by growing alternating epitaxial layers of different materials forming, in the growth direction, a bandgap structure as described above. Quantum dots, as well as quantum wires, on the other hand cannot be produced by such a layerwise approach. Microfabrication techniques involving lithography and etching can be used. Quantum dots can be produced by "cutting up" quantum well structures into small pillars, or by "electromagnetic confinement," which involves the deposition of contacts on a quantum well structure for the application of electrical potentials. However, the use of strain-induced island formation present in some epitaxial systems allows for the production of high quality quantum dots through two growth modes: Volmer-Weber and Stranski-Krastanow [2]. Of all the methods for producing 0D structures in semiconductors, this self-assembling of quantum dots during epitaxial growth has arguably proven to be the most successful. This process of quantum dot formation is due to the relaxation of strain energy in non-latticed matched systems such as InAs grown on GaAs. We shall discuss these two compounds as well as the topic of self-assembly in the

following chapter. However they are produced, quantum dots have discrete energy levels. We shall return to this point in Chapter 2 and we shall discuss strain-induced island formation in Chapter 3.

The earliest report of three-dimensional growth of InAs/GaAs we have found in our literature searches dates back to 1985 and was authored by Goldstein, Glas, Marzin, Charasse and Le Roux of the *Centre National d'Etudes des Telecommunications*, Paris, France [3]. Using RHEED observations during MBE, they observed a "... transition from the 2D to a three-dimensional growth (3D) with island formation under arsenic rich-conditions." There are older reports of InAs growth on GaAs in which the 3D growth mode is either observed but not identified as such, or in which the results of the 3D growth are perceived as undesirable. Schaffer, Lind, Kowalczyk and Grant of the *Rockwell International Science Center*, California, USA in a report published in 1983 [4], comment that "... appropriate nucleation conditions (for 2D surface morphology) are those that lead to the (4×2) indium stabilised surface reconstruction, and that (...) the (2×4) arsenic stabilized InAs(100) results in films with (...) poor surface morphologies." The study of InAs/GaAs self-assembled quantum dots as something interesting from the point of view of either fundamental or applied physics did not come until some years later. Leonard, Krishnamurthy, Reaves, Denbaars and Petroff of the *Materials Department and QUEST* at the University of California, Santa Barbara, California, USA, in 1993 report [5], "... unambiguously demonstrate photoluminescence at 1.2 eV from these islands by comparing samples with and without dots."

The properties of low dimensional structures offer great control in the design of the electronic and optical properties of devices. Particularly, in recent years there has been significant interest in zero dimensional (0D) semiconductor structures. In addition to fundamental scientific interest, there

is a strong technological motivation due to the potential applications of 0D structures in better-performing or novel devices such as lasers, wavelength switches, optical memories, and quantum computers.

1.2 Some Applications Driving Quantum Dot Research

Devices made from confined structures can be grouped under two broad categories: quantum optical, which includes devices designed for the emission or detection of photons, and quantum electronic, which includes devices designed to control electrons. Devices such as CD players and optical storage media for computers, for instance, are designed utilising near-infrared to visible semiconductor laser sources. There is demand in telecommunications for high quality sources and detectors operating at 1.3 and 1.5 μm because these wavelengths coincide with the minima of dispersion and absorption in optical fibres. Similarly, emitters are produced that operate at 1-10, 35, 60, 94, 140, 220 Ghz because these frequencies correspond to minima in the attenuation curve due to absorption by atmospheric components [6]; cordless and cellular telephones operate in the higher range of these frequencies. Considering quantum dots specifically, the foreseen applications are wide ranging; they include photodetectors, lasers for telecommunications, and quantum information devices (spintronics). Fundamental research leading to the deepening of our understanding of the quantum dots themselves and their formation may in turn lead to advancements in the production of such devices.

1.2.1 Computing and Memory Devices

Quantum dots, because of their limited number of discrete energy levels, can "contain" only small numbers of charge carriers. This can lead to single electron devices which could potentially lead to much faster computing at lower power requirements. Also, possibilities of quantum logic states, as opposed to the conventional binary systems, could lead to totally different computer logic and computational methods. Energy levels in 0D structures could provide two-level systems, described by two states $|0\rangle$ or $|1\rangle$, where, when the system is in one of these two states, the system is in state analogous to the 0 or 1 in conventional binary computing, and when the system is in a state given by a linear combination of the basis states, the system is in a "non-classical" state that is unavailable in present day computation [7].

As early as 1995, memory devices based on self-assembled quantum dots had been proposed, and demonstrated experimentally by Imamura et al. of Fujitsu labs [8]: Light of a properly selected, specific wavelength impinging on a quantum dot array is absorbed by some quantum dots, or possibly even a single quantum dot, exciting charge carriers to some metastable state and thereby storing information into memory. Subsequently, light signals could then be used to read the bits (or bit) already written, or to write other bits in the same array. Such optical memory devices present the possibility of storing one bit per quantum dot, so that a surface density of one quantum dot per 100 nm^2 would produce a 10^{12} bit/cm^2 memory density, that is to say 125 gigabytes (1 terabit) per square centimetre.

Nakajima et al., also at Fujitsu labs in 1997, demonstrated a fabrication technique for reliably building a single electron memory device [9]. This is therefore a quantum electronic device, as opposed to the Imamura device which is quantum optical. Essentially, they produced a modified field effect transistor by replacing the gate with a quantum dot. The device is based on the Coulomb blockade effect: A single electron tunnels to the quantum dot serving as a storage node, and a downward shift in drain current is measured with increasing gate voltage. A subsequent reduction of gate voltage does not produce a similar shift; this hysteresis demonstrates the mnemonic nature of the device.

1.2.2 Telecommunication Light Sources

Laser structures based on quantum dots are very similar to those based on quantum wells, but the replacement in the active region of the quantum well by quantum dots leads to substantial performance gains [10]. These are mainly due to four effects: (1) The reduction in volume of the active region means that there is less material to populate with electron-hole pairs to reach population inversion. This leads to a reduction in threshold current density, resulting in increased laser reliability and lower power consumption. (2) The sharp spectral lineshape of single quantum dots leads to a commensurately sharp gain spectrum. This can give a very small wavelength chirp[4] under high-speed direct modulation in quantum dot lasers which is something that conventional multiple quantum well lasers cannot do. (3) It is possible to reach population inversion in energy levels higher than the excitonic ground state (i.e. electron in the conduction band ground state and hole in the valence band ground state). This is due to the fact that population inversion can be established at reduced current

[4] Chirp in lasers refers to the emission wavelength instability similar in musical terms to vibrato applied to an otherwise pure tone.

densities, as well as to the fact that quantum dot energy states rapidly reach gain saturation. This makes a spectrum of recombination energies, albeit discrete, available from each quantum dot in an ensemble while still operating at current densities lower than those for quantum well lasers. (4) The variation of quantum dot properties across the ensemble, compositional and structural leads to a distribution of the energy levels. The overall gain spectrum of the ensemble is likewise broadened. This, in addition to the third point can be exploited in the fabrication of tunable lasers.

Techniques for obtaining long wavelengths from InAs quantum dots have been explored. When these are grown on InP instead of GaAs as mentioned in Section 1.1, because of differences in strain and bond energies, the quantum dots produced are larger and in consequence emit at longer wavelengths. Quantum dot based InAs/InP lasers have recently been produced at 1.6 μm [11][5]. There are methods by which longer wavelengths can be reached with the InAs on GaAs system. Maximov and coworkers, as shown in Figure 2 have found growth conditions that lead to the formation of quantum dot clusters. With this they reached wavelength beyond 1.7 μm. Stintz and coworkers have placed the InAs quantum dots in a thin quantum well that is an alloy of the quantum dot material and the barrier material, as seen in Figure 3. With this they reached wavelengths longer than 1.3 μm. These are essentially ways of making the quantum dots bigger.

[5] Lasers emitting in this range of wavelengths can also be obtained in the InP system using InGaAsP/InP quantum well.

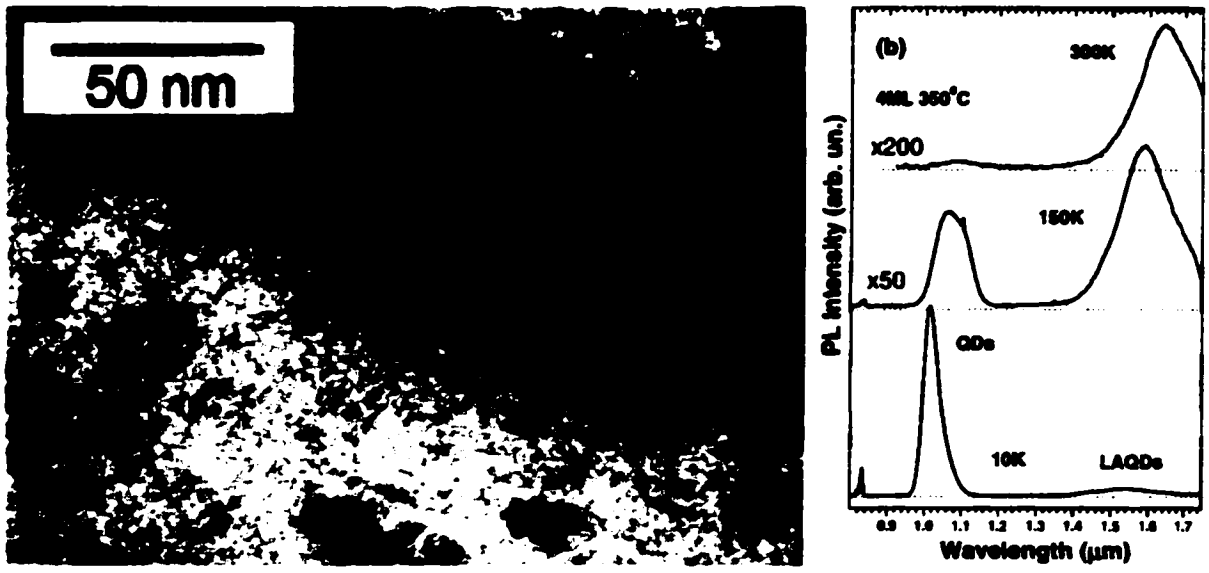

Figure 2. Plan view Transmission Electron Microscopy (TEM) image, and photoluminescence (PL) spectra of quantum dot clusters. From ref. [12].

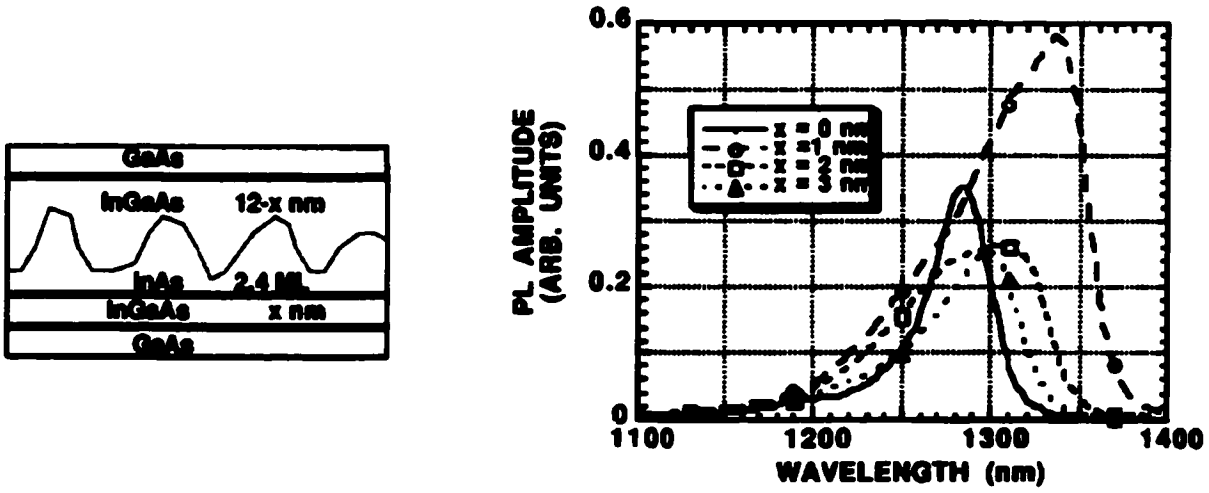

Figure 3. Schematic and PL spectra of "dots in a well" structure. From ref. [13].

Quantum dot lasers are a prime candidate for reaching one of the present day goals in laser production, the fabrication of lasers operating at 1.3 μm and 1.5 μm while still using GaAs substrates, because GaAs wafers are cheaper than the InP alternative, and volume production on GaAs is more advanced. Our work on the effects of the arsenic pressure and capping on quantum dots is of direct interest in addressing the difficulties in producing long wavelength sources from quantum dots. The members of the Epitaxy group at IMS/NRCC in Ottawa, Canada, where I performed the bulk of my doctoral research, have been studying over the past few years the fundamental aspects of quantum dot growth to see how the growth itself can be adjusted to tune the properties of quantum dots. In Chapter 4 we shall review the quantum dot growth control parameters studied by our group.

1.3 Scientific Contributions of this Thesis

The production of semiconductor devices based on self-assembled quantum dots, such as those described in the previous section, requires precise knowledge of the dependence of the quantum dot properties on the growth control parameters. This knowledge is still incomplete. The presence in the literature of conflicting reports of growth studies is evidence that the required growth control is still to be established.

My doctoral research identifies the dependence of the properties of quantum dots displaying well-resolved electronic shells on the group V pressure used during the deposition and annealing of the strained material. It also clarifies the dependence of the quantum dot properties on two already recognised growth control parameters, the substrate temperature and the coverage of strained

material. To do this required a novel experimental approach to the problem. The combination of techniques used to characterise the quantum dots, RHEED, SEM, AFM and PL produced an extensive set of experimental data. This allowed us to study the role played by the arsenic pressure, InAs coverage, and substrate temperature on the formation of the quantum dots, and of the arsenic pressure and capping procedure on the quantum dot structural parameters (height, width, density) as well as on the resulting electronic states [14,15].

The data reveal that the arsenic pressure, generally ignored as a growth control parameter prior to this work, produces a shift in the resulting electronic states greater than that due to the other growth control parameters. This thesis provides an explanation of the role of the arsenic pressure in the formation of quantum dot ensembles, and proposes a plausible conceptual model of the quantum dot modifying effects occurring during the overgrowth (capping) of quantum dots.

The study was performed on InAs/GaAs quantum dots, but the effects of the group V pressure and capping procedure may be significant in other growth systems. Therefore, the contributions to knowledge made by this thesis are germane to III-V epitaxy as a whole. They should contribute to the advancement of the epitaxial growth of similar materials specifically, and of the technique generally.

2 Growth Constituents, GaAs and InAs: Bulk and Low Dimensional Properties

This chapter provides the reader with adequate background knowledge on the growth materials as well as quantum dot (QD) structure discussed in the following chapters. The chapter starts by describing the bulk properties of the two growth materials used in the experiments presented in this thesis: GaAs and InAs. Following this, we present a simple model to describe an InAs QD imbedded in GaAs. The chapter concludes with calculations based on this model and some discussion of the results.

2.1 Crystal Structure of GaAs and InAs

The compound semiconductors GaAs and InAs have the zincblende crystal structure illustrated in Figure 4. This structure consists of two interpenetrating face-centred-cubic anion and cation sublattices displaced from each other by $\left(\frac{1}{4}\frac{1}{4}\frac{1}{4}\right)a$, where a is the lattice constant. Epitaxy of III-V semiconductors is commonly done on the polar (001) GaAs surface. The {001} planes are separated by $\frac{1}{4}a$ and are alternately occupied by cations or anions. Each pair of (001) planes comprises a monolayer (ML) of either GaAs or InAs, and there are thus 2 ML per unit cell.

InAs has a larger lattice constant than GaAs (a_{InAs} = 6.0584 Å and a_{GaAs} = 5.6532 Å at room temperature); thus thin InAs films deposited on GaAs substrates are compressively strained. The strain in the overlayer of the thin film is given by $\delta = \left(\frac{a_e - a_s}{a_e}\right)$ where a_s and a_e are the unstrained lattice constants of substrate and epitaxial layer [17]. In heteroepitaxy of InAs on GaAs, such as in

the samples studied for this thesis, the height of 1 ML of InAs, which when unstrained in homoepitaxy is 3.0292 Å, becomes 3.2393 Å because of the tetragonal distortion due to the compressive strain caused by the surrounding GaAs [18].

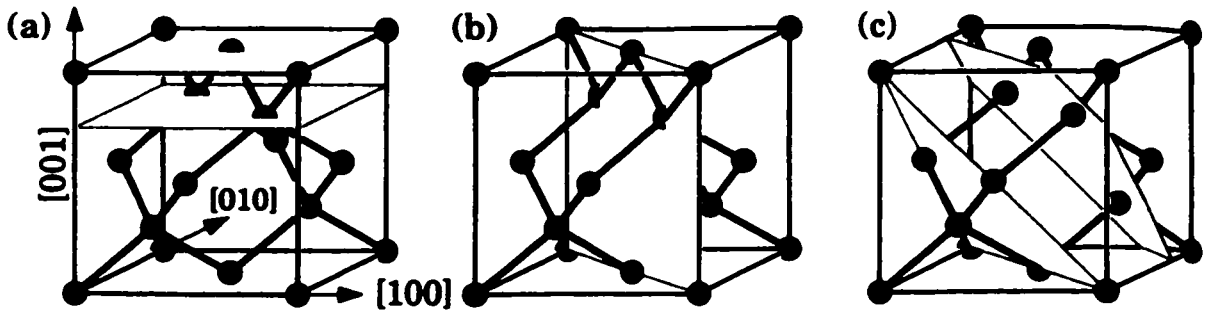

Figure 4. Important planes in the zincblende crystal structure of GaAs: (a) GaAs(001), (b) GaAs(110), and (c) GaAs(111). From ref. [16].

2.2 Band Structure of GaAs and InAs

The dependence of the bandgap of common compound semiconductors is displayed in Figure 5 as a function of lattice constant, which is determined by composition. Direct and indirect energy gaps are plotted with full and broken lines respectively. The two materials of interest in this thesis, GaAs and InAs have bangaps equal to 1.35 and 0.36 eV respectively at room temperature [20]. As illustrated in Figure 6, in InAs/GaAs heterostructures, the 1.0 eV difference in bandgaps leads to band offset of roughly 0.7 eV in the conduction band (CBO) and 0.3 eV in the valence band (VBO) [21].

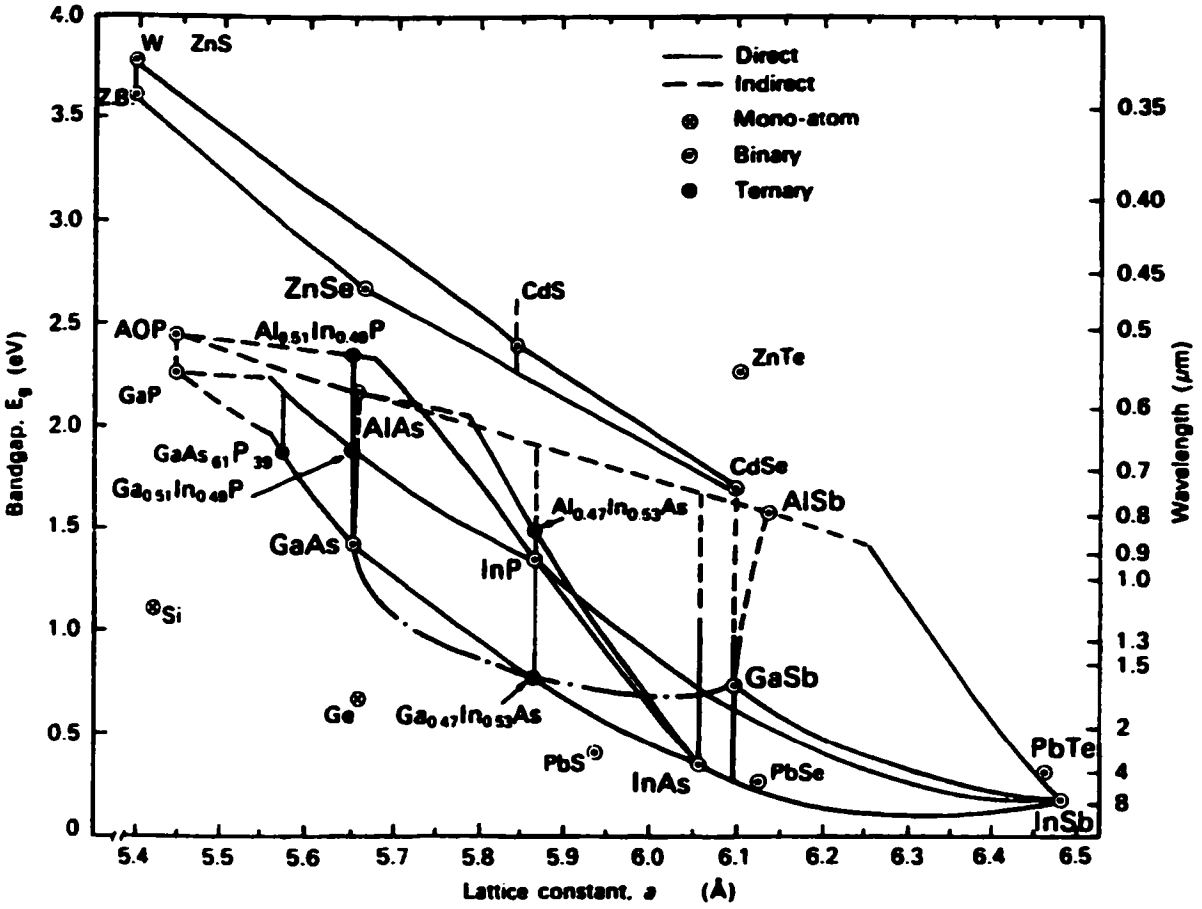

Figure 5. Bandgap and lattice constant of common semiconductors. The lines connecting the points represent alloys of varying composition. From ref. [19].

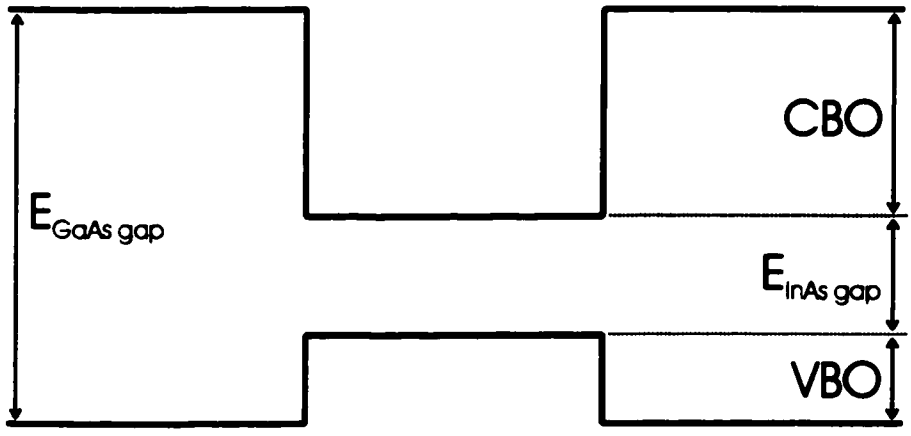

Figure 6. Schematic representation of the band offsets for InAs/GaAs heterostructures, showing the bandgaps (E_{gap}), the conduction band offset (CBO) and the valence band offset (VBO).

The temperature variation of the bandgap can be described by the Varshni equation:

$$E_g(T) = E_g(0) - \frac{\alpha T^2}{(T+\beta)} \tag{1}$$

where α and β are material-dependent constants [22]. The dependence of the bandgap energy on composition and temperature has been determined for a number of III-V semiconductors, including InAs and GaAs: for GaAs $\alpha = 5.8\times10^{-4}$ eV/K and $\beta = 300$ K and for InAs $\alpha = 4.19\times10^{-4}$ eV/K and $\beta = 271$ K [23]. The accepted zero temperature gaps for GaAs and InAs are 1.519 eV and 0.417 eV respectively [21].

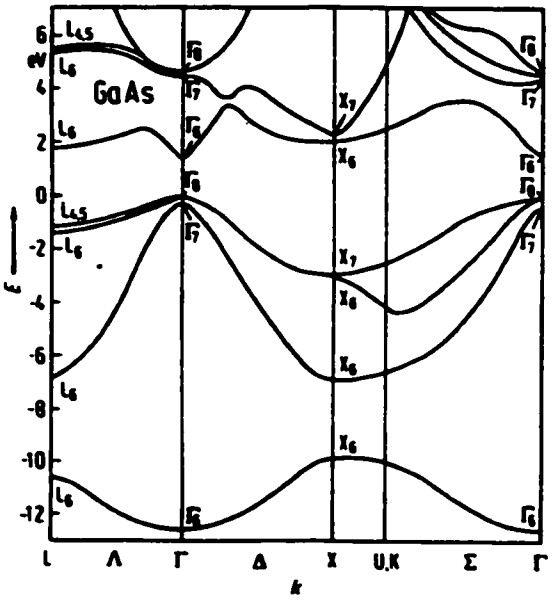

Figure 7. Band structure of GaAs obtained by a non-local pseudopotential calculation. From ref. [24].

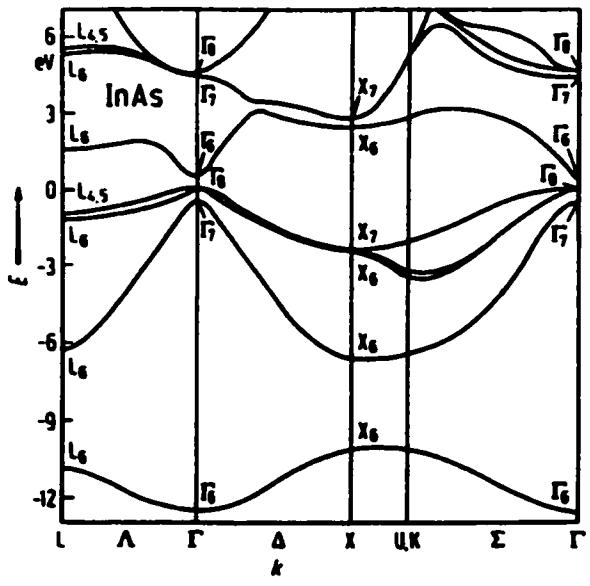

Figure 8. Band structure of InAs obtained by a non-local pseudopotential calculation. From ref. [24].

GaAs and InAs are direct-gap semiconductors. Calculated band structures of these III-V semiconductors are illustrated in Figures 7 and 8. The maxima of the uppermost (heavy and light hole) valence bands of all III-V semiconductors are situated at the Γ point; however there are three conduction band minima (at the Γ, L, and X points). The relative arrangement of these minima determines the nature of the bandgap. The bottom of the conduction band is located at the Γ point for GaAs and InAs, hence these semiconductors have a direct band gap, and as a result make an excellent choice for optical devices relying on direct optical transitions.[6] In these bulk materials, the heavy and light hole valence bands are degenerate at the Γ point; however in heteroepitaxy this degeneracy is lifted due to strain and carrier confinement in low dimensional structures.

For direct-gap semiconductors, near the conduction band edge at the Γ point, assuming isotropic parabolic bands, the energy-momentum relation is given by

$$E(k) = E_c + \frac{\hbar^2 k^2}{2m^*} \tag{2}$$

where E_c is the conduction band edge, and m^* is the effective mass of the electrons. In general, the effective mass of charge carriers in semiconductors is given by the second derivative of the energy E, with crystal momentum $\vec{p} = \hbar\vec{k}$.

$$\frac{1}{m^*} = \frac{d^2}{dp^2}E = \frac{1}{\hbar^2}\frac{d^2}{dk^2}E \tag{3}$$

The effective mass for high curvature (narrow parabola) at the band edge is therefore smaller than that for low curvature (wide parabola). For $In_xGa_{1-x}As$, the effective mass of the electron is $m_e^* =$

[6] Optical transitions across an indirect bandgap must be assisted by phonons to satisfy momentum conservation.

0.067 + 0.04x [23]. The effective masses for the holes along the {100} axis, the most common growth axis, are:

$$m_{hh}^{*}(x) = \frac{m_0}{\left(\gamma_1(x) - 2\gamma_2(x)\right)}$$
$$m_{lh}^{*}(x) = \frac{m_0}{\left(\gamma_1(x) + 2\gamma_2(x)\right)} \qquad (4)$$

where m_0 is the free electron mass, and γ_1 and γ_2 are the Luttinger-Kohn parameters, which as a function of $In_xGa_{1-x}As$ composition are: $\gamma_1(x) = 6.85\,(1-x) + 19.67x$, $\gamma_2(x) = 2.1\,(1-x) + 8.37x$ [23].

2.3 Modelling of an InAs Quantum Dot Imbedded in GaAs

In this section, we present a simple model that we have produced following the work of Hawrylak and coworkers [25] to determine the eigenenergies of an electron-hole pair trapped in an ideal dome-shaped QD. In Section 2.3.1, we first describe the model and general aspects of the solution of the Schrödinger equation. In Section 2.3.2, we present details of the derivation of the eigenenergies of the system.

2.3.1 Description of the Model

We begin by writing a general form for the Hamiltonian of the system:

$$H = \frac{P_e^2}{2m_e^{*}} + \frac{P_h^2}{2m_h^{*}} + V_e(\vec{r}_e) + V_h(\vec{r}_h) - \frac{e^2}{\varepsilon|\vec{r}_e + \vec{r}_h|} \qquad (5)$$

where ε is the zero-frequency dielectric constant of the semiconductor, $V(\vec{r}_{e/h})$ is the potential due to the shape of the island, and the subscript e and h identify the electron or hole. For strong confinement, this structural potential (~ few hundred meV) dominates the Coulomb interaction (~ few meV) so that we can neglect the electron-hole interaction energy. The problem reduces to a one-particle Schrödinger equation:

$$-\frac{\hbar^2}{2m^*_{e/h}}\nabla^2\Psi_{e/h} + V_{e/h}(\vec{r}_{e/h}) = E_{e/h}\Psi_{e/h} \qquad (6)$$

for both electrons and holes, where $m^*_{e/h}$ is the appropriate effective mass.

Wojs, Hawrylak, Fafard and Jacak treated this problem [25] by performing a full numerical diagonalisation. They were able to show that the adiabatic approximation is justified for this system. In this approximation, due to the low aspect ratio (height/width) of the QD, the confinement in the growth direction (vertical or z-axis) dominates, and only one bound state exists for the motion in this direction. Therefore, the wavefunction can be written as

$$\Psi(r,\theta,z) = g_r(z)f(r,\theta) \qquad (7)$$

where the subscript r indicates that $g_r(z)$ varies only slowly with r (r and θ are coordinates in the plane perpendicular to the growth direction). This leads in the solution of the problem to a separation of variables for the Schrödinger equation.

Using this, in the following section, we show in detail how the motion along the z-axis can be solved as a particle in a well problem, and the motion of the electron or hole in the x-y plane can

be solved as a 2D harmonic oscillator. This then presents a picture of QDs as energetically offset 2D harmonic oscillators:

$$E = E_{0,r=0} + (n+1)\hbar\omega \tag{8}$$

where $n = 1,2,3,\ldots$ Because of the presence of a harmonic term in the solution, this model predicts that the spacing between levels is constant. The photoluminescence results that we shall review in Chapter 4 and present in Chapters 7 and 8 show that this is indeed the case in InAs/GaAs self-assembled QDs.

Using the above form with appropriately selected effective masses and confinement potentials for electrons and holes, as well as a value for the strained InAs bandgap, QD emission energies can be calculated as

$$E_{emission} = E_{InAs\ QD\ bandgap} + E_n^{electron} + E_n^{hole} \tag{9}$$

The QD selection rules [26] in this simple model translate to a requirement that n be equal for the electron and hole.

2.3.2 Derivation of the Model

Following from the previous section, we now insert the wavefunction described by equation 7 into the Schrodinger equation in cylindrical coordinates to get

$$\left\{\frac{-\hbar^2}{2m^*}\left[r^{-2}\left(r\frac{\partial}{\partial r}r\frac{\partial}{\partial r}+\frac{\partial^2}{\partial\theta^2}\right)+\frac{\partial^2}{\partial z^2}\right]+V(r,z)\right\}g_r(z)f(r,\theta) = Eg_r(z)f(r,\theta) \tag{10}$$

Now, as stated above the z-motion can be separated out, so that we can write:

$$\left(\frac{-\hbar^2}{2m^*}\frac{\partial^2}{\partial z^2}+V(r,z)\right)g_r(z)=E_0(r)g_r(z) \tag{11}$$

This equation accounts for the "z-motion" in the $V(r,z)$ potential, and this leaves $E_0(r)$ to act as an effective potential in

$$\left[\frac{-\hbar^2}{2m^*}r^{-2}\left(r\frac{\partial}{\partial r}r\frac{\partial}{\partial r}+\frac{\partial^2}{\partial\theta^2}\right)+E_0(r)\right]g_r(z)f(r,\theta)=Eg_r(z)f(r,\theta) \tag{12}$$

Because $g_r(z)$ is a slowly varying function of r, we neglect

$$r^{-2}\left(r\frac{\partial}{\partial r}r\frac{\partial}{\partial r}\right)g_r(z) \tag{13}$$

and therefore

$$\left[\frac{-\hbar^2}{2m^*}r^{-2}\left(r\frac{\partial}{\partial r}r\frac{\partial}{\partial r}+\frac{\partial^2}{\partial\theta^2}\right)+E_0(r)\right]f(r,\theta)=Ef(r,\theta) \tag{14}$$

Equation 14 together with equation 11 determine the system in this approximation [25] .

The energy for the particle motion in the z-direction, $E_0(r)$ is found using equation 11, in which r is not a variable but a parameter. This means that $E_0(r)$ is found at every point r away from the centre of the QD for the thickness of the QD at that point, that is, $t(r)$. This problem was treated in a similar manner by Raymond [27], but for the case of infinite confinement barriers. The potential

$V(r,z)$ takes the value 0 inside the QD, that is for $0<z<t(r)$, and V_0 outside. This is the familiar particle in a finite well problem, which we solve using the series solution of Aronstein and Stroud for the energy levels of a finite square well [28]. Taking only the leading-order correction factor to the energy of an infinite square well, they get

$$E_{\text{finite}} = \frac{P^2}{(1+P)^2} E_{\text{infinite}} \tag{15}$$

where

$$P = \frac{\sqrt{2mV_0}}{\hbar} \frac{l_0}{2} \tag{16}$$

is the *well-strength parameter* for a particle of mass m in a well of thickness l_0 and barrier height V_0. This gives

$$E_0(r) = \frac{P^2}{(1+P)^2} \frac{\pi^2\hbar^2}{2m^* t^2(r)} \tag{17}$$

in which the appropriate values of V_0 and m^* for electrons and holes must be used when calculating P in the finite well correction factor.

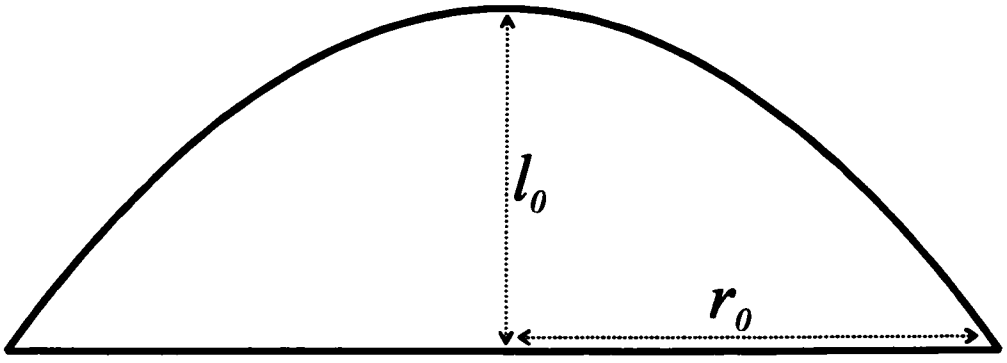

Figure 9. Paraboloid shape used to model the shape of a quantum dot. Relating this figure to equation 18, the positive z-axis points downward.

As pictured in Figure 9, we choose to model the QD by the volume enclosed by a paraboloid centred about the origin truncated by a plane at $z = l_0$:

$$z = \frac{l_0}{r_0^2} r^2 \tag{18}$$

where l_0 is the height and $2 \times r_0$ is the width of the QD. The thickness $t(r)$ at each radial position is given by:

$$t(r) = l_0 - \frac{l_0}{r_0^2} r^2 \tag{19}$$

Rearranging and inserting into $E_0(r)$, we get:

$$E_0(r) = \frac{P^2}{(1+P)^2} \frac{\pi^2 \hbar^2}{2m^* l_0^2} \left(1 - \left(\frac{r}{r_0}\right)^2\right)^{-2} \tag{20}$$

We now perform a binomial expansion of the term in the brackets and keep only the first two terms:

$$\left(1 - \left(\frac{r}{r_0}\right)^2\right)^{-2} = 1 + 2\left(\frac{r}{r_0}\right)^2 + \quad \ldots \tag{21}$$

The assumption that r/r_0 is small means that we are only considering the states for the lowest levels of excitation of lateral motion. Inserting this into $E_0(r)$, we get

$$E_0(r) = \frac{P^2}{(1+P)^2} \frac{\pi^2 \hbar^2}{2m^* l_0^2} \cdot \left[1 + 2\left(\frac{r}{r_0}\right)^2\right] \tag{22}$$

This form can be described in the following way. When moving in the x-y plane, the particle feels an harmonic effective potential equal to the ground state energy of a quantum well of thickness l_0 scaled by a parabolic factor equal to $2(r/r_0)^2$ due to the curvature of the QD.

Substituting this form for $E_0(r)$ into equation 14, we get

$$\left\{\frac{-\hbar^2}{2m^*}r^{-2}\left(r\frac{\partial}{\partial r}r\frac{\partial}{\partial r}+\frac{\partial^2}{\partial\theta^2}\right)+\frac{P^2}{(1+P)^2}\frac{\pi\hbar^2}{2m^*l_0^2}\left[1+2\left(\frac{r}{r_0}\right)^2\right]\right\}f(r,\theta)=Ef(r,\theta) \qquad (23)$$

The 1 in the square bracket represents a constant that offsets all energy levels, so that this equation describes an energetically offset 2D harmonic oscillator with eigenenergies

$$E = E_{0,r=0} + (n+1)\hbar\omega \qquad (24)$$

where $E_{0,r=0}$ is given by equation 22 using r=0, n = 1,2, 3, . . . , and

$$\omega = \frac{P}{(1+P)}\frac{\sqrt{2}\pi\hbar}{m^*l_0r_0} \qquad (25)$$

In the case of $r_0 \to \infty$, we recover the result for a single quantum well of thickness l_0. Because the second term in equation 24 is the solution to a two-dimensional simple harmonic oscillator, this model predicts that the spacing between levels is constant.

2.4 Expected Properties of InAs/GaAs Quantum Dots

To discuss the model presented in the previous section, there remains the selection of values for $V_{e,h}$ and $m^{*}_{e/h}$. The literature is replete with values for these parameters for InAs [21]. Unfortunately, very few of these values agree. Basing ourselves on the review of III-V band parameters by Vurgaftman, Meyer and Ram-Mohan [21], we use the "recommended low temperature value" for the effective mass of electrons in bulk InAs, $0.026m_e$. We use their "composite set" of Luttinger parameters, $\gamma_1 = 20$ and $\gamma_2 = 8.5$ to calculate the effective mass of holes, $0.33m_e$. For the value of the potential barrier for the electrons, we use the only reported value for a measurement of the conduction band offset in InAs/GaAs QDs, 0.34 eV. For the value of the potential barrier for the holes, we use the ratio of the valence band and conduction band deformation potential, $a_v/a_c = 1.00$ eV / 5.08 eV and calculate the valence band offset as:

$$V^{QD}_{holes} = V^{bulk\ InAs}_{holes} - \frac{a_v}{a_c}\left(V^{bulk\ InAs}_{electrons} - V^{QD}_{electrons}\right) \qquad (26)$$

Using a consistent set of bulk InAs conduction and valence band offsets, 0.7 eV and 0.3 eV respectively, we get for the valence band offset in InAs QDs, 0.23 eV. Finally, we add the shifts in valence band and conduction band to the accepted value for the bulk InAs band gap, 0.42 eV, and get a value of 0.85 eV for the bandgap of InAs/GaAs QDs.

For an InAs/GaAs QD 17 nm wide and 3.8 nm high, that is having an aspect ratio $l_0/r_0 \approx 0.4$, this model predicts a emission energy for the lowest electron-hole pair of 1.34 eV and an energy spacing of 0.22 eV. For an increase in size of 10%, maintaining the same aspect ratio, we get an emission energy of 1.28 eV and an energy spacing of 0.19 eV. The results we shall present in

Chapter 8, will show that our model overestimates the emission energies by approximately 10% and the level spacings by a factor of two. The shifts as a function of size are proportionally overestimated, but the sign is correct: Smaller QDs emit at higher energies. The difficulty in selecting adequate parameters limits the quality of the results obtained with this model.

In the case of a well of infinite height, the wavefunction has an extent exactly equal to the well width, but for a well of finite height, the wavefunction extends beyond the barrier, decaying exponentially. This means that the wavefunction "samples" the surrounding GaAs where the effective mass is no longer equal to that of the QD. This contributes to the difficulty of selecting appropriate effective masses for the electron and hole.

If we rely on the wide range of values reported in the survey of experimental and theoretical band parameters for InAs done by Vurgaftman, Meyer and Ram-Mohan [21], we must conclude that there is large uncertainty in the set of valance band offset, bandgap, and conduction band offset that we used in our calculations, (0.34, 0.85, 0.23) eV. If we do not account for strain in the band parameters, that is if we use (0.70, 0.42, 0.30) eV, we get the following: for a QD 20 nm wide having an aspect ratio of 0.2, the emission energy for the lowest electron-hole pair is 0.87 eV and the energy spacing is 0.10 eV; and for an increase in size of 10%, maintaining the same aspect ratio, we get an emission energy of 0.82 eV and an energy spacing of 0.09 eV. Considering that strain effects should move the conduction band well upwards and the valence band well downwards without changing the curvature of the potentials, one would expect the strain to cause an overall shift of energy levels without much effect on the energy spacings. Our model is consistent with this and the sign of the shift due to the strain in the InAs QD.

Our determination of the band offsets and bandgap neglected the biaxial component in the deformation potentials. Including these contributions should reduce the calculated strained InAs-quantum-dot bandgap value by a amount on the order of ~ 0.1 eV, thereby reducing the emission energies by approximately the same amount. We therefore expect that including this in our calculations should improve the agreement of our model with experimental results.

Further considerations must be made before comparing the predictions of such a model with real samples. Systems produced by self-assembly take the form of arrays of a large number of QDs, and because of this, the emission spectrum of self-assembled QD samples will be broadened due to size and composition inhomogeneities (order of a few tens of meV [29]) over the entire ensemble. Each QD in the array contributes one sharp line for each populated excitonic level to the overall spectrum.

3 Growth Theory

This chapter presents the fundamental aspects of growth theory involved in the fabrication of self-assembled QDs. We begin by a thermodynamic justification of three growth modes: Frank-van-de-Merwe layer by layer growth, Volmer-Weber island formation, and Stranski-Krastanow island formation. The QDs formed in the strained InAs/GaAs growth system, such as those studied in this thesis are formed by Stranski-Krastanow growth. We then discuss island formation in general as a strain relaxation mechanism. This is followed by the brief description of models of the evolution of QD ensembles.

3.1 Three Growth Modes

We will describe the heteroepitaxial growth modes in terms of the chemical potential of material α deposited on material β. To do this, we start by considering the binding energy of a particle added to a crystal surface as it depends on the nature of the binding site. If we consider a system having simple cubic symmetry, we can define five different types of binding sites, as illustrated in Figure 10.

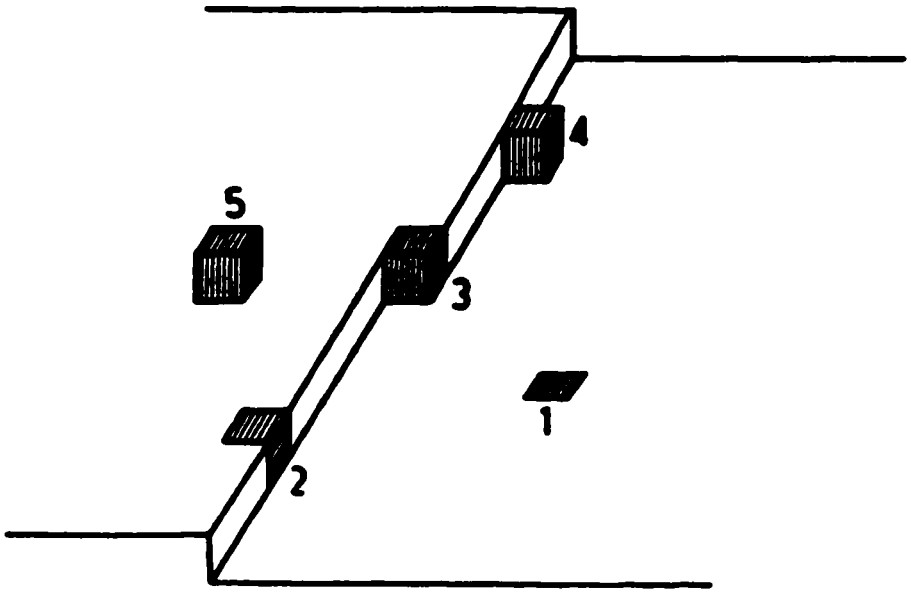

Figure 10. Five types of bonding sites in simple cubic symmetry: (1) incorporated in the surface layer, (2) incorporated in a step, (3) incorporated in a kink, (4) attached on a step, and (5) attached on top of the surface layer. From ref. [2].

The number of saturated and unsaturated (or dangling) bonds are the following for each of the five cases:

type of position	number of saturated bonds	number of unsaturated bonds
incorporated in the surface layer	5	1
incorporated in a step	4	2
incorporated in a kink (i.e. two steps)	3	3
attached on a step	2	4
attached on top of the surface layer	1	5

Only in the case of the kink position is it possible to remove or add a particle without changing the total number of dangling bonds in the system. In general, for any symmetry, the number of bonds that must be broken to remove a particle from the kink position is equal to half the number of bonds of the same particle in the bulk. This kink position is called the "half crystal position," and the equilibrium of a crystal system with its ambient phase is determined by the binding energy in this position, which we label $\varphi_{1/2}$ [2]. This can be understood by considering that at equilibrium of the two phases, the probabilities of attachment and detachment at the half crystal position are equal.

Following this, we now write[7] the chemical potential for a layer n monolayers thick of deposited material in heteroepitaxy:

$$\mu(n) = \mu_\infty + \left[\varphi_\alpha^\alpha - \varphi^\alpha(n)\right] + \left[\xi_d(n) + \xi_e(n)\right] \tag{27}$$

Here, μ_∞ is the chemical potential of the infinite bulk, φ_α^α is the binding energy of material α on itself, $\varphi^\alpha(n=1) = \varphi_\beta^\alpha$ is the binding energy of material α on material β, ξ_d is the misfit-dislocation energy averaged over all atoms in the epilayer, and ξ_e is the elastic (pseudomorphous) strain energy per atom. If the lattice misfit is denoted by f, then the two strain energies are $\xi_e = \xi_e(f_e)$ and $\xi_d = \xi_d(f - f_e)$, where f_e is the fraction of the lattice misfit that is accommodated by elastic deformations. In this thesis, we are interested in epitaxial systems in which strain energy is relaxed elastically by the formation of QDs, not inelastically through the formation of dislocations so that $\xi_d = 0$.

---

[7] We are following the derivation found in the text *Crystal Growth for Beginners, Fundamentals of Nucleation, Crystal Growth and Epitaxy*, by Ivan V. Markov.

If $\varphi_\beta^\alpha > \varphi_\alpha^\alpha$, that is, if the epilayer wets the substrate, and if the misfit is negligible, then $\mu(n)$ will be an increasing function of n and the growth will proceed layer by layer. This growth mode is called Frank-van der Merwe. If $\varphi_\beta^\alpha < \varphi_\alpha^\alpha$, that is, if the epilayer does not wet the substrate, then $\mu(n)$ decreases with n from the start (n=1), and the growth will proceed via 3D island formation. This growth mode is called Volmer-Weber. Finally, if again $\varphi_\beta^\alpha > \varphi_\alpha^\alpha$, but the misfit is not negligible, then $\mu(n)$ will start out as an increasing function of n, and at some value of n will become an decreasing function. The growth will start out layer by layer, but beyond the value of n where the slope of $\mu(n)$ changes, there will be formation of islands. This growth mode is called Stranski-Krastanov. Schematic curves of $\mu(n)$ can be found in Figure 11.

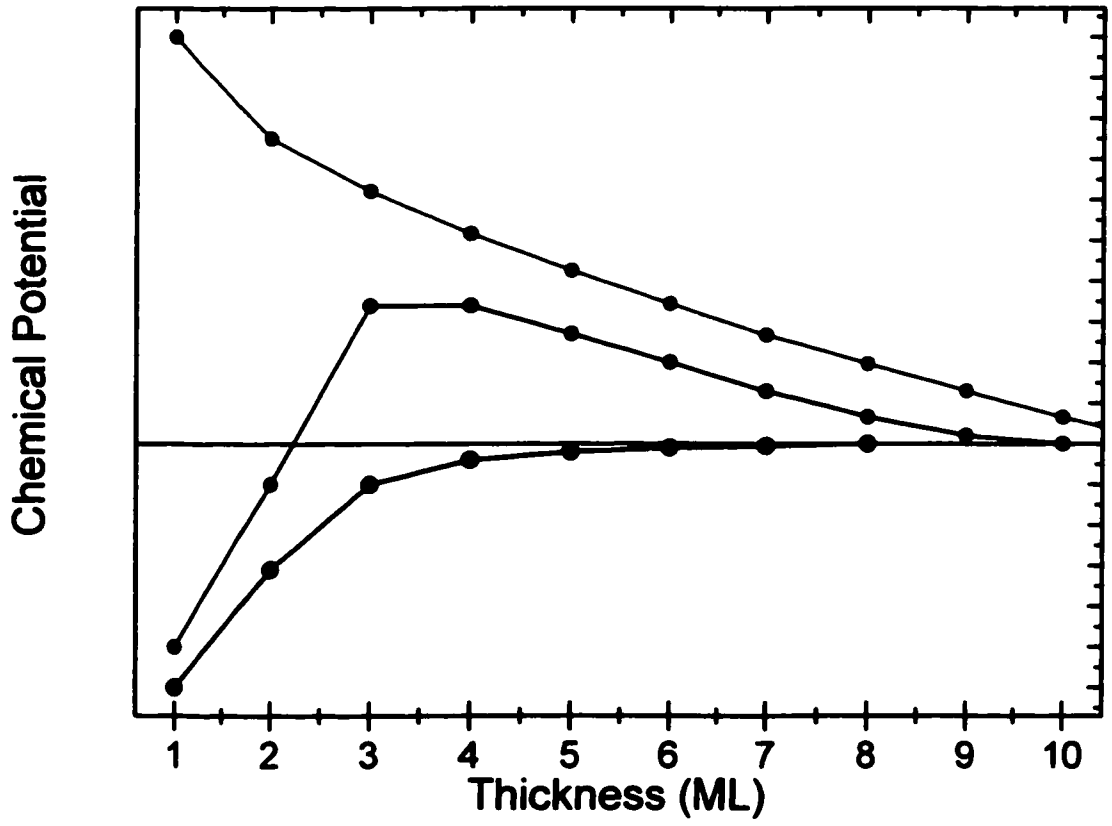

Figure 11. Schematic representation of the chemical potential for the three growth modes: VolmerWeber islanding (red), Stranski-Krastanov layer-by-layer followed by islanding (green), and Frank-van der Merwe layer-by-layer (blue).

The QDs studied in this thesis were formed in the Stranski-Krastanov growth mode. Because it will be important in the final discussion of our results, we point out that the layer by layer phase of this growth mode leads to the formation of a layer that will be referred to as the "wetting layer" (WL). Stated specifically for the system studied in this thesis, a wetting layer forms before the QDs because the chemical bond strength between InAs and GaAs is stronger than that between InAs and other InAs. In other words, InAs adhesion to GaAs is stronger than cohesion of InAs to itself.

3.2 Island Formation as a Relaxation Mechanism

As discussed in Section 3.1, the formation of a coherent (without dislocation) island is associated with an overall relaxation of the strain energy per particle $\Delta\xi_e < 0$. This drive will be opposed by the increase in surface energy associated with the increase in total surface area, $\Delta A > 0$ due to the island formation.

Bond counting suggests that the relaxation energy depends on the island shape; the number of bonds in the volume of the island will increase roughly as the cube of the size (i.e. width) of the island, whereas the number of highly strained bonds in the few monolayers closest to the substrate will increase roughly as the square of the width of the island. With this in mind, one can deduce that: (1) An island having a lower aspect ratio strains a larger fraction of its bonds than one having a higher aspect ratio. (2) For a given shape, the relaxation energy will depend on volume.

The above discussion is of thermodynamic equilibrium of the near surface region containing the deposited strained material. These considerations of equilibrium did not include the strain energy in the wetting layer or substrate under each QD, nor the strain in the material surrounding the QD when they are capped. Such considerations of the dependence of strain on QD size shall be important in the final interpretation of our results in Chapter 9. Whether the system ever reaches thermodynamic equilibrium or is pinned in some state along its evolution towards equilibrium will be the focus of the following section in which we present a few relevant examples of models of QD ensemble evolution.

3.3 Models of Quantum Dot Ensemble Stabilisation

The relaxation discussed in the previous section triggers the 2D to 3D transition and therefore the QD formation. Thermodynamic considerations suggest that once islands are formed they will evolve according to the process of "Ostwald Ripening," in which larger islands expand at the expense of smaller islands in a minimisation of the total surface energy, or the process of coalescence, the growth of islands into each other [30]. Coalescence can be relevant in the later stages of evolution of higher density QD ensembles, and can produce islands or clusters considerably larger than the average island size (such as those seen in Figure 2). Ostwald ripening leads to a wide size distribution that evolves in a self-similar manner, increasing the average island size and decreasing the island density. Therefore, thermodynamic considerations of the Stranski-Krastanov growth mode do not predict, on their own, the observed narrow size distribution of self-assembled QD ensembles [31-33].

Something must enter into play to explain the experimentally observed sharp size distributions in QD ensembles. Despite extensive study of self-assembled QD growth, including both luminescence and structural characterization, the growth mechanisms of QD structures are not fully understood. Models of QD formation calling upon either kinetic limitations or strain influences in thermodynamic equilibrium have been proposed to explain similar observations of QD ensemble properties.

There is a debate in the literature as to whether the sharp size distribution of self-assembled QD ensembles is due to kinetic limitations or to the attainment of thermodynamic equilibrium. If a system were to evolve to equilibrium, the final state of the ensemble should be independent of history and dependent only on the thermodynamic parameters at the time where the state of the system is observed. The effects of the thermodynamic control parameters on a system at equilibrium should be reversible. The system cannot be considered to ever reach thermodynamic equilibrium while the amount of deposited material is being changed, that is during deposition or a high temperature anneal during which desorption occurs. In Chapter 6, we shall describe how we arrived at the values for these control parameters that were used in our experiments. The pressure of interest will be the arsenic pressure, and it is its effects on the formation of QDs that is the main focus of this thesis.

In the following section we will briefly discuss the thermodynamic approach to the modelling of the evolution of QD ensembles. Our results do not support "thermodynamic limitations of QD evolution," rather they lend support to kinetics playing a dominant role. Indeed, some theories suggest that the kinetic processes can slow down to such an extent that the evolution of the system becomes trapped in a given state and Ostwald Ripening does not occur. This is sometimes called

kinetically self-limited growth. The subsequent section will describe in greater detail than the thermodynamic modelling a selection of such "kinetic models."

3.3.1 Models of Thermodynamically Limited Quantum Dot Evolution

The theoretical work of Shchukin tries to explain the results of Ledentsov et al. by considering the strain dependence of the surface energy [34]. This theory suggests that the thermodynamic equilibrium of a lattice-mismatched heteroepitaxial system of 3D coherent islands is a periodically ordered array of identical pyramid shaped islands, and that no Ostwald ripening should occur. In this model, there is no energetic benefit to Ostwald ripening because the strain-induced renormalisation of surface energies leads to a decrease in the total surface energy despite the increase in total surface area due to the presence of islands. This work is concerned with amounts of deposited material as large as twice (or more) the amount at which the 2D to 3D growth transition occurs. Differently, some of the kinetic theories presented in the following section are concerned with coverages only slightly above this critical value.

The work of Schukin suggests that the build up of strain energy in the underlying surface due to the presence of the QDs limits the size of the QDs, and furthermore that this strain energy can lead to ordering in the QD ensemble. Ledentsov and coworkers observe a weak ordering interaction of nearest neighbours [35] at coverages exceeding the 2D to 3D transition by more than one monolayer. Other groups have used this interaction to organise the QDs in a lattice [36]. QD ensembles produced at near critical coverages, such as ours, do not display such in plane ensemble organisation

[31,37,38]; this is due to the low QD density. The QD ensembles we shall present in Chapters 7 and 8 are of this type. We will not relate our results to such a strain limited model.

3.3.2 Models of Kinetically Limited Quantum Dot Evolution

This is not intended as an exhaustive review of kinetic models of QD formation. The models presented in this section are examples of how kinetics can lead to sharp size distributions in QD ensembles. They also introduce the sort of processes that can be expected to be relevant to the discussion of our results in Chapter 9.

3.3.2.1 Dobbs et al.

Dobbs and coworkers [32] present a kinetic model for calculating the time dependence of QD formation. In a mean field approach, they allow the processes of deposition, diffusion, attachment and detachment to change densities of group III adatoms, and of 2D and 3D islands. Their calculation assumes that the wetting layer has already been formed. They derive analytically a system of three rate equations for the density of group III adatoms, and that of 2D and 3D islands, and 2 differential equations for the average size of 2D and 3D islands. This system of equations depends on six parameters that are material and strain-dependent: E_s, i^*, E_{i^*}, E_a, E_{ll}, and E_e.

The flux of atoms impinging upon the surface of the substrate determines the growth rate. Adatoms then diffuse on the surface by a process of hopping between surface sites with an energy barrier, E_s. Adatoms then collide and nucleate to form 2D islands. Islands smaller than a critical size

i^* and associated binding energy, E_i, dissolve, and islands larger than this critical size grow. For adatoms attaching to islands, the diffusion barrier E_s can be augmented by an additional barrier, E_a. This additional barrier can be due to strain, among other possible causes such as adsorbed reaction products in MOCVD. This E_a barrier reduces the net flux of adatoms going to every island. Importantly this strain-induced barrier E_a increases with increasing island size. Furthermore, as islands grow atom detachment from their periphery increases due to strain; they give this dependence to the detachment barrier: $E_d = E_d(\infty) + E_0\left(\ln r/r\right)$, in which $E_d(\infty)$ is set to zero for this model, E_0 is a strain-dependent energy parameter, and r is the island radius scaled to the lattice parameter.

As the size of 2D islands increases, the population of adatoms diffusing on their upper surface increases and the probability of a second layer nucleating increases. This is dependent on the rate of detachment from the island periphery, and on the barrier, E_e, for atoms to cross step edges. They identify the point of transition form 2D to 3D growth as the onset of nucleation of a second layer atop the 2D islands.

The general aspects of the 2D to 3D transition predicted by this model agree well with our growth observations, but some details differ. An important behaviour predicted by this model is that as soon as 3D islands are formed, they become traps for atoms that are newly deposited and those that detach from 2D islands [32,39]. Because 3D islands consume the arriving flux of atoms and the flux of atoms detaching from 2D islands, the average 2D island size decreases suddenly and 3D nucleation stops[8]. This results in the behaviour that 3D island density increases rapidly and saturates

[8] 2D nuclei are required for 3D nucleation to occur. This is because 2D islands must attain a certain width for the population of atoms diffusing on top of them to be high enough to allow 2D nucleation to occur on top of the first 2D nuclei, thereby forming a 3D nucleus.

as deposition proceeds. After this, further deposition is predicted to only increase the island size, but not the island density. Results of InAs on GaAs obtained at IMS/NRCC that we will review in Section 4.2 will contradict this predicted behaviour, and results that we will present in Chapter 7 will show that whether atoms deposited after the 2D to 3D transition go into the QDs or the wetting layer is dependent on the arsenic pressure during the deposition of In.

Some groups report a reduction in the amount of material remaining in the wetting layer after the transition from layer by layer to island growth due to transfer of atoms from the wetting layer to the QD ensemble [31,40,41]. This is sometimes described as a dynamic wetting layer. The results we present in this thesis, and indeed the results obtained by our group over the past few years include this behavior. (We will review these results in Chapter 4) Dobbs and coworkers include in some of their calculations a dynamic wetting layer [42]. The trends in the evolution of the 3D island density were not significantly different from those they obtained without including the dynamic wetting layer, and the only considerable difference was in the island volume predicted.

The size-dependent strain contribution, E_a, to the energy barrier for adatom attachment at the periphery of QDs will be included in the discussion of our results in Chapter 9. It serves as a barrier to adatom attachment and therefore reduces the flux of adatoms going to islands, leading to an effect similar to a detachment process. An increase in the overall detachment rate leads the system to a narrowing of the island size distribution [43] by increasing the density of adatoms required for the nucleation of new islands instead of the growth of already existing islands. In a more sophisticated version of the same theory [42] Dobbs and coworkers included a strain-induced contribution to E_a.

This contribution was an increasing function of island size. From this, they predict that the islands in a strained system will evolve towards a self-limiting size and a very narrow size distribution.

3.3.2.2 Barabási et al.

Barabasi and coworkers [33] present a two dimensional (i.e.1D plus height) solid-on-solid model for determining the effects of strain on island formation in heteroepitaxial systems. They include the processes of deposition and activated diffusion in a Monte Carlo simulation of coherently strained growth, that is, growth without the formation of dislocations. Unlike the model of Dobbs and coworkers, their calculations do not assume that a wetting layer has already formed, but rather determine the point during deposition at which islanding will occur in addition to the evolution of the islands after they have formed. They identify all clusters higher than 1 ML as being islands, and define their width as being their lateral size in the second monolayer. This model predicts the self-assembling of islands for large enough misfits.

They allow atoms at the free surface to hop to neighbouring lattice sites, imposing a condition preventing jumps of more than one lattice site at a time. They account for strain by allowing harmonic interaction between nearest- and next-nearest neighbours and disallowing dislocations. The probability for an adatom to jump to a neighbouring site is proportional to $\exp\left[-\left(nE_n + E_0 - E_s\right)/k_BT\right]$, where n is the number of neighbouring atoms, E_n is the bond energy, E_0 is the energy barrier for diffusion of an isolated atom placed on a strain-free substrate, and E_s is the strain energy given by $E_s = \left(c/2\right)\sum\left(a_i - a_i^0\right)^2/\left(a_i^0\right)^2$, where a_i^0 and a_i are the bulk and stretched bond lengths, i running over the occupied nearest and next-nearest neighbours.

Relaxation is allowed to occur, and elastic strain energies are recalculated after every deposition and diffusion event, moving radially outward from the last active atom, and iterating until the relative displacements of atoms are smaller than a preset value.

In the case of a misfit $\varepsilon = 5\%$, there is the formation of a wetting layer, but in the case of $\varepsilon = 7.5\%$, no wetting layer is formed. In other words, for their model system, at a misfit of 7.5% the strain energy is sufficient to take the system into the Volmer-Weber growth mode, and that misfits smaller than 5% lead to the Stranski-Krastanov growth mode.

They calculate the island density as a function of coverage for different values of misfit. This function has a peak at 1.33 ML for $\varepsilon = 0\%$, and at 1.5 ML for $\varepsilon = 2.5\%$. The drop after the peak is due to islands coalescing, and in these low-strain systems further deposition only serves to increase the average island size. In the case of both $\varepsilon = 5\%$ and $\varepsilon = 7.5\%$, the island density is not a peaked function of coverage, which is consistent with continuous nucleation and the absence of significant coalescence. In fact, in these high-strain systems, the density increases faster with coverage for higher misfit value.

They also determine the width of the island size distributions, $w_s = \sqrt{\overline{s^2} - \overline{s}^2}$, where $\overline{s}$ is the average island size. Their calculations for misfits of 0% and 2.5% predict wide size distributions, and for 5% and 7.5% misfit they predict narrow island size distributions. For $\varepsilon = 0\%$ and 2.5%, $w_s/\overline{s}$ is an increasing function of the amount of material deposited; they take this as an indication of unbound growth fluctuations. For $\varepsilon = 5\%$ and 7.5%, they find that $w_s/\overline{s}$ increases at first but then saturates; they take this to be an indication of self organisation.

The model reproduces the strain field under QDs extending into the wetting layer and the substrate that has been observed by TEM [5,44]. Figure 12 shows the strain they calculated as a function of position around the island for ε = 7.5%, and Figure 13 is a similar result obtained by another group. The strain energy can be clearly seen to increase with decreasing distance from the island. The local chemical potential, $\mu \approx -\left(nE_n + E_0 - E_s\right)$ is therefore reduced in the vicinity of the island, leading to a gradient pointing away from the island, $j \propto -\frac{d}{dx}\mu(x)$. Since, nE_n+E_0 is independent of position for an isolated adatom on a flat surface, E_s is the only position-dependent energy in the chemical potential, $j \propto -\frac{d}{dx}E_s$. This reduces the net flux of adatoms moving towards the island [45,46]. Furthermore, for a sufficiently large island, the strain energy would become comparable to the bond energy of an atom bound at the periphery of the island. This, similarly to the E_0 parameter in the Dobbs model leads to an increased probability of detachment at the island periphery. These combined effects tend to stabilise the island size by reducing the likelihood of large islands. Therefore, they concluded that it is the island-induced strain fields that lead to the narrowing of the island size distribution for large enough mismatch.

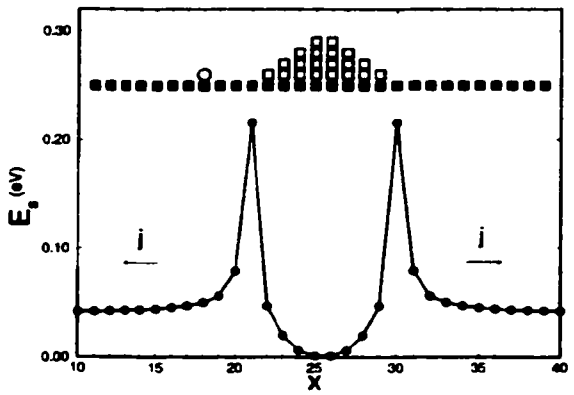

Figure 12. Calculated strain energy of an atom placed on the top of the substrate or on an island. From ref. [33].

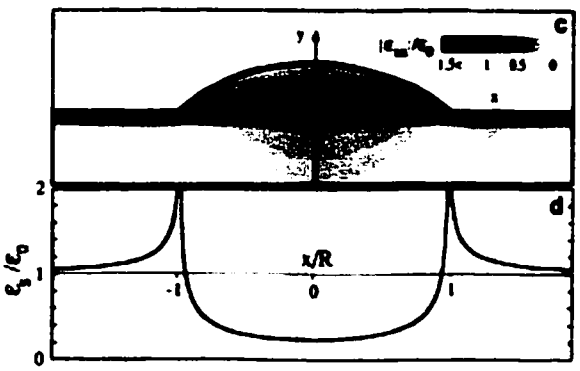

Figure 13. A contour diagram showing the calculated strain in and around an island, and the variation of surface strain along the system surface. From ref. [45].

3.4 Concluding Remarks

We presented two kinetic models in some detail: Barabási et al. predict that 2D nuclei will have a tendency to form having a narrow size distribution (although not as narrow as what is reported for self-assembled QDs), and Dobbs et al. predict that there is a tendency to sharpen the size distribution of 3D islands during the 2D to 3D transition. Both models are concerned with the highly strained area at the periphery of each island. Regarding the evolution of QDs, these models show that the strain energy acts as a size-dependent barrier to adatom attachment at the periphery of QDs. Such a size-dependent barrier favours the attachment of adatoms to smaller QDs, as well as the transfer of adatoms from larger to smaller quantum dots, thereby slowing the growth of larger islands relative to smaller islands, leading to the experimentally observed sharp size distribution of strain-induced-self-assembled QD ensembles.

After deposition is stopped, the only source of atoms for QD growth are the adatoms diffusing on the surface. In addition to the adatoms of the wetting layer, some adatoms may come from other QDs. Because of the strain-induced decrease in the barrier to atom detachment, the atoms bound at the periphery of large QDs may contribute to the population of adatoms diffusing on the surface. Also, any island smaller than the critical nucleation size will dissolve and contribute to this population. The results we will present in Chapters 7 and 8 suggest an important role for a property of these adatoms diffusing on the surface. The average separation between QDs in ensembles formed at InAs coverages just exceeding the critical coverage for 2D to 3D transition appears to be kinetically

determined by the distance over which group III adatoms diffuse before attachment. In the literature review of Chapter 4, this distance will be described as the "incorporation-diffusion length" (IDL). In Chapter 9, we shall discuss in detail the role of the IDL in the evolution of QDs.

4 Review of Quantum Dot Growth Control Parameters

In this chapter, we present the main control parameters used in the growth of self-assembled quantum dots (QDs). We concentrate on reviewing the experimental work done at IMS/NRCC on the growth of InAs QDs on GaAs. We then go on to review the literature on the effects of the group V pressure effect on the growth of self-assembled QDs. Following this, we introduce the concept of the adatom incorporation-diffusion length, and discuss its dependence on the group V pressure. In the last section of this chapter, we review the reported effects of capping self-assembled QDs. These last two sections will be particularly relevant to the analysis of our results in Chapter 9.

4.1 Four Quantum Dot Growth Control Parameters

The production of uniform QD ensembles displaying good structural and emission properties requires precise control of the epitaxial growth parameters. For example, in the case of coverage (or amount of deposited strained material) in the InAs/GaAs system grown by molecular beam epitaxy (MBE), structural studies of uncapped QDs demonstrate that the density of Stranski-Krastanov (SK) islands varies abruptly at the critical coverage for 2D to 3D transition [40,47]; minute differences in coverage exceeding this critical value lead to drastic changes in the QD ensemble properties [48,49]. Moreover, a well-resolved QD excited state structure is observed only for lower density ensembles [31,50]. As discussed in Chapter 2, a reduction in QD size leads to an increase in carrier confinement, a displacement of the QD energy levels towards higher energies, and consequently a blue shift of the QD emission lines. This is predicted theoretically [51], and observed experimentally

[38,52-54]. Precise control of all the growth parameters is also needed during the capping procedure, since it can considerably modify the QDs [38,55-57].

Optical characterisation studies of self-assembled QDs are numerous, but this is not the case for systematic studies of the growth control parameters. For instance, in the case of the arsenic pressure, which we review in Section 4.2, very few reports concerned primarily with its effects have been produced, and much of the relevant work is presented in the form of secondary topics within reports concerned with other effects. In this section, we provide a concise review of the work on self-assembled QDs that has been done by MBE at IMS/NRCC. This body of work, particularly because the studies were performed on self-assembled QD ensembles displaying well resolved excited state structures, elucidates systematically the effects of each growth control parameter. This review will be essential to the interpretation of our experimental results presented in Chapters 7 and 8. In the section discussing the amount of deposited strained material, we shall review the works of another group, Ledentsov and coworkers [35]. This will not only allow us to generalise our perspective on this important control parameter, but it will also allow us to draw a parallel with Chapter 3 because this group interpreted its results within the frame of the "thermodynamic equilibrium model" briefly discussed in the previous chapter.

Obtaining desired emission properties, such as specific emission wavelengths, entails the careful tailoring of a QD ensemble and its energy levels. To do this, and to improve the QD ensemble uniformity, the size and shape of the QDs can be engineered using the following growth control parameters [54]: (i) the amount of deposited strained material, (ii) the growth temperature, (iii) the deposition rate and anneal time which determine the time during which the QDs are allowed to evolve

to a desired size and uniformity, and (iv) post formation manipulation (some of which we discuss in Section 4.1.4). With these, it is possible to control the size and density of QDs that will be produced by a given growth, and hence the energy levels.

Except where otherwise specified, the data and the interpretation presented in Section 4.1, as well as the samples used in these studies, were produced by Fafard, Wasilewski and coworkers at IMS/NRCC. We do not state this in each of these sections, but we do indicate the specific references from which the figures have been reproduced. Although these studies were completed before the author of this thesis joined the Epitaxy group at IMS/NRCC, the author was made quite familiar with this work and has participated in the continued interpretation of these measurements.

Photoluminescence (PL) spectroscopy is the main measurement technique used to obtain the results presented in the following section. PL shall be introduced in detail in Chapter 7 of this thesis where we shall present our PL measurements. For the purposes of the present section, it is preferable to focus on the function of PL: Light stimulation of a given sample promotes electrons to higher energy levels, which leads to the creation of electron hole pairs that subsequently recombine and produce luminescence. The wavelength of the emission provides information on the energy levels within the sample studied. In the case of these samples, and those presented in Chapter 7 and 8, the light emission is due to charge carrier recombinations occurring in both the QD ensemble and the wetting layer[9] (WL).

[9] The WL is a thin quantum well.

4.1.1 Amount of Deposited Strained Material

Figure 14 displays spectra that were obtained from a wafer having an InAs coverage that was graded across the wafer during deposition. The details of the production of such a wafer shall be discussed in Chapters 6 and 7 where we shall describe similar samples which were produced for this thesis. Each spectrum was measured at a different point along the InAs coverage gradient. The peak visible between 1.40 eV and 1.45 eV is due to photo-emission due to charge carrier recombinations occurring in the WL,[10] and the group of peaks visible at lower energies are due to similar recombinations occurring in the QD ensemble. The excited state structure of the QDs is indicated by the identification of the peaks by their associated excitonic energy levels: s, p, d, f [54]. It can be seen that, as the InAs coverage increases above the critical coverage for 2D to 3D transition, the QD emission shifts to higher energies (blueshift), and that the WL intensity decreases. TEM measurements performed at different points found the following QD densities: at 1.89 ML, 8 QD/μm^2; at 1.91 ML, 32 QD/μm^2; at 1.96 ML, 90 QD/μm^2; in all cases, the QDs were approximately 20 nm wide [31].

Because the QD energy levels are energetically lower than those of the WL, the excitons created by the light stimulation across the beam spot tend to thermalise to QDs, where they then recombine, but some recombinations occur in the WL. The greater the number of QDs, the lesser the probability that excitons will recombine in the WL. Therefore, the intensity of the WL peak reduces relative to the QD peak intensity, as a function of increasing InAs coverage, due to the increase in QD density.

---

[10] InAs grows on GaAs in the Stranski-Krastanov growth mode; see Section 3.2.

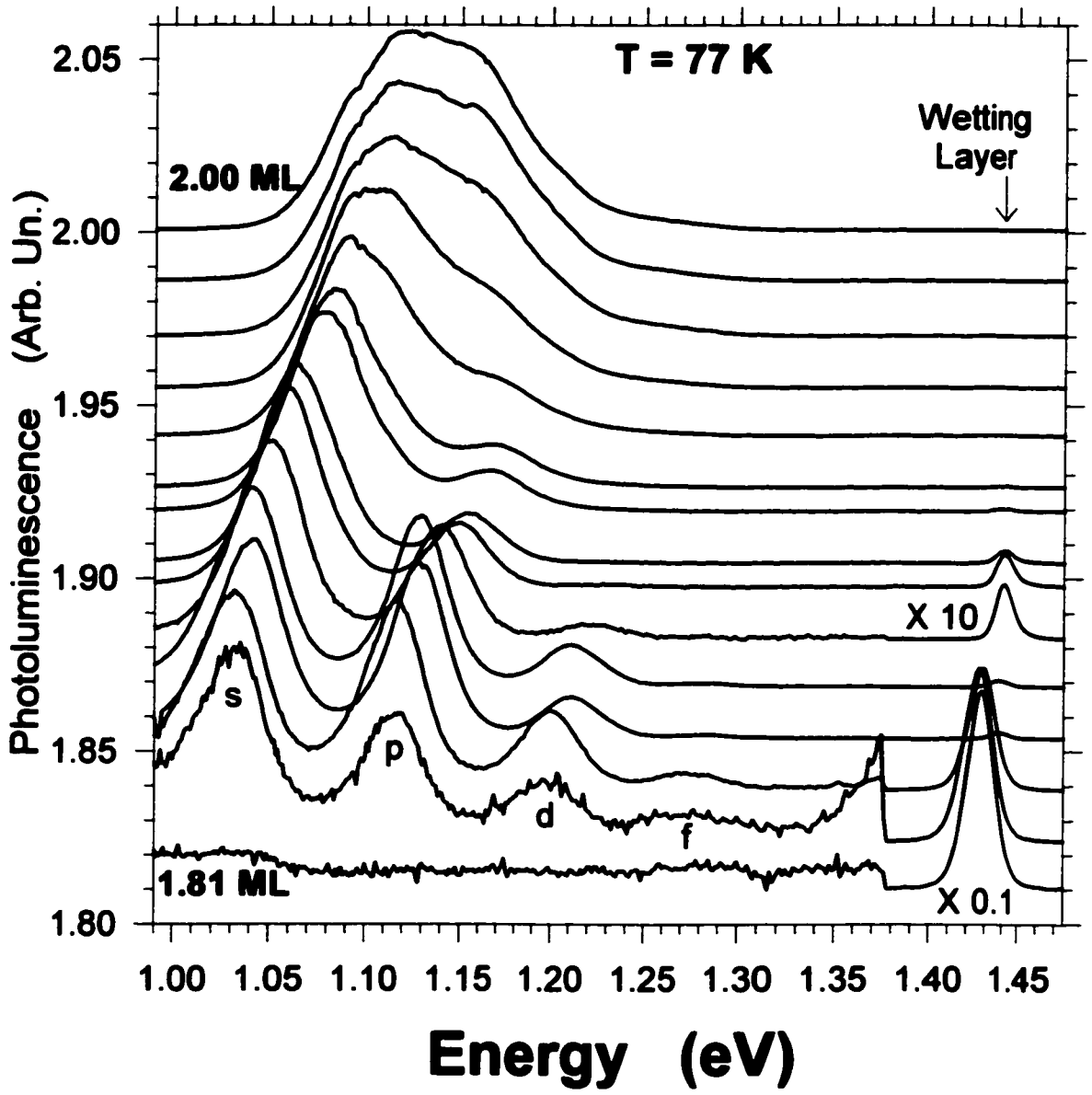

Figure 14. Evolution of the emission spectrum with the amount of InAs deposited for coverages between 1.81 and 2.00 ML. The state filling spectroscopy was obtained with PL at 77K, exciting above the GaAs barrier using an intensity of a few kW/cm^2. Each spectrum is offset to the value on the y-axis corresponding to the InAs coverage in ML. From ref. [31].

Figure 15 displays the WL peaks of spectra recorded from the same sample as those in Figure 14 but for a slightly reduced range of coverages. As seen in Figure 14, the spectra recorded at coverages lower than ~1.81 ML along the InAs coverage gradient did not exhibit any QD emission. The appearance of a QD emission in the spectra recorded at ~1.85 ML indicates that it is at this coverage that the 2D to 3D growth transition occurred. The WL peak shifts to longer wavelengths (redshift) before the 2D to 3D transition due to the increase in thickness of the WL. After the 2D to 3D transition, the WL blueshifts; this is due to the QDs "consuming" material from the WL in their nucleation (sudden blueshift at ~ 1.85 ML) and evolution (slower blueshift beyond 1.85 ML). The empirical relation of the WL thickness and its emission wavelength in Figure 15(b) can be used to determine approximately the final thickness of the WL and the amount of InAs that has been incorporated into the QDs. Using this relation, it was evaluated that as the total amount of InAs deposited increased from 1.85 to 1.89 ML, the amount of InAs incorporated into the QD ensemble quickly increased from 0ML, just before the 2D to 3D transition at 1.85ML, to approximately 0.42 ML. For deposited amounts greater than 1.89 ML, the WL thickness remained constant at 1.5 ML, and all the material deposited after the 2D to 3D transition went into the QD ensemble and not the WL. In Chapter 7, we will present results that demonstrate that this behaviour is dependent on arsenic pressure.

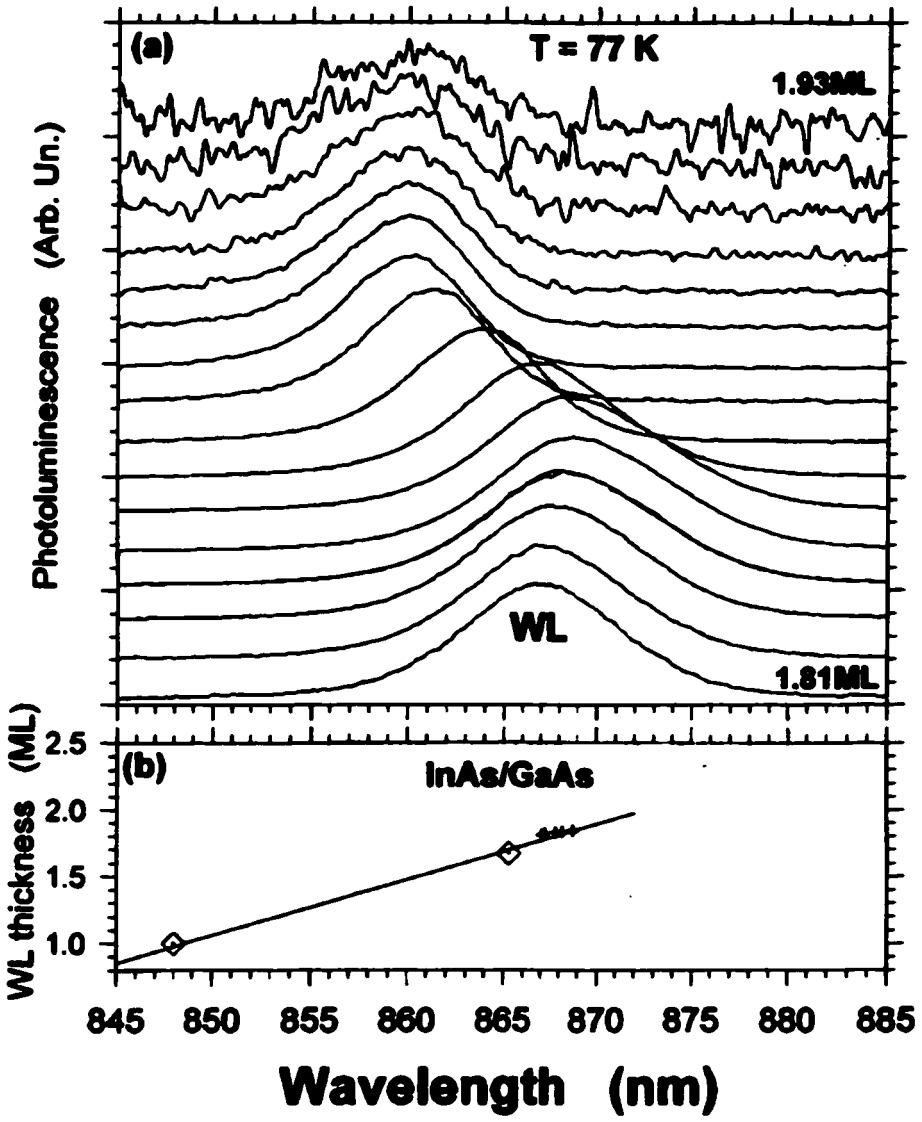

Figure 15. (a) Evolution of the WL emission with the amount of InAs deposited for coverages between 1.81 and 1.93 ML. (b) The relationship between thickness of the WL and its emission wavelength for the data prior to the sudden blueshift of the WL caused by the transfer of InAs to the QDs (crosses), for other samples grown separately (diamonds), and an empirical fit (line). From ref. [31].

Because the TEM measurements did not reveal any QD size evolution, the blueshift of the QD excited state structure was not interpreted as being due to a QD size evolution, but to the influence of the increasingly overlapping strain fields of neighbouring QDs on the QD electronic states, or to compositional effects. Therefore, it was interpreted that the amount of deposited strained material primarily controls the QD density.

In another coverage dependence study, Ledentsov and coworkers [35] grew InAs on GaAs by Molecular Beam Epitaxy at 480 °C and observed the following as a function of the amount of InAs deposited:

- At approximately 1.7 monolayers (ML), there is a transition from layer by layer growth to 3D InAs island growth.
- Between 2 ML and 4 ML, the islands were small, did not have crystalline facets, and the island size distribution was wide.
- At 4 ML the islands density was large, the islands had crystalline facets and a square base parallel to the [100] and [010] directions with an average lateral size of 140 Å.

At coverages smaller than 4 ML, growth interrupts[11] allowed the islands to reach the same equilibrium base size, 140 Å. The growth interrupt times as a function of coverage were: 10 sec for 3 ML, 40 sec for 2.5 ML, 100 sec for 2 ML. They had concerns [58] regarding the evaporation of InAs at 480 °C, specifically that an interrupt longer than 100 sec could lead to non negligible loss of In, alloying of the deposited InAs with the GaAs substrate, and even to migration of defects from the substrate to the epilayer. Importantly, they believed that their QD ensembles were in thermodynamic equilibrium, and that the equilibrium base size of the islands was 140 Å . The

[11] A growth interrupt is a step in a growth procedure during which deposition of material is interrupted, and after which deposition is resumed with the same material or another.

results of the IMS/NRCC group and the results presented in Chapters 7 and 8 do not show evolution towards a same base width independently of the amount of InAs deposited. The differences between the higher coverage (above 2 ML) samples of Ledentsov and our samples (below 2 ML) are probably attributable to the differences in amount of deposited strained material leading to different regimes of QD evolution as discussed in Section 3.3.1.

4.1.2 Growth Temperature

Figure 16 displays PL spectra that were obtained from a set of samples grown at different substrate temperatures; each spectrum was obtained from a different sample. The horizontal axis is the difference between the energy of the emission and the GaAs confinement barrier. The WL peak is visible between -100 meV and -50 meV, and QD peaks are visible at higher energy differences (i.e. lower E). Differently than in Figure 14, the QD excited state structure is indicated by a numbering of the peaks according to their associated electronic energy levels in the second spectrum from the top. It can be seen that as the temperature used during deposition and anneal of the InAs increases, the QD emission blueshifts, the energy spacing between the QD PL peaks decreases, and that the WL intensity decreases.

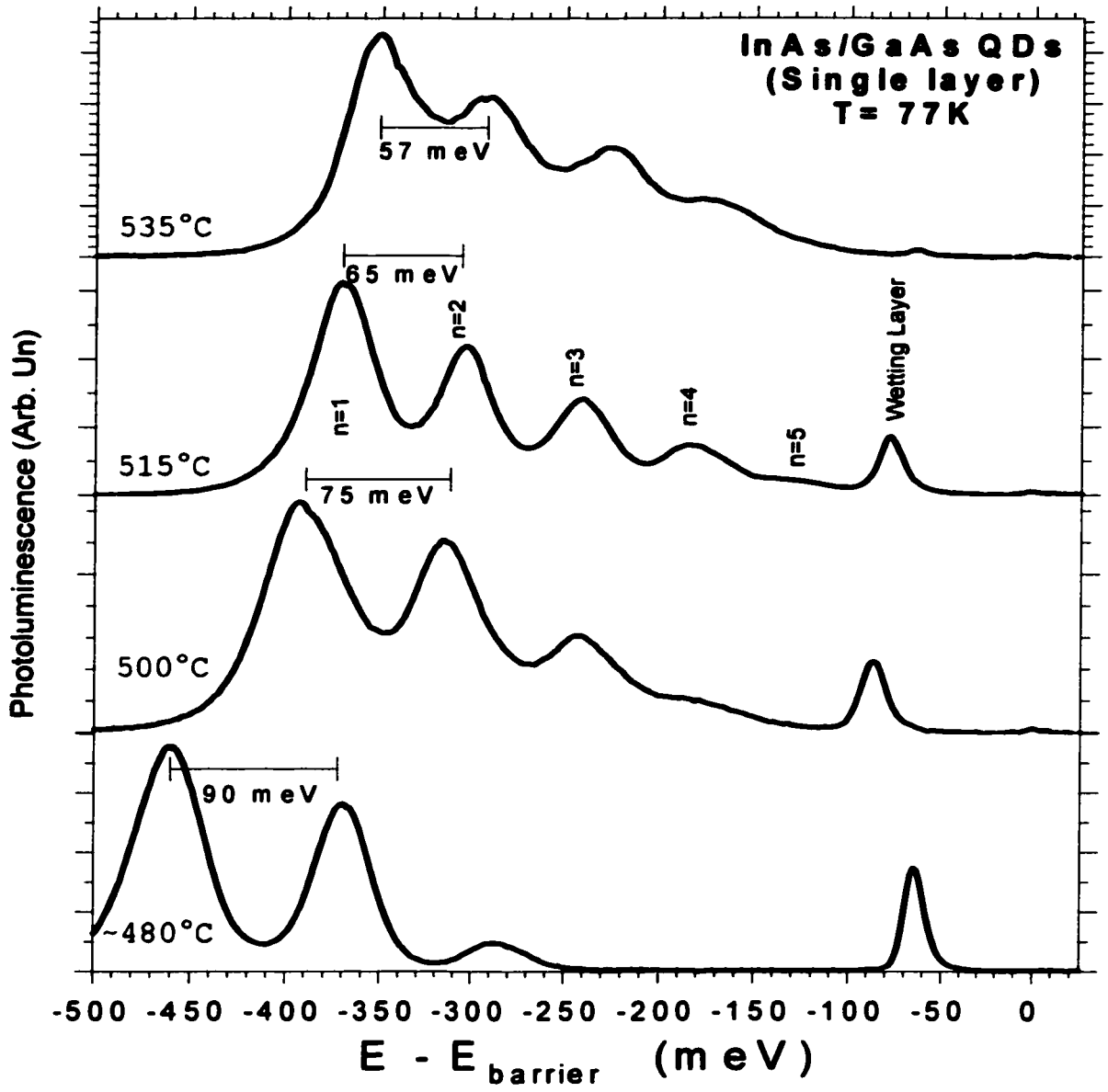

Figure 16. Evolution of the emission spectrum with the substrate temperature during growth: at 535 °C (A), 515 °C (B), 500 °C (C), and ~ 480 °C (D). The intersublevel spacings are indicated on each curve. The state filling spectroscopy was obtained with PL at 77K, exciting above the GaAs barrier (0 meV on the x-axis) using an intensity of a few kW/cm^2. From ref. [37].

Here again the reduction in the intensity of the WL peak is attributable to the increase in QD density. The pronounced change in QD PL peak spacing can be directly related to a change in the energy spacing of the charge carrier energy levels.[12] From these results and structural measurements performed by TEM, it was interpreted that, higher growth temperatures lead to larger QDs with smaller energy spacings, so that the size of QDs can be effectively tuned by adjusting the growth temperature [37].

Comparing TEM images of QDs produced at 530°C and 500°C, it was observed qualitatively that the 530°C sample had a higher density of larger QDs than the 500°C sample (both samples had a QD density of the order of 10^3 QDs/μm^2, and the difference is a factor of ~ 2). We would point out that because of this, it is difficult to conclusively attribute the shift in QD peak position to either size or density evolution of the QDs. Indeed, the trends predicted by the model presented in Section 2.3 and 2.4 suggest that a reduction in QD size should lead to a change in both position and spacing of QD energy levels. Most likely, the trends observed in PL are the combined effect of size and density evolution in the QD ensemble, with the possible additional influence of capping effects described in Chapter 9.

4.1.3 Anneal Time

Figure 17 displays spectra that were obtained from samples for which different annealing intervals were used after the formation of the QDs and before their capping. Each spectrum was

[12] As a rough approximation, it can be assumed that these energy differences between carrier recombination energies can de divided between the electrons and holes in proportion to the relative band offets, see Section 3.1.

obtained from a different sample. The WL peak is visible between 860 nm and 880 nm, and QD peaks are visible at longer wavelengths. The QD excited state structure is not labelled, but the peaks are related to excitonic energy levels in the same manner as those in Figures 14 and 16 (note the different x-axes, either wavelength or energy).

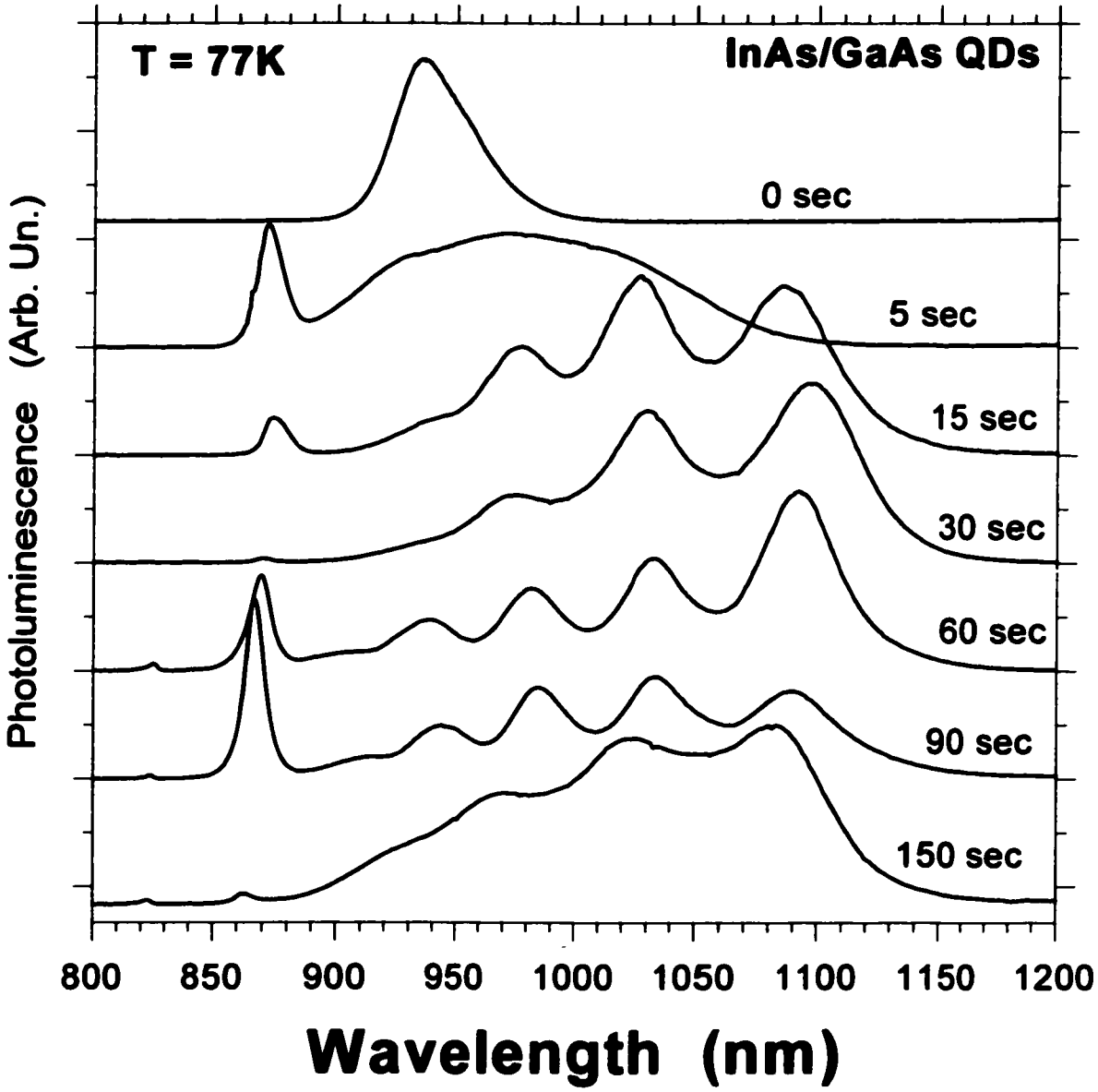

Figure 17. Evolution of the emission spectrum with the anneal time following the deposition of the InAs. The anneal times are indicated on the right hand side of each curve. The state filling spectroscopy was obtained with PL at 77K, exciting above the GaAs barrier using an intensity of a few kW/cm^2. From ref. [37].

The spectrum obtained from the samples with no annealing interval and with a 5 sec anneal show a broad feature instead of sharp energy levels. This indicates that after short annealing times, the QDs have not had sufficient time to evolve towards a sharp size distribution as that described in Section 3.4.2. After longer annealing intervals, up to 90 sec, the QD emission did not show considerable evolution. From this data it was not possible to ascertain whether this is due to thermodynamic equilibrium, kinetic limitations, or other effects.

The redshift of the broad structure, the slight redshift of the QD peaks, and the reduction in WL peak intensity observed up to 30 sec are attributable to the formation of the QDs as they nucleate and grow in size and number. After annealing for longer than 60 sec, there is a slight blueshift and a loss of resolution in the QD excited state structure; this is probably due to indium desorption leading to loss of QD material and possibly even to a reduction in QD density.

The annealing time together with the duration of deposition determine the span of time over which QD ensembles can evolve.

4.1.4 Post Formation Manipulation: "Indium Flush"

Figure 18 displays spectra that were obtained from samples that included an "Indium Flush" performed at different heights of partial capping. An *indium flush* is a specific type of discontinuous capping procedure[13] that involves interrupting the overgrowth of the QDs with the capping material at a height smaller than the QD height (partial capping). It is thermodynamically favourable for the

[13] Discontinuous capping procedures will be discussed in Section 4.4.

GaAs partial cap to bind to the WL. Because of the relaxation of the InAs after the 2D to 3D transition, the lattice constant on the surface of the QDs is close to the InAs bulk value. If the GaAs were to bind to the QDs, it would be strained considerably, and therefore the GaAs does not wet the QDs [38,59]. This leaves the QDs exposed and the WL covered with GaAs. Furthermore, as discussed in Section 3.1 the adhesion of InAs to GaAs is stronger than the cohesion of InAs to other InAs (which is the reason a WL forms in the SK growth mode, Section 3.2), as GaAs surrounds the QDs, InAs from the QDs diffuses onto the surrounding GaAs [38]. As the QDs reduce in height, the underlying and surrounding GaAs can bring the QD surface lattice constant closer to that of GaAs, at which point the GaAs partial cap can overgrow the QDs. This is followed by the flash-desorption of any InAs layer that has formed by indium migration onto the surface of the partial cap.

Each spectrum in Figure 18 was obtained from a different sample. The WL peak is visible between 860 nm and 880 nm, and QD peaks are visible at longer wavelengths. The QD excited state structure is not labelled, but the peaks are related to electronic energy levels in the same manner as those in Figures 14 and 16. For samples with the indium flush performed using a partial GaAs cap thinner than 2.0 nm (less than 1 ML of GaAs), it was reported that most of the InAs was evaporated. The QD emission redshifts with partial cap thickness increasing up to 8.5 nm of GaAs. Therefore, by using a partial cap ranging from 2.5 and ~ 8.5 nm to perform the indium flush, the shape of QDs can be adjusted from a flatter to a higher aspect ratio (height/width). The blueshift of the PL peaks of the QDs produced using an 11 nm partial cap was attributed to the intermixing of the QD and cap material.

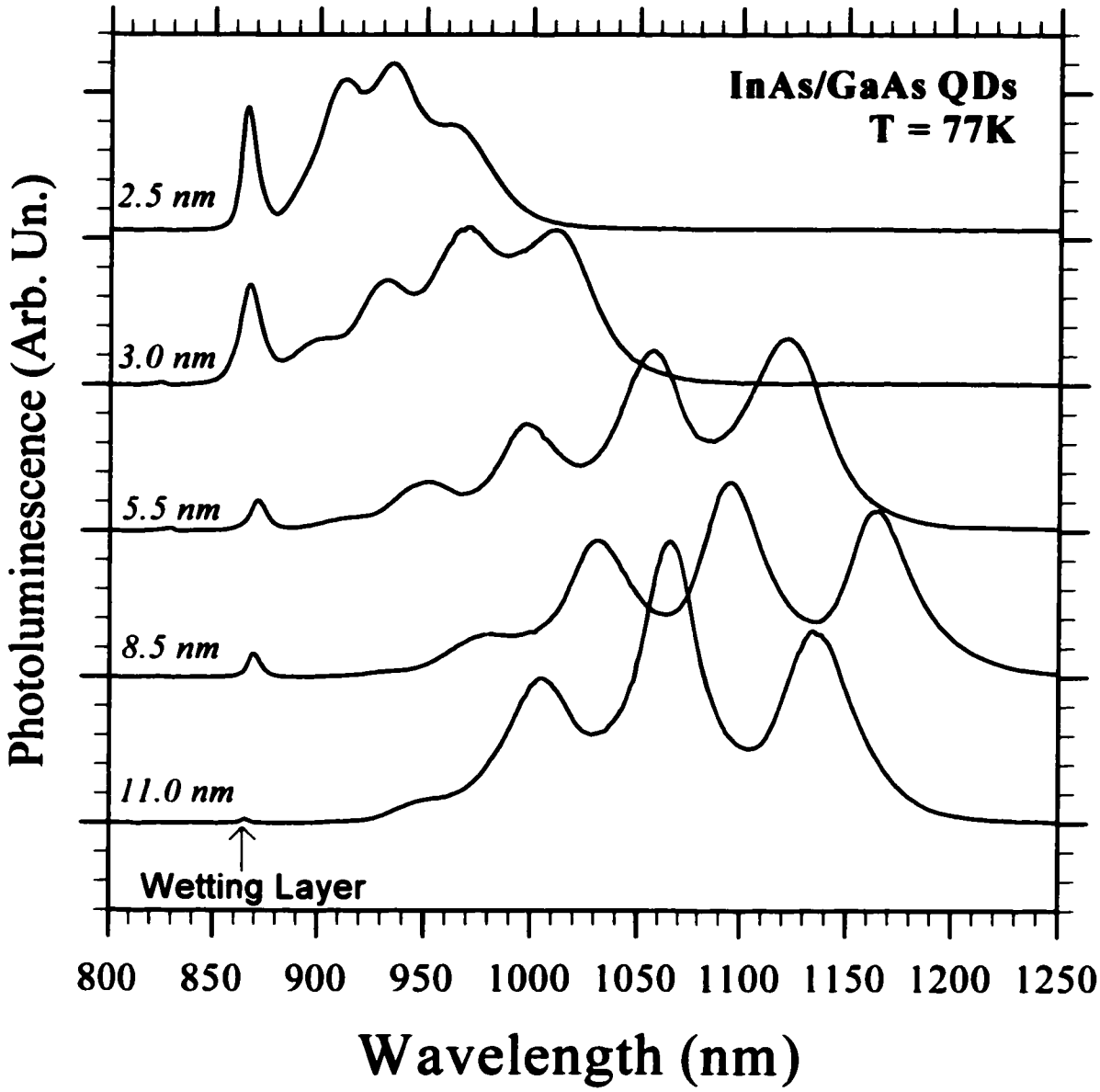

Figure 18. Evolution of the emission spectrum with indium flush executed after the deposition of a partial cap of GaAs of thickness between 2.5 and 11.0 nm. The state filling spectroscopy was obtained with PL at 77K, exciting above the GaAs barrier using an intensity of a few kW/cm^2. From ref. [37].

Figure 19. Cross-sectional TEM images of a stack of two indium flushed QDs (left hand side) and of a stack of two nominally identically grown QDs capped continuously. The central line indicates the height of the partial GaAs cap for the indium flush of the lower QD. The same height of partial cap was used for both QDs. From ref. [38].

Figure 19 compares stacked layers of QDs from samples that were similarly grown except for the use of an indium flush in one of the samples. It can be seen from these TEM images that the indium flush procedure reduces QDs to a desired height. The "imposition" of a selected height to all the QDs in an ensemble may also serve to improve ensemble size uniformity [38]. We shall further discuss this type of capping procedure when, in Section 4.3.2, we discuss discontinuous capping procedures more generally.

4.1.5 A General Remark Regarding Quantum Dot Growth Control Parameters

The growth control parameters described in the preceding sections were described to "primarily" control one ensemble property. The reason for this qualification is that, for this to be true, from growth to growth, the evolution of the ensemble must be stopped at the same point after the QDs have nucleated. This is, in great part, the reason for the differences between observations by our group at IMS/NRCC and Ledentsov et.al. They study QD ensembles produced with coverages

equal to approximately twice the critical coverage, whereas we stop the InAs deposition at the critical point for 2D-3D transition. As was mentioned in the previous chapter, it may be that this places our ensembles in a regime in which the system is kinetically "pinned" and their ensembles in a different regime where the kinetics bring the system to a point where thermodynamic equilibrium determines the state of the ensemble.

4.2 Group V Pressure Effect on Self-Assembled Quantum Dots

Although there are reports of arsenic pressure effects on QDs [44,60-65], no consistent trend emerges from the literature for MBE-grown InAs QDs. The MBE-grown QDs in these reports, in the context of the investigation of the arsenic pressure effects, do not show well-resolved multiple energy levels at any arsenic pressure. For metalorganic chemical vapor deposition (MOCVD) a detailed study has been reported [66], but due to the fundamental differences in growth processes, the trends reported therein are dissimilar to the results presented in this thesis.

The direct comparison of results in the literature is difficult due to the lack of common reference points in arsenic pressure, as well as the use of different growth techniques, deposition temperature, deposition rate, and total amount of strained material deposited. Microscopy studies of uncapped samples [61,62] showed an increasing QD density and decreasing QD size with increasing arsenic pressure. PL measurements of capped samples [60] consistent with these results revealed a blueshift of QD emission with increasing arsenic pressure. It has been suggested that these trends are attributable to an increase in diffusion length at low arsenic pressures [60,62]. In contrast,

at least one study produced the opposite trends [44]. Also, reports have been made of non-monotonic trends in QD density [52,66], and regimes in which QD formation appears to be completely inhibited [63-65].

Yasuda and coworkers [61], working with AFM images of uncapped InAs grown by MBE on the GaAs (211)B surface observed an increase in QD density with increasing arsenic pressure. At the lowest pressures and longest anneal times, they observed elongated (dash-like) structures instead of symmetrical (or nearly symmetrical) QDs. They suggested that it is unlikely that such a change in shape could occur without the presence of a kinetic barrier in the system. It is also conceivable for a change in surface energies to lead to a change in QD shape. They also reported a further increase in QD density as a function of increased anneal time, and an increase in QD size for very long anneal times (20 min). Importantly, the total volume of material in nanostructures increased with increasing anneal time, which they suggested could be due to alloying with the underlying material.

Ohtake and Ozeki, performing in-situ reflection high energy electron diffraction (RHEED) and total-reflection-angle X-ray spectroscopy on uncapped InAs grown by MBE on GaAs (001) reported that at low arsenic pressures and/or high substrate temperatures the formation of QDs is inhibited [65]. This is consistent with similar observations by Ledentsov and coworkers [63], and Mokerov and coworkers [64]. Using RHEED, Ohtake and Ozeki further observed that this inhibition of QD formation coincided with the surface displaying an arsenic-poor reconstruction, either (4×2), (8×1), or unreconstructed (1×1).

Leon and coworkers [52,66], working with InGaAs on GaAs (100) by MOCVD reported non-monotonic QD size and density variations associated with Ostwald ripening leading to a bimodal QD size distribution at high AsH_3 pressures. Using uncapped QD samples, they observed that the density of the smaller islands first increased and then decreased with increasing AsH_3 pressure, and that the density of the larger (Ostwald-ripened) islands followed the opposite trend. Furthermore, their measurements of the average island separations indicated that the diffusion length of group III adatoms was not, in this case, the limiting factor. The size of the non-Ostwald-ripened islands was nearly independent of AsH_3 pressure. They attributed the differences in island coverage to the thermodynamic driving force in Stranski-Krastanov island formation and the role of AsH_3 as an impurity-free surfactant. We note that the trends they observed in QD density, particularly the bimodal nature, differ from ours; in this regard, the different alloying tendencies of InGaAs and InAs on GaAs, the dissociation kinetics of AsH_3, and the nature of the active arsenic species on the surface may be of importance.

In Chapter 8 we present surface microscopy measurements correlated with PL spectra of QDs displaying well-resolved excited state structures. The well-resolved excited state structure allows for the clear identification of the trends in the QD ensembles as a function of arsenic pressure. Similarly to the work of Yasuda, Yamaguchi, and Chu, these results are consistent with the accepted dependence of group III diffusion length on group V pressure. In Chapter 9, we draw an approximate quantitative comparison with reported incorporation-diffusion lengths.

4.3 Adatom Incorporation-Diffusion Length Dependence on Group V Pressure

The incorporation-diffusion length (IDL) is a property of adatom diffusion: It is a measure of the distance over which adatoms travel on a surface before reaching a point of incorporation at a step edge or an island. In the general context of MBE growth of arsenic-based III-V compounds, it has been shown that the group V pressure affects the IDL of group III species. This is because the group V pressure affects the surface population of active group V species, which in turn affects the trapping probability of group III adatoms [67]. In this way, the group V pressure can limit mechanisms involving the diffusion of group III adatoms. During both GaAs [67-69] and InAs [70] homoepitaxy, increasing the arsenic pressure decreases the IDL of group III adatoms. The effects of such a trend on the growth of InGaAs on GaAs have also been reported [71]. The reduction in IDL with increasing arsenic pressure is attributable to the increased probability for a diffusing indium adatom to encounter an active arsenic species due to the increased surface population of active arsenic species.

For QDs, in addition to the kinetic mechanism discussed above, it is possible that changes in binding energies due to changes in arsenic pressure[14] may lead to changes in surface energies and in the state of thermodynamic equilibrium of the QD ensemble. In principle, both kinetic limitations and thermodynamics can influence QD size, shape, density, and composition. In practice, the annealing time together with the duration of deposition determine the span of time over which QD ensembles can evolve towards thermodynamic equilibrium at a rate determined by the reaction

[14] The change in surface population of arsenic atoms leads to a change in the average number of bonds per indium atom [72].

kinetics. The results presented in Chapter 8 are qualitatively consistent with the dependence of the IDL on arsenic pressure described above. This suggests that the diffusion mechanisms play a role in determining the QD density, so that in some growth conditions this property of InAs/GaAs QD ensembles is determined by kinetic limitations.

4.4 Capping Effects

Without the presence of a capping layer, the radiative recombination in QDs is greatly, if not entirely quenched. Even if we allow for the possibility of different means of surface passivation, device applications situate the active layer within a complex structure of layers producing desired opto-electrical properties. This implies that for most practical applications, the QDs are overgrown with some material.

GaAs, AlGaAs (for low Al compositions), and InP do not wet InAs QDs at typical growth temperatures [38,53,56,73,74]. This is due to the fact that the incoming flux of capping material arrives on an InAs surface consisting of both a WL and QDs. The WL complies to the compressive strain caused by the underlying material, but the QDs relax so that their outer surface lattice constant is much closer to the bulk InAs lattice constant [38,75]. The larger a QD, the more relaxed it is [58], and therefore the greater the difficulty for the capping material to overgrow it. In the case of InP islands capped with InGaAs, the situation may be reversed, and the capping material binds preferentially to the surface of the QDs [76].

Unlike GaAs, AlAs does wet both the WL and the QDs. This can presumably be attributed to a greater bond strength preventing the Al from migrating on the InAs WL+QD surface. The difference in bond strength can be seen by comparing the heat of formation of AlAs, GaAs and InAs, respectively -1.12, -0.74 and -0.61 eV/molecule [20]. Results reported by Arzberger and coworkers [77], suggest that by capping InAs QDs with a thin layer of AlAs before completing the cap with GaAs, the effects of mechanisms modifying QDs during capping are greatly reduced.

An important effect of the capping layer is the further straining of the QDs (their bases are already strained by the underlying substrate before capping) [78-80]. In the case of $In_{0.33}Ga_{0.66}As$ [78] and InAs [79] QDs capped by GaAs, it is estimated that the compressive strain from the surrounding matrix increases the energy gap of the QD material, leading to a blue shift of the QD emission lines by as much as a few hundred nm. Other important effects of the deposition of a capping layer include the loss of QD material and the alloying of the QD and capping material due to mechanisms such as the out-diffusion or evaporation of QD material, and the in-diffusion of capping material (intermixing). These effects can be amplified or attenuated, for instance, by adjusting the substrate temperature [37,81], changing the capping material [13,77], or interrupting the capping at a height smaller than or nearly equal to the height of the QDs [38,56], as discussed below. Also, the presence of the QDs can affect the growth of the capping material in the vicinity of each QD. Different QDs (size/composition) are expected to affect, and to be affected by, the capping material differently [56,82-84].

Discontinuous capping procedures, in which overgrowth of the QDs is interrupted for any purpose, elucidate how mechanisms leading to the loss of QD material affect larger QDs to a greater

extent than smaller QDs [38,53,56,81-86]. This is supported by structural and luminescence measurements, but importantly this is verified by transmission electron microscopy performed after the completed capping procedure (partial cap, interruption, completion of cap) for InAs on GaAs [38], and InAs on InP [53]. These measurements indicate that the reduction in size of the QDs is mostly, if not entirely, a reduction in height. The increased loss of material from larger QDs is attributable to two factors: because of their size, larger QDs are (1) more likely to be uncovered and (2) remain uncovered for a longer period of time.

It should be noted that, following discontinuous capping procedures, a reduction in QD density has been reported by some authors [56]. This can be attributed to the complete evaporation or out-diffusion of QD material from uncovered QDs during the capping interruption. In contrast, the QD density of capped and uncapped QD ensembles grown under the same growth conditions are similar [53,83], and we have found no reports of continuous capping affecting the QD density.

In summary, capping can affect the structure or composition of QD ensembles through several principal mechanisms: (1) the substantial modification of QD strain, (2) the out-diffusion of QD material or in-diffusion of capping material (during the overgrowth or after the QDs are completely covered), (3) evaporation of QD material, and (4) strain-induced preferential coverage by the capping material of either the QDs or the WL. The first mechanism, if the capping material increases the QD strain, will shift the energy levels to higher energies, and if the capping material reduces the QD strain, it will shift the energy levels to lower energies. The second mechanism, due to the interplay between bandgap changes in the QDs and the surrounding material, can be rather complex and can shift the energy levels to either higher or lower energies. The third mechanism can lead to a reduction in QD

size, shifting their energy levels to higher energies. The fourth mechanism can lead either to an increase, a reduction, or even a complete lack of covering of the QDs, and thus change the effect of mechanisms 2 and 3. The results presented in Chapter 8 suggest that these mechanisms in effect during the capping of InAs QDs with GaAs can modify a QD ensemble, structurally or compositionally, to the extent that the evolution trend set by a given growth control parameter can be reversed.

5 Growth Technique and Procedures

In this chapter we present the MBE reactor, the growth technique, and the growth procedures used in our study of self-assembled quantum dots (QDs). We then discuss the desorption of growth material constituents. This process is important in the growth of our samples, and in particular it can affect the quality of the material grown. This chapter concludes with a description of the general growth procedure used to produce our samples, taking care to explain how the growth control parameters are adjusted.

To study the effects of the arsenic pressure on the formation of QDs, we produced two series of samples; each will be discussed in a later chapter. All samples were grown at IMS/NRCC by the author; the three samples presented in Chapter 7 were grown by Dr. Simon Fafard and the author.

5.1 MBE Reactor and Materials

All growths were done in a modified V80H VG-Semicon MBE system shown in Figure 20 using the source materials: metallic indium and gallium, and a solid arsenic source set to produce As_2 or As_4. The substrates used were (001)-oriented GaAs epi-ready single-crystal wafers purchased from American Xtal Technology. Specifically, for the first set of three samples (Chapter 7), we used quarters[15] of two inch (50.8±0.4mm) semi-insulating (undoped) wafers indium mounted[16] to two inch

[15] Quarters were used instead of full wafers purely for purposes of economy.

[16] Indium mounting involves the placing a small amount of pure indium in between the sample and its mount. As the sample is heated in the MBE reactor, the indium melts, and the sample is held by surface tension.

silicon wafers, and for the second set of nine samples (Chapter 8), we used full two inch n-doped (Si doped, 1 to 3×10^{18}) wafers. Before growth, the substrates were thermally cleaned by outgassing at ~500°C in vacuum for one hour followed by approximately ten minutes at ~700°C under arsenic pressure to remove any surface oxide.

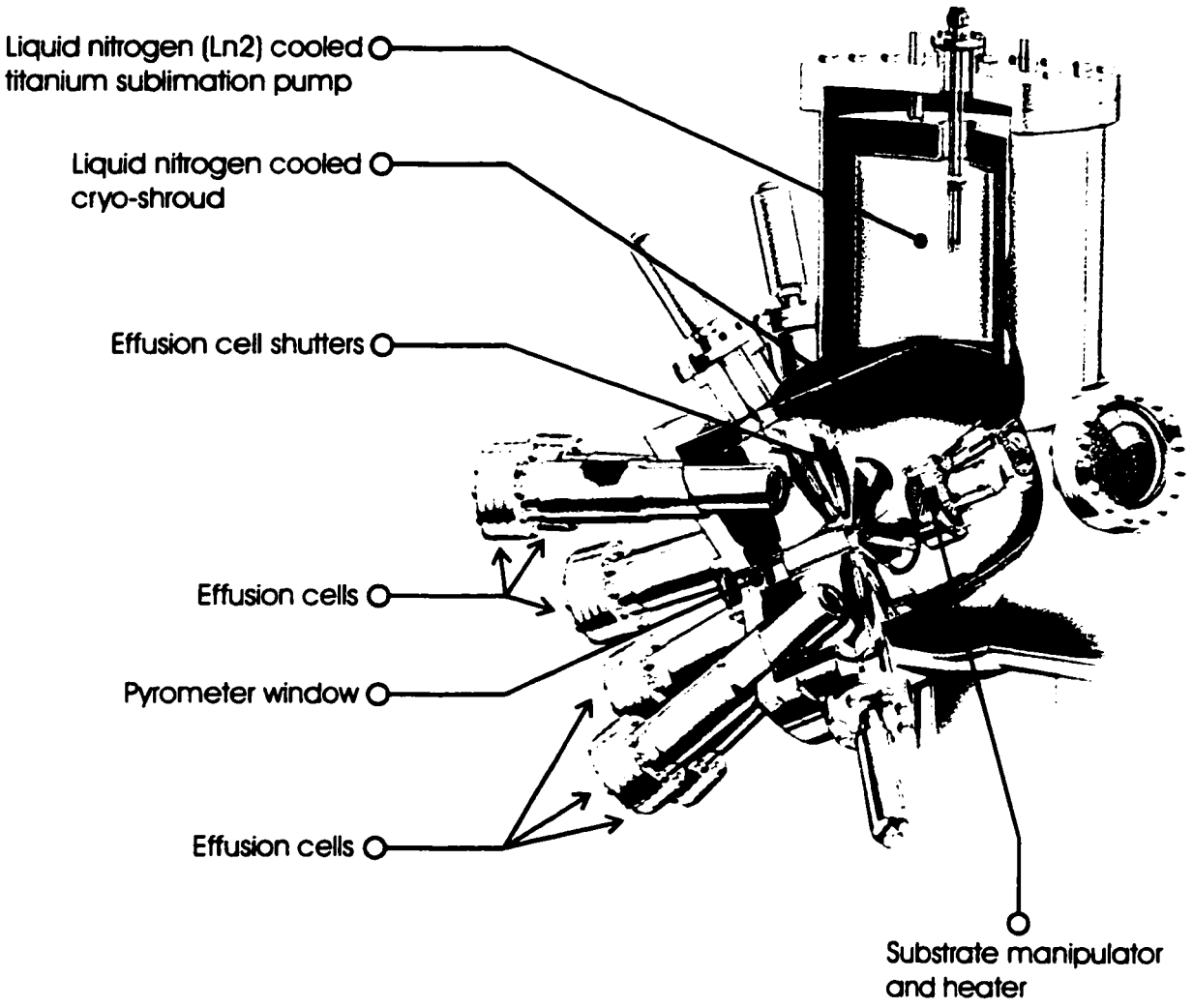

Figure 20: V80H VG-Semicon MBE system. The RHEED instrument (not displayed) which will be discussed in Chapter 6, consists of an electron gun and phosphor screen mounted on either side of the growth chamber, both in the plane of the substrate (parallel to the substrate heater and to the plane defined by the set of effusion cells). Modified from ref. [87].

Between growths, the system was kept in ultra high vacuum (UHV); in the growth chamber and preparation chamber the base pressure was maintained in the low 10^{-10} Torr range, and the partial pressure of important contaminants such as carbon and water were kept below the 10^{-11} Torr range. For a potential contaminant having a partial pressure equal to 1×10^{-11} Torr, assuming unity sticking coefficient, it would take approximately fifty hours to deposit one monolayer onto a surface, and about thirty minutes to contaminate a substrate with 1% of a monolayer. The UHV conditions required to keep the system, including the sources and manipulator, free of contaminants are maintained by the use of cryopumps and a liquid nitrogen cooled shroud lining the growth chamber. To reach UHV pressures, pumping alone is not sufficient. Immediately following atmospheric exposure, it is necessary to heat, or bakeout the vacuum chamber to accelerate the outgassing of materials deposited on the chamber walls and all the equipment. The growth temperatures discussed above also serve to reduce the sticking coefficient of potential contaminants.

During growth, the substrates were held in molybdenum holders placed in a rotating stage. The rotation in combination with the off axis position of the sources serve to improve the uniformity of the epitaxial deposition. The sources consist of effusion cells equipped with pyrolitic boron nitride (PBN) crucibles optimised for deposition uniformity [88] in which the indium and gallium are heated above their melting point. The fluxes necessary for our growths required setting the source temperatures to ~ 800 °C for indium and ~ 1000 °C for gallium. The arsenic source used in our experiments is a 500 cc Applied Epi Valved Cracker effusion source. In this source, solid bulk arsenic material is heated to ~ 450 °C, and the flux generated then passes through a hot region, a Rhenium "cracker" which when set to 400 °C predominantly produces As_4 and when set to 950 °C predominantly produces As_2.

After the oxide removal at ~ 600°C to 630°C, for the different growth steps described in detail in Section 5.4, the substrate temperature was maintained between ~500°C and ~600°C. The heater element, which is situated behind the wafer in the substrate manipulator, consists of tungsten wire placed in a groove in a PBN plate acting as a heat diffuser, as well as a support and electrical insulator for the wire. This diffuser plate, in addition to the rotation of the substrate, serves to reduce thermal gradients across the substrate. A thermocouple mounted in a double ceramic tube passes through the PBN diffuser plate such that the tip of the thermocouple is positioned between the PBN plate and the wafer. The thermocouple temperature was monitored by Eurotherm 818 Controller/Programmer which, using this temperature as a reference signal, controlled the power applied to the heater. The substrate temperature measurements quoted in our measurements were made using an SVT Associates In-Situ 4000 optical pyrometer aimed at the substrate surface.

The main pressure gauge in the growth chamber was an ionisation gauge degasable by electron bombardment. Background gases were identified, and their partial pressures were measured using a residual gas analyser (quadrupole mass spectrometer). Pressure readings can also be made using the residual gas analyser, but because of outgassing and conductance considerations the ionization gauge gives a better evaluation of the chamber pressure. The main ionisation gauge was verified to be linear with the arsenic flux coming from the arsenic valved cracker cell by placing a second, retractable ion gauge in the position normally occupied by the substrate during growth procedures and directly measuring the arsenic flux. Furthermore, during our experiments the partial pressure of all other materials or contaminants in the growth chamber was negligible compared to that of arsenic, as verified using the residual gas analyser. Therefore, the total pressure in the growth

chamber, as measured by the main ionisation gauge was recorded as the arsenic pressure in the chamber during the growth procedures.

In the following sections, we discuss the calibration of the reference points of the dependent and independent parameters in our study. In the final section, we give a general description of the growth procedures used to produce the two sets of samples discussed in Chapters 7 and 8.

5.2 Desorption of Growth Material Constituents

We shall now introduce the concepts of adsorption and desorption in some detail. We do this because the physical principles involved are relevant both to the growth process and to the technique of thermal desorption spectroscopy (of which we shall make qualitative use later on).

Adsorption is the bonding of molecules or ions onto a surface. By bonding we mean that due to some interaction there exists a potential well with a minimum a few angstroms from the surface that "traps" the adsorbing particle onto the surface. The minimum of this potential well can be considered to be a bond energy. When a surface is exposed to a flux during growth, each molecular impact has a certain probability, expressed by a sticking coefficient, of leading to an adsorption event. The number of molecular impacts per unit area and unit time and the sticking coefficient determine the rate of adsorption.

Desorption is the activated process by which an adsorbed molecule leaves the surface. In keeping with our simple picture of trapping in a surface potential well, some mechanism, say a phonon mediated process, transfers energy to the adsorbate, and when this adsorbed particle is sufficiently excited it leaves the adsorbate and returns to the gas phase in contact with the substrate. Plots of the flux of desorbing gas versus the substrate temperature are called thermal desorption spectra. In Sections 5.3.2 we show thermal desorption spectra of indium on GaAs.

Epitaxial growth is performed at temperatures at which the evaporation of at least one of the components may not be negligible. The rate of desorption of a surface species can be expressed by the Arrhenius form:

$$\frac{d\theta}{dt} = -\nu \cdot \theta^n \cdot e^{-E/kT} \tag{28}$$

where θ is the surface coverage of the desorbing species, n is the order of reaction, v is a prefactor with units of seconds^{-1}, T is the substrate temperature, and E is a binding energy. In one picture of the desorbing particle, the surface, combined with the bulk, acts as an infinite thermal bath. In this picture of desorption kinetics, the prefactor in the Arrhenius form is taken to be an attempt frequency along the surface normal. In a microscopic theory, the prefactor has a more subtle meaning, including the transition probabilities into the gas phase from the energy levels in the adsorption potential well, which may be dependent on surface coverage.

In homoepitaxy, the adsorption energy for gallium on GaAs is 4.8 eV, and the adsorption energy for indium on InAs is 4.0 eV [72]. The presence of an adsorbate on the surface of some materials, or a change in surface population of an adsorbate whether it is a constituent species of the

underlying surface or not, can cause a surface reconstruction (i.e. a repositioning of the atoms at the free surface). As will be shown in Chapter 6, the surface reconstruction of GaAs is dependent on the surface coverage of arsenic.

There is another important characteristic of adsorption/desorption phenomena that we should mention: dissociation. In certain cases it is energetically favourable for an adsorbing molecule to dissociate during the adsorption reaction. In the InAs/GaAs system the active arsenic species on the surface is believed to be As_2, and therefore it is believed that As_4 dissociates to As_2 either by a first order or second order dissociation reaction [67].

5.3 General Growth Procedure and Adjustment of the Growth Control Parameters

We produced two series of samples, and all have the same basic growth structure. Growth parameters (i) to (iii) listed in Section 4.2 were optimised to produce well-resolved QD energy shells and kept nominally identical throughout both series. The specific values used for each of the growth control parameters, substrate temperature, InAs coverage, and arsenic pressure, as well as how these values were selected is discussed in the following sections. The details of the growth procedure for each of the two series of samples are described in Chapters 7 and 8. The sections in which the growth details are discussed are indicated in parentheses throughout.

Referring to Figure 21: Following the oxide removal (Chapter 5), a GaAs buffer layer was deposited to bury any contaminants that might remain on the surface of the de-oxidised wafer and to

provide a smooth growth surface. On top of the buffer, the desired coverage of InAs was deposited and annealed, leading to the formation of the QDs (Section 6.3.3). Then this layer was overgrown with a GaAs cap. A different capping procedure was used for each set of samples (Sections 7.1 and 8.1). The main differences between the two series are: (1) for the first series, consisting of three samples, the InAs coverage was graded (Section 7.1) and (2) for the second series, consisting of nine samples, a second layer of InAs was deposited on top of the GaAs cap (Section 8.1) for the purpose of performing surface microscopy measurements.

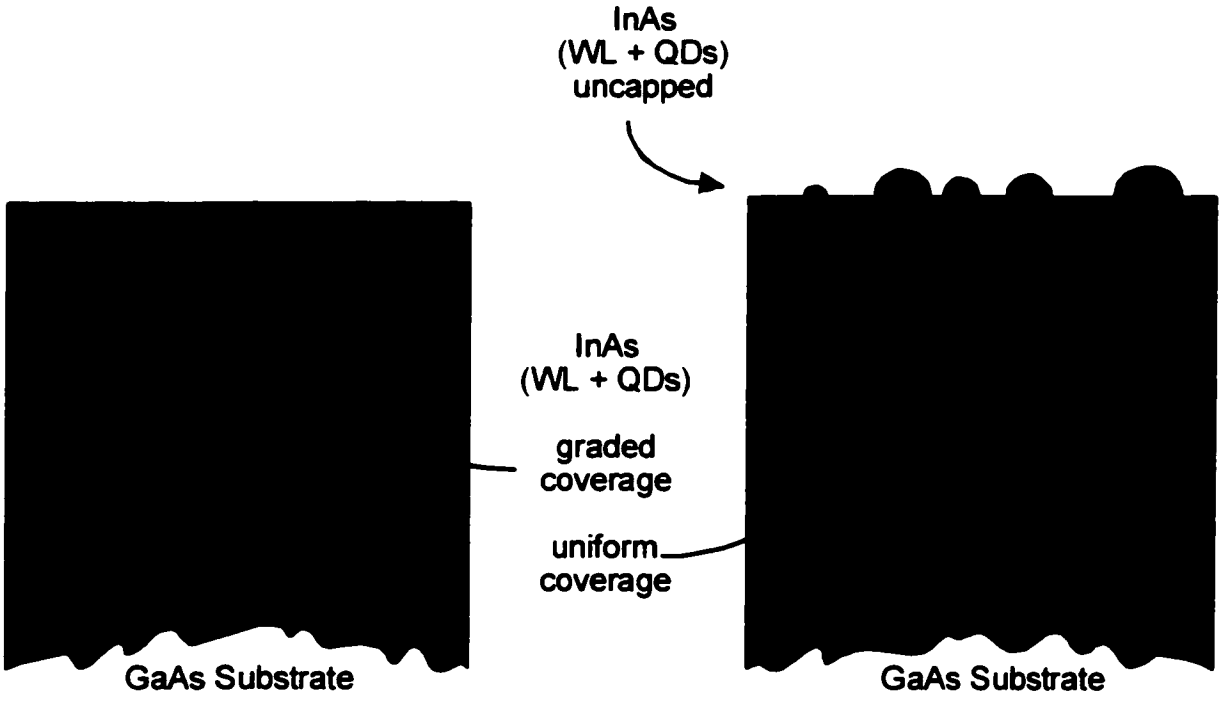

Figure 21: The growth structures discussed in Chapter 7 (left hand side) and Chapter 8 (right hand side).

In the following sections, we shall discuss the GaAs growth rate, substrate temperature, InAs growth rate, and the arsenic pressure. Particularly, we shall justify the specific values or reference values used in these experiments.

5.3.1 GaAs Growth Rate

The growth rate of each material used in the MBE reactor, including GaAs, is calibrated by X-ray characterisation of superlattice structures. Furthermore for GaAs, at approximately weekly intervals these calibrations are verified and adjusted using the optical pyrometer by measuring the reflectivity oscillations during the deposition of thick layers (order $\lambda/4$) alternating AlAs and GaAs [89]. This second operation is not possible for InAs because the light absorption coefficient is too large, so that not even a single complete oscillation can be measured.

The deposition rate for GaAs was ~ 0.2 nm/sec.

5.3.2 GaAs and InAs Deposition Temperatures

The GaAs was grown at ~ 600°C; this gives a smooth surface morphology while limiting the desorption of gallium from the surface.

The InAs layers where grown at ~ 515°C. Maximising the substrate temperature during the deposition and annealing of the InAs maximises the indium diffusion length [69] and therefore increases layer uniformity. Looking at the Arrhenius form in equation 28, we can deduce that the practical limit to the substrate temperature for these steps in the growth procedure is the desorption of InAs. As stated in Section 5.2, the adsorption energies for GaAs and InAs homoepitaxy are 4.8 eV and 4.0 eV respectively [72]. It can therefore be expected that the chemical contribution to the

indium binding energy in heteroeptaxy of InAs on GaAs neglecting strain, ϕ_β^α in equation 27, is in that range. The actual value will depend on the number of bonds involved in the trapping of the indium atom; for instance, the number of arsenic atoms bonded around or on top of the indium would change the binding energy. Figure 22 presents desorption spectra for three initial InAs coverages: 0.5, 1.0 and 1.5 ML. These thermal desorption spectra are too noisy[17] to allow quantitative analysis [90], but we can see that 515°C is approximately the highest substrate temperature at which InAs can be deposited without leading to a considerable desorption of the InAs.

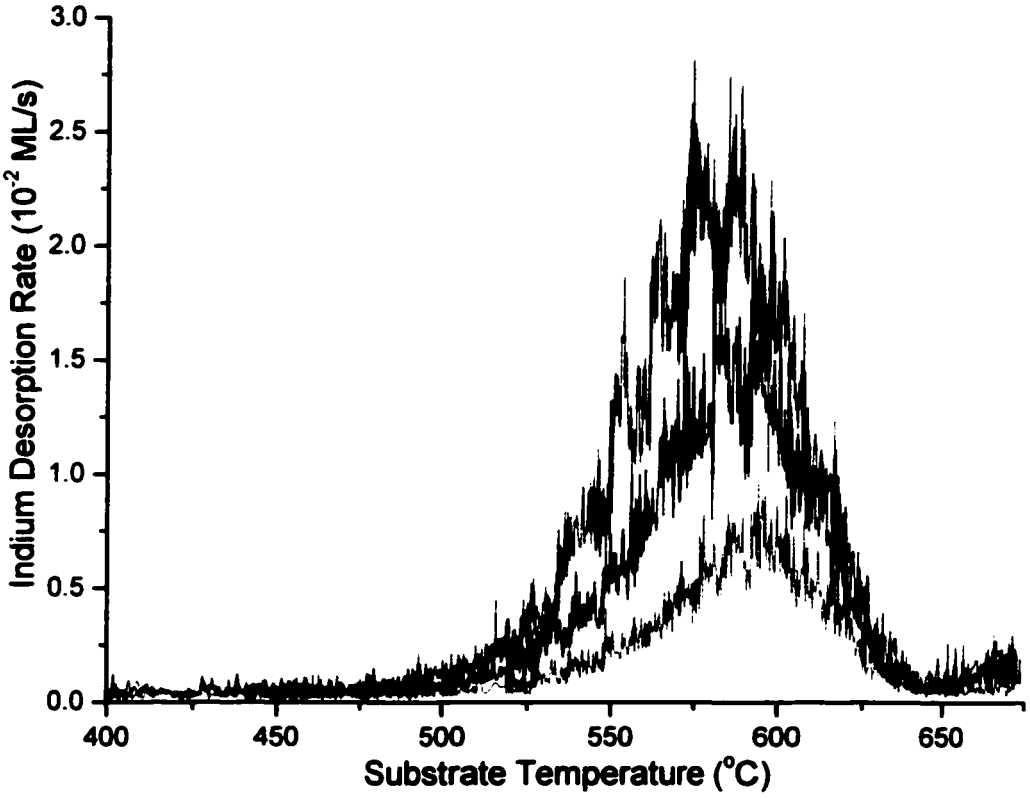

Figure 22. Thermal desorption spectra of InAs on GaAs for the following InAs coverages: 0.5 ML (red), 1.0 ML (black), 1.5 ML (blue). The substrate was heated at 1 °C/sec. The periodic (over ~ 10 °C) noise in each curve is due to fluctuations in the power applied to the substrate heater by the temperature controller.

[17] The noise in the data is in part due to the rotation of the wafer, fluctuations in the power applied to the substrate heater, and the positioning of the residual gas analyser.

5.3.3 InAs Flux/Coverage

The coverage studies performed at IMS/NRCC reviewed in Section 4.2 determined that QD ensembles produced at coverages exceeding the critical value for 2D to 3D transition, but as close to this value as possible, have the best-resolved excited state structures. Therefore, based on this, both in the case of the samples presented in Chapter 7 and 8, the QDs were formed by depositing 1.9 monolayers of InAs. In order to allow good control of the amount deposited for the formation of the QDs, the InAs growth rate used was 0.02 nm/sec.

The flux from effusion cells can fluctuate by approximately ±1% per day. To compensate for these day to day fluctuations in the indium source, an easily available measurement of the flux is required. Reflectivity oscillations such as those used in the weekly re-calibration of the gallium flux, as explained in Section 5.3.1, cannot be utilised in the case of the indium source. The RHEED movies presented and analysed in Section 6.6 provide a signature of the 2D to 3D transition. Measuring the transition time at a set substrate temperature and arsenic pressure provides the necessary flux re-calibration.

5.3.4 Arsenic Pressure

The goal of this study was to observe the effects of the arsenic pressure on the formation of InAs QDs. As discussed in Section 4.2, to compare results from different experiments, it is essential to have a readily determined reference point in arsenic pressure. Using an absolute pressure

measurement from an ion gauge for instance does not provide sufficient "portability" of the reference point to another growth system (or even to the same growth system if the equipment configuration is at all changed); this is due to the fact that such a pressure measurement is strongly dependent on gauge positioning. Similarly, the "beam equivalent pressure" measured by placing an ionisation gauge in the path of the flux of each source will also be dependent on gauge positioning, although more weakly so. The difficulty is resolved by using a measurement that is not directly related to the arsenic pressure but rather an effect of the arsenic pressure.

We reference all arsenic pressures with respect to the arsenic pressure, P_0, providing the minimal flux needed to sustain an arsenic-stabilized surface reconstruction during GaAs growth at 0.2 nm/s and 600 °C as determined by RHEED.[18] This is also the minimum pressure required to grow stoichiometric GaAs at 2 Å/s and 600 °C. It is determined by setting the substrate temperature and GaAs effusion cell to the desired set point, and iteratively reducing the arsenic pressure (of either species) and initiating the growth of GaAs. The surface reconstruction is observed in real time using RHEED, and the highest arsenic pressure at which the unreconstructed (1×1) surface is observed without any sign of the (4×2) reconstruction is recorded and used as P_0. The appropriate P_0 value was used for each arsenic species, As_2 or As_4 which are respectively used in the growth of the samples discussed in Chapter 6 and 7.

As stated earlier in Section 5.1, the main ionisation gauge was verified to be linear with the arsenic flux much in the usual manner in which beam equivalent pressures are determined. A

[18] The ion gauge used throughout the experiments recorded a value of 7.0×10^{-8} Torr for As_2 and 2.0×10^{-7} Torr for As_4. These translate to values at the substrate of approximately 1×10^{-4} and 6×10^{-4} Torr for As_2 and As_4 respectively; these values were measured using a retractable ion gauge placed in the position normally occupied by the substrate holder during growth procedures.

retractable ion gauge was placed in the position occupied by the substrate during growth, and the pressure reading of both the main ionisation gauge (used for measurements during actual growths) and the retractable gauge were recorded. The reading of the main gauge was determined to be proportional to the arsenic flux coming from the arsenic valved cracker cell.

The arsenic pressure was adjusted for the deposition of the InAs layers, but the growth of the GaAs buffer and cap layers required that the minimum arsenic pressure for stoichiometric GaAs growth be maintained. Therefore, rapid adjustment of the arsenic pressure for the designated growth steps was achieved by adjusting the valve of the valved arsenic cracker cell.

6 Characterisation of Growth Surfaces

In this chapter we present characterisation measurements of the surfaces onto which growth is initiated, as well as of the surfaces observable during the deposition of the growth materials. The identification of the reconstruction of the GaAs surface onto which the growth takes place is essential. The surface reconstructions vary according to the temperature and arsenic pressure utilised, and this relates to the surface stoichiometry. During growth, it is essential that the surface be kept arsenic rich; this assures good material quality. Furthermore, as will be of key importance in our discussion in the last chapter of this thesis, the proper identification of the surface reconstruction can serve as a guide for relating the temperature/arsenic-pressure used in our experiments to those used in other experinments.

For the purpose of growth surface characterisation, two main techniques were used: LEED (ex-situ) and RHEED (in-situ). Since both these techniques are electron based, and since in Chapter 8 we shall present SEM measurements, we will discuss the interaction of electrons and surfaces in some detail. Following this, we will introduce the principles behind LEED and RHEED. Following this, because the LEED measurements were performed ex-situ, we will describe the transfer procedure which was required to minimise surface contamination during transport due to exposure to atmosphere. We will then present together the measurements that were performed with both techniques. In the last section, we will present real-time RHEED movies of quantum dot (QD) growth.

6.1 Electrons and Surfaces

Due to their surface sensitivity, electron based probing techniques are a mainstay of surface science research. Because of their shallow penetration depth, electrons having a kinetic energy between about 5 and 2000 eV detected coming from a material, regardless of the mechanism by which they were generated, must originate from the surface region. The high probability of inelastic scattering of low energy electrons inside a solid ensures that electrons coming from deeper regions of the material fall outside the energy window of detection, such as the elastic peak in LEED (Section 6.3) or a specific inelastic peak in Auger Electron Spectroscopy (AES) (Section 6.2).

There are two main types of energy loss mechanisms in operation: single particle electronic excitations, and plasmon scattering. The first of these two can further be divided into two categories: excitations of valence electrons, and excitation of core electrons. The contribution to the mean free path by the interaction with core electrons (mainly due to the repulsion from the outer shells) is generally about two orders of magnitude smaller than that for either plasmon scattering or valence electron excitation. It is therefore the combination of plasmon scattering and valence electron excitation that is the cause for the surface specificity of electron probes. Elastic scattering contributes by increasing the mean travel distance in the material by reflecting outgoing electrons away from the surface, and although this in itself does not reduce the probability of escape, it increases the probability of the other interactions. We therefore speak of attenuation depth instead of inelastic scattering mean free path. We will not go into greater details about this since it is not central to this thesis, but we do include a graph of the attenuation depth versus energy (see Figure 23, the scatter in points is material-dependent).

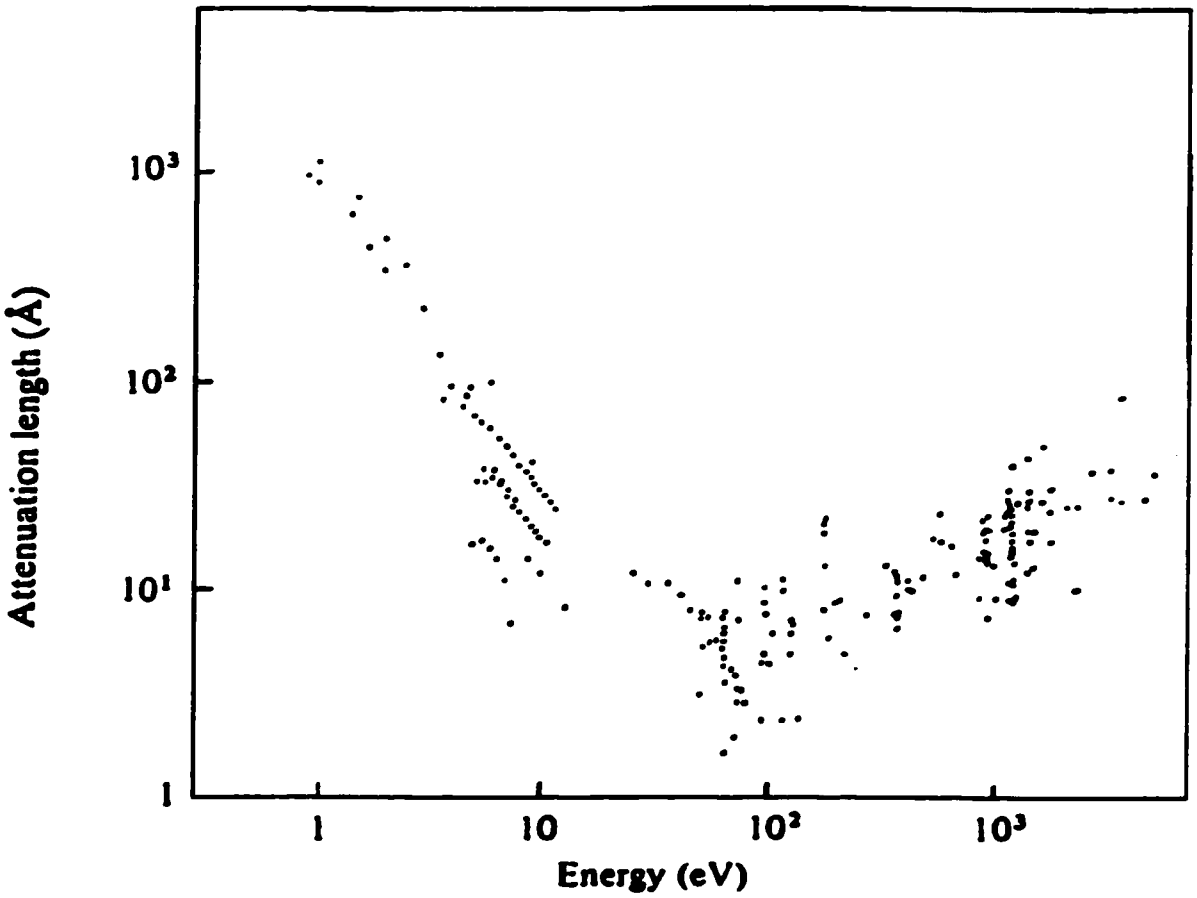

Figure 23: Collection of experimental determinations of attenuation length as a function of energy above the Fermi level for many different materials (after Seah & Dench, 1979). From ref. [91].

6.2 Auger Electron Spectroscopy

What we have discussed up to now in Section 6.1 is relevant to all electron based techniques, and we shall return to some of these points in the following sections when discussing LEED and RHEED. In this section we continue our discussion of the interactions of electrons with surfaces paying particular attention to a specific inelastic process: the interaction with core electrons leading

to the emission of Auger Electrons. Although it is not a quantitatively important energy loss mechanism, this process is the basis of Auger Electron Spectroscopy (AES). AES is a core level spectroscopy used for surface chemical composition analysis. In Section 6.4, we shall make use of this technique to measure the arsenic surface population on samples that were prepared for ex-situ LEED measurements.

Atoms in a material impinged upon by electrons or X-rays of energy ≥ 1500 eV may be ionized by losing a core level electron. After such an ionization, an atom may relax by filling the empty core level with an electron from a higher level, and this will be accompanied by the emission of a photon, or an electron. The electron emitted in the second possibility will originate from a level near in energy to the level of origin of the electron that filled the core hole. Electrons emitted in this process are called "Auger electrons". The core hole decay is represented schematically in Figure 24.

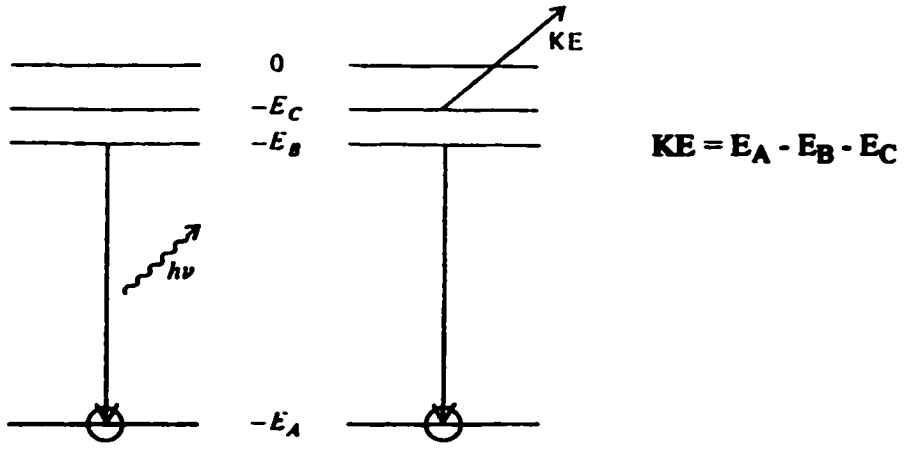

Figure 24: Energy level diagram showing the filling of a core hole in level A, giving rise to (X-ray) photon emission on the left, or Auger electron emission on the right. The levels are labelled with their one-electron binding energies. From ref. [91].

For core hole depths of less then about 10 keV, that is, relatively shallow core levels, the "Auger process" will dominate over the photonic process, and we therefore have an electron spectroscopy as opposed to a light spectroscopy. The core level, as well as the shallower levels are characteristic of the atom involved, and it is therefore possible to identify the atom. (The shallower levels can be core or valence; the core levels, being less affected by chemical shift are often more useful in this spectroscopy, but valence levels can still be used in the fingerprinting of atoms.) Auger electrons form a discrete spectrum on top of the smoothly varying background of backscattered/secondary electrons. We shall discuss backscattered and secondary electrons in detail in Chapter 8 where we present SEM measurements.

6.2.1 AES Instrument

The AES apparatus we used is from Perkin Elmer, and consists of a model 10-155 Cylindrical Mirror Analyzer (CMA) and electron gun control. The CMA is a system of electrostatic lenses made of concentric cylinders. An electron gun sends a monoenergetic beam of electrons ($\sim 10^3$ eV) onto a surface, and the CMA selects the energy of the returning electrons (less than the incident beam energy). Intensity spectra of the backscattered electrons are recorded and subsequently differentiated for analysis.

6.3 Low Energy Electron Diffraction and Reflection High Energy Electron Diffraction

Low Energy Electron Diffraction (LEED) is a diffraction technique involving elastically scattered electrons, as shown in Figures 25 and 26. It is the surface technique analogous to X-ray diffraction in the bulk. Looking back at Figure 23 we can see that electrons having energies between 10 and a few 10^2 eV have an elastic mean free path smaller than about 10 Å. On the scale of crystalline lattice constants, this represents about 2 to 4 atomic layers; this renders electron based techniques operating at such energies essentially "blind" to depths greater than a few atomic layers, and because of this we can say that effectively the system probed has only two dimensional periodicity. These energies also coincide with the energy required for electrons to have a de Broglie wavelength of the order of lattice constants.

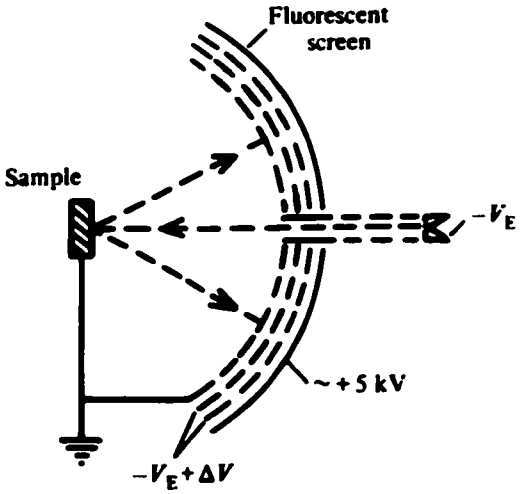

Figure 25. Schematic representation of Low Energy Electron Diffraction (LEED). From ref. [91]. V_E is the electron beam energy.

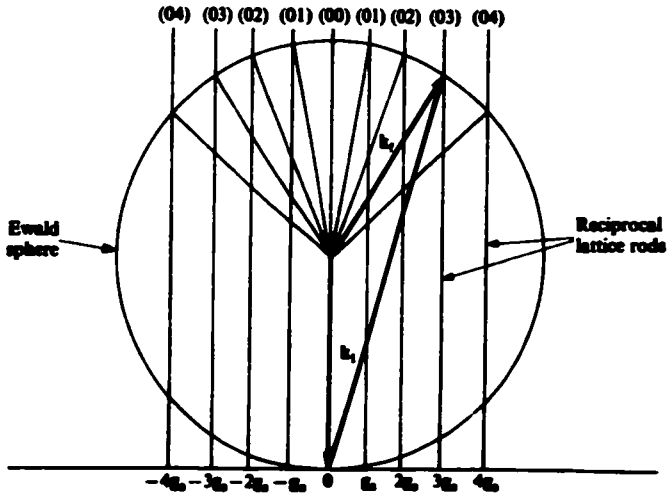

Figure 26. Representation in k-space of LEED. From ref. [92]. The $\mathbf{g}_s$ are the reciprocal surface lattice unit vectors, and $\mathbf{k}_i$ and $\mathbf{k}_f$ are the incident and diffracted electron beam.

Reflection High Energy Electron Diffraction (RHEED) is the most commonly found characterisation tool found mounted to MBE reactors. RHEED is performed using high energy electron beams (~ 10 to 20 keV) at grazing incidence, see Figures 27 and 28. This near parallel geometry leads to the surface sensitivity at such high electron energies. This geometry results in a diffraction pattern consisting of elongated spots, or streaks, visible in only one crystallographic direction at a time (as opposed to the whole 2D reciprocal space in LEED), as explained in Section 6.3.1. Because of this the substrate must be rotated to see other directions. Furthermore. the near parallel incidence of the electron beam allows for its use during growth. In this way, the surface structure can be identified, and the deposition of atomic monolayers can be observed (by recording RHEED intensity oscillations associated with the evolution of surface flatness during growth [2]) in real time. It is also possible to record RHEED movies of growth procedures; we will make use of such movies to characterise the QD formation process in Section 6.6.

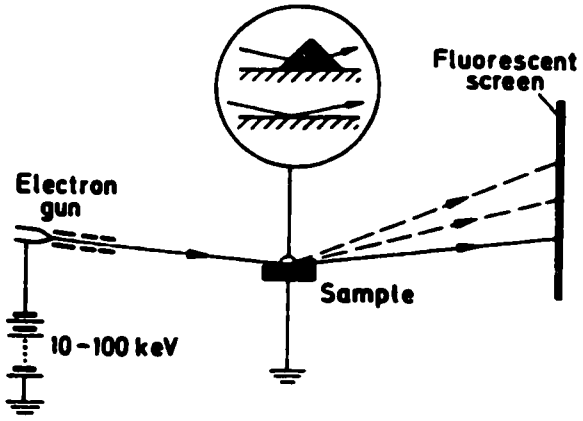

Figure 27. Schematic representation of Reflection High Energy Electron Diffraction. From ref. [91].

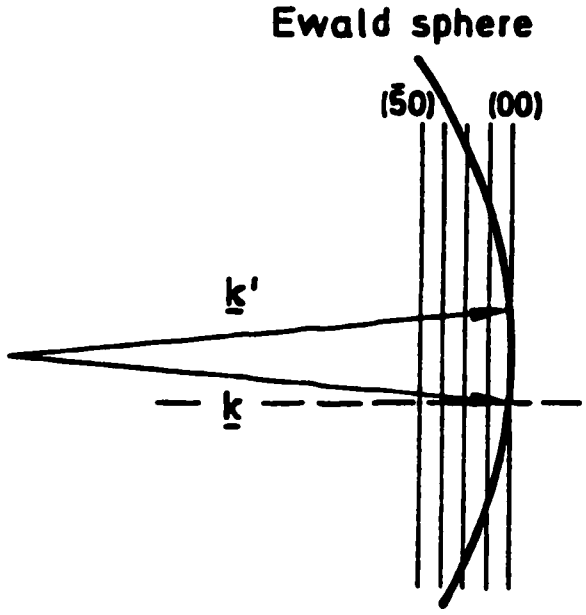

Figure 28. Representation in k-space of RHEED. From ref. [91].

6.3.1 2D Reciprocal Lattice

In this section we describe in detail the relation between LEED and RHEED patterns and the surface lattice. We begin by stating conservation of energy for in-coming (unprimed) to out-going (primed) wavevectors: $k^2 = k'^2$. We can separate the components parallel and perpendicular to the surface: $k_{//}^2 + k_{\perp}^2 = k'^2_{//} + k'^2_{\perp}$. We can also consider conservation of momentum independently in each of these directions: $\vec{k}'_{//} = \vec{k}_{//} + \vec{g}_{hk}$ (where $\vec{g}_{hk} = h\vec{a}_1^{\,*} + k\vec{a}_2^{\,*}$, and $\vec{a}_1^{\,*}$ and $\vec{a}_2^{\,*}$ are the reciprocal surface lattice unit vectors), but $\vec{k}_{\perp}$ is not conserved. The diffraction pattern produced is related to the reciprocal surface lattice which can be calculated from:

$$\begin{aligned} \vec{a}_1^{\,*} &= 2\pi \frac{\vec{a}_2 \times \vec{n}}{A} \\ \vec{a}_2^{\,*} &= 2\pi \frac{\vec{n} \times \vec{a}_1}{A} \\ A &= \vec{a}_1 \cdot \vec{a}_2 \times \vec{n} \end{aligned} \qquad (29)$$

where $\vec{n}$ is the unit normal to the surface, $(\vec{a}_1, \vec{a}_2)$ are the real space lattice unit vectors, and $(\vec{a}_1^{\,*}, \vec{a}_2^{\,*})$ are the reciprocal lattice unit vectors; both sets of lattice vectors are illustrated in Figures 33 and 36. The pattern produced by a given surface will have symmetry that is lower than or equal to that of its real space surface lattice. For normal incidence of the electron beam (as is commonly done in LEED), the point group of the diffraction pattern will be the one of the surface structure (the diffraction pattern is therefore literally the Fourier transform of the real space surface lattice). Off normal incidence of the electron beam will reduce the symmetry of the diffraction pattern. Because of this, in RHEED, the diffraction pattern consists of elongated spots visible in each crystallographic direction according to the direction of incidence of the electron beam.

6.3.2 LEED and RHEED Instruments

The LEED instrument that was used in our measurements is a Specs/Leybold Spaleed, which stands for spot profile analysis LEED [93], and this is synonymous to high resolution LEED. Its electron gun provides an electron beam of monoenergetic electrons (10's to few 10^2 eV) with a diameter at the surface of the order of 1mm. A system of electrostatic lenses provides the focussing. In high resolution mode, a system of deflection plates guides the electron beam to the surface and back to a channeltron (an electron "multiplier" operating on a cascade process).

The RHEED instrument consists of a Staib Electron Gun and Control unit model EK-35-R, and the KSA 400 control and data acquisition software provided by K-Space Associates. The digital camera acquiring the images from the RHEED phosphor screen is an Adimec MX12P charge coupled device (CCD).

6.4 Transfer Procedure Using an Amorphous Arsenic Cap

The LEED measurements were performed at the Physics Department of the University of Ottawa a few kilometres from IMS/NRCC where they were produced. To minimise surface contamination and oxidation, the samples were covered, or capped, with a layer of amorphous arsenic. This was done by cooling the substrate to $T \lesssim 80C°$ and exposing it to the arsenic flux in the growth chamber (described in the following chapter). After ~ 40 minutes the substrate had slowly

continued to cool down to T≈40C°, and a faint RHEED signal from the surface remained. Another 40 minutes exposure to the arsenic flux produced a total amorphous arsenic layer a few hundred angstroms thick and the total loss of the RHEED signal. After transport, the sample was mounted into the LEED vacuum chamber, and the amorphous arsenic cap was removed by thermal evaporation (see thermal desorption spectroscopy, Section 5.2). During a 1 °C/s temperature ramp, the rate of evaporation of arsenic becomes non-negligible above 300C° (see Figure 29).

After this evaporation, it is important to verify that the surface has returned to stoichiometry. This can be done by monitoring the ratio of two Auger peaks, one associated with arsenic and one associated with gallium. Figure 30 shows the relative amount of arsenic remaining on the surface after each temperature ramp in a sequence leading to the evaporation of the protective amorphous layer. Trace amounts of residual cap-arsenic have been observed by scanning electron microscopy even after 10 minutes at 420 °C [94]. As will be seen in the following section, LEED reveals surface reconstructions well before all traces of the arsenic cap are evaporated.

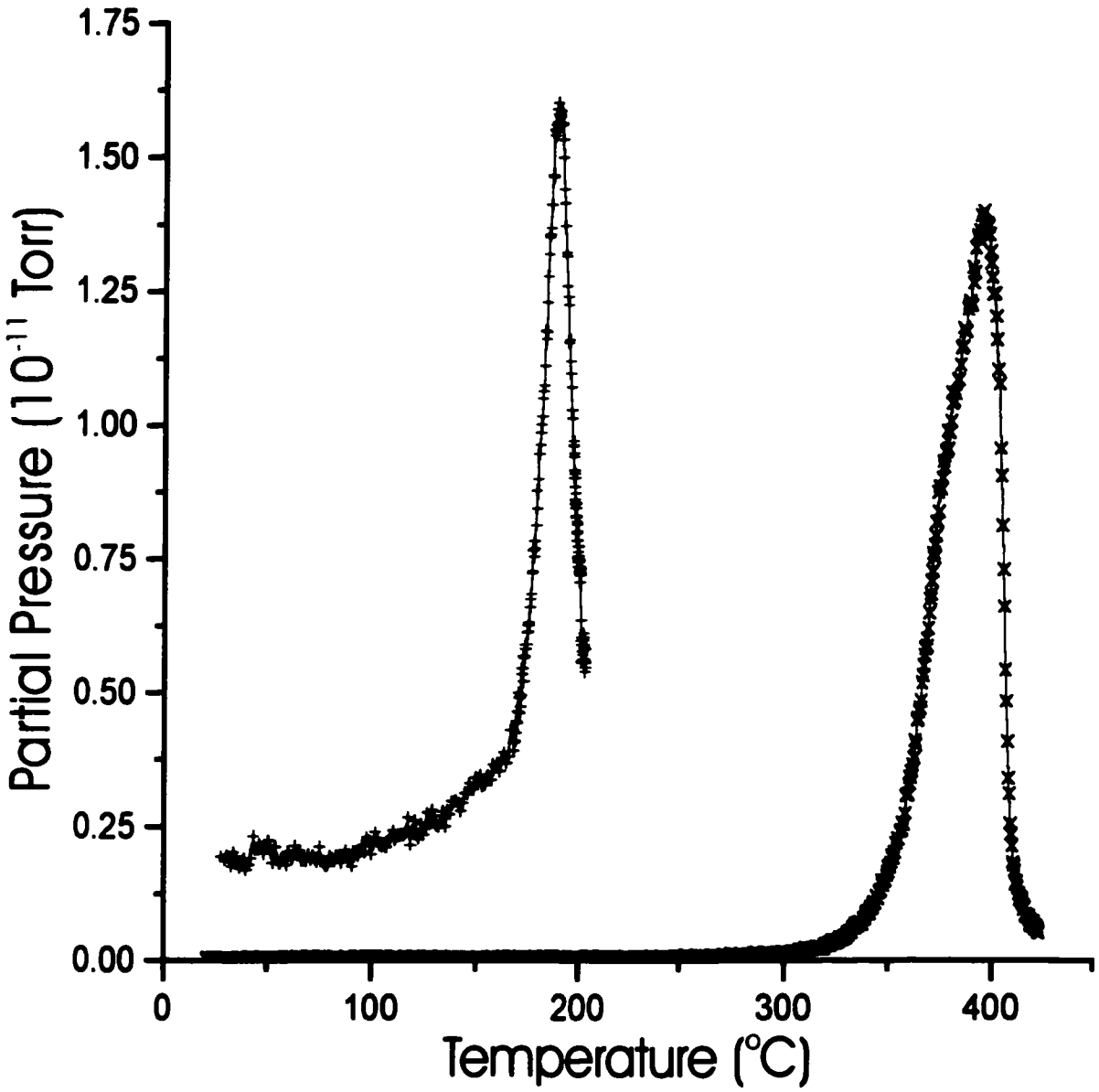

Figure 29. An example of an evaporation curve for the amorphous arsenic cap (x-crosses) and argon imbedded during sputtering by argon ion bombardment (+ plus) (not discussed, but referred to in Figure 30).

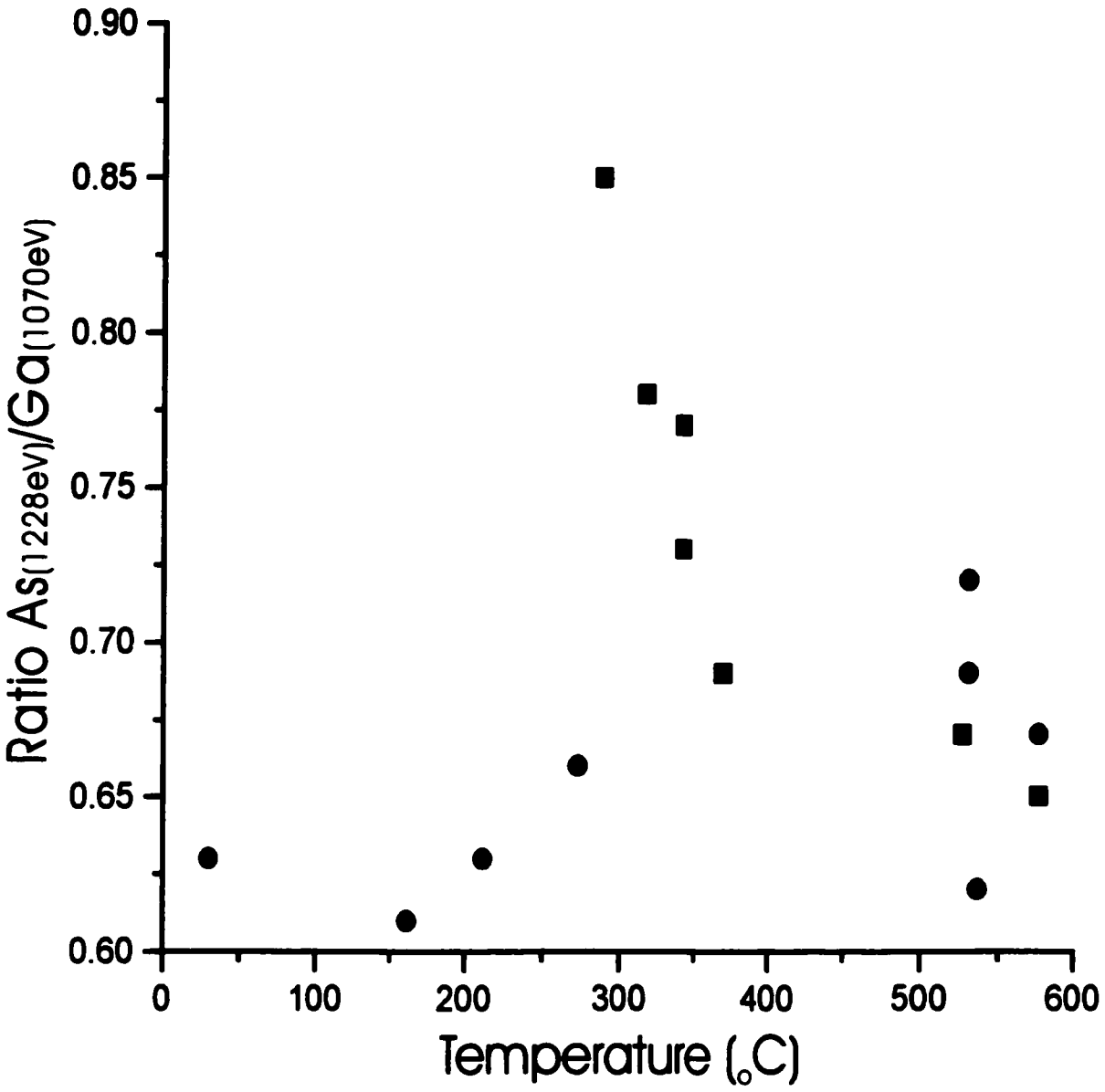

Figure 30: Ratio of the main auger electron signals for arsenic and gallium, during the evaporation of an amorphous arsenic cap (squares), and following sputtering by argon ion bombardment (circles). Each point was obtained by heating the sample at 1 °C/sec, stopping the ramp at the desired temperature and cooling back to T < 400K. The change in ratio as a function of temperature is proportional to the ratio of arsenic to gallium surface populations, but the absolute value is not calibrated to specific coverages. The trend in the ratio (squares) follows the arsenic evaporation curve in Figure 29, and the rough baseline described by the circles is indicative of the surface stoichiometry in the (2×4) surface reconstruction (described in Section 6.5.2).

6.5 GaAs Surface Reconstructions

Figure 31 is a phase diagram of the reconstructions of the GaAs(001) surface, and Figure32 is an STM image of the (2×4) surface reconstruction, both taken from the literature. As can be seen in Figure 32, the arsenic atoms dimerise along the $[\bar{1}10]$ leading to the two-fold periodicity in this direction, and two out of four dimers are missing along the $[110]$ direction leading to the four-fold periodicity in this direction.

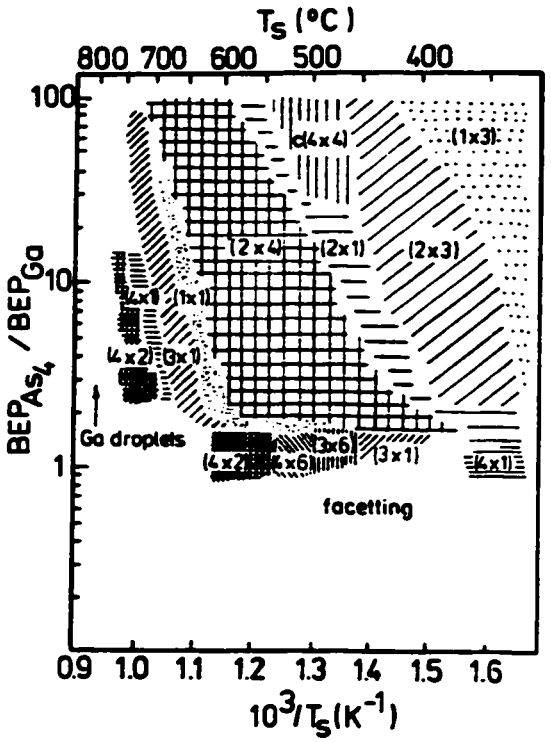

Figure 31. GaAs (001) surface reconstruction phase diagram. From ref. [95].

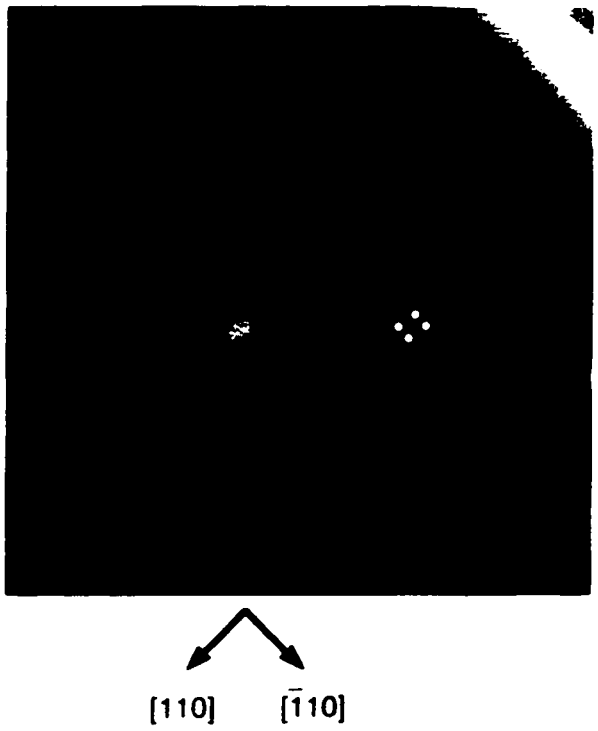

Figure 32. STM image of the (2×4) surface reconstruction. The overlaid schematic represents the surface unit cell and the arsenic dimers. From ref. [96].

In this section, the different reconstructions are presented in the order of their appearance as a function of increasing temperature. The LEED measurements were performed in vacuum (without an arsenic overpressure). The RHEED measurements were performed in low arsenic pressure.

6.5.1 Centred (4×4)

The centred (4×4) or c(4×4) reconstruction is an arsenic rich reconstruction that occurs, as can be seen in Figure 31, at high arsenic pressures and low substrate temperatures. This is an important point to which we shall refer when comparing our results to the literature in the final chapter of this thesis.

In the MBE reactor under arsenic flux using RHEED we observed the c(4×4) at $T \leq 400\,^{\circ}C$, as shown in Figure 33. In this figure, arrows are shown representing the RHEED electron beam directions of incidence onto a schematic representation of the real space surface, along with the diffraction patterns produced in each direction. In an actual experiment, there is a single electron beam, and the sample must be rotated to produce the diffraction patterns on a phosphor screen in line with the RHEED electron gun and the sample.

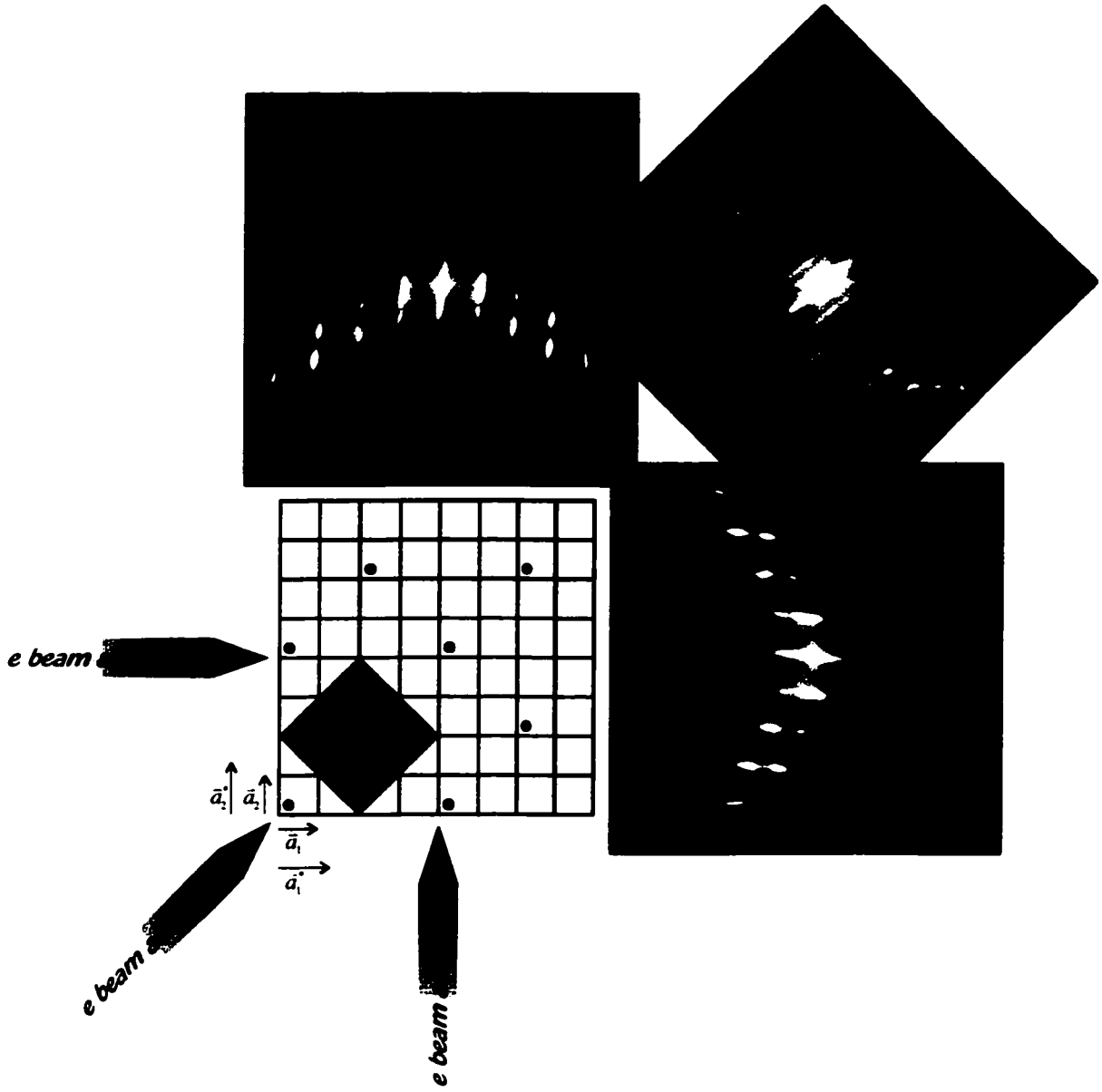

Figure 33. RHEED patterns for the c(4×4) GaAs (001) surface reconstruction. The electron beams are shown incident on a schematic representation of the surface structure (with the primitive surface unit cell shown as a shaded box). The RHEED patterns are placed around the schematic opposite their respective electron beam direction. The streaks are labelled at the bottom of each RHEED pattern.

Because the c(4×4) is a centred reconstruction, the two major surface directions $[\bar{1}10]$ and $[110]$ both display 2-fold periodicity. The specular spot, in all directions is labelled (0,0), the spot to the right and to the left that are one surface reciprocal-lattice unit vector away from the (0,0) are

respectively labelled (-1,0) and (1,0) in the $[\bar{1}10]$ (when the beam is incident along the $[110]$ direction), or (0,-1) and (0,1) in the $[110]$. A spot (or streak) situated half way between two spots separated by a reciprocal-lattice unit vector is called a half order spot (or streak) and is associated, in real-space to a feature on the surface repeating every two unit cells; such a spot between the (0,0) and (0,1) is labelled (0,1/2). Similarly, in the diffraction patterns of this 4-fold surface reconstruction, there are quarter order streaks. To see the 4-fold periodicity in RHEED, the substrate must be rotated 45° so that the electron beam is incident along the diagonal $[010]$ (intermediate to $[\bar{1}10]$ and $[110]$). The periodicity in this direction is $\sqrt{2}$ longer than along the $[\bar{1}10]$ or $[110]$.

In a LEED pattern of the same surface reconstruction all directions of the diffraction pattern are visible without having to rotate the sample. Because it requires a high arsenic coverage, this reconstruction is difficult to prepare under vacuum (as in our LEED measurements performed without an arsenic atmosphere). With the last traces of the amorphous arsenic cap providing the required surface population of arsenic, it was possible, after flash-annealing to T~430°C and cooling to room temperature, to see a very faint, poorly ordered c(4×4). This is shown in Figure 34; the diffraction spots which are visible are identified in Figure 35. The 4-fold reconstruction is seen in the form of very faint (±1/4,±1/4) around the (0,0) and similar structures around the (±1,±1) spots. Note that the 1/2 order spots are broad; this indicates that in this surface preparation the reconstruction is ordered only over very small distances on the surface.

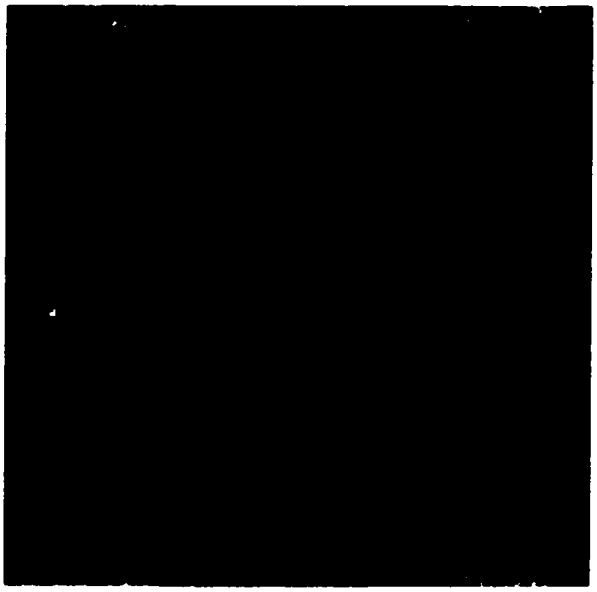

Figure 34. Map of the logarithm of LEED intensity for the GaAs (001) c(4×4) reconstruction. The colour scale was adjusted to facilitate the identification of the diffraction spots. Because of the surface symmetry, the $[110]$ direction (vertical) and the $[\bar{1}10]$ direction (horizontal) display the same periodicity.

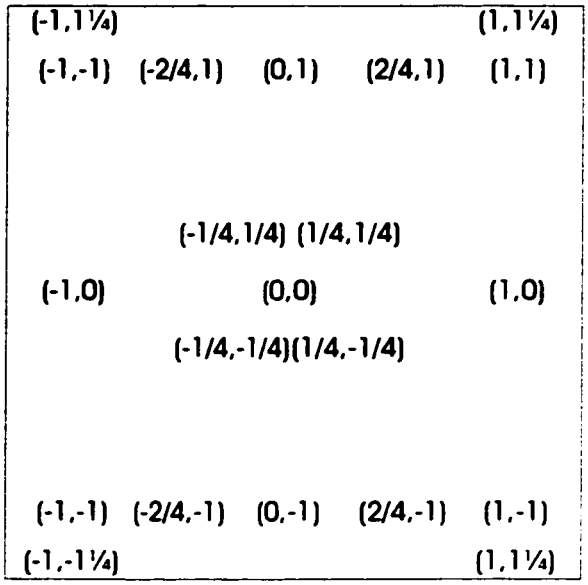

Figure 35. Schematic identifying the LEED spots in Figure34.

6.5.2 (2×4)

The (2×4) reconstruction, as can be seen in Figure 31, is observed at lower arsenic pressures and higher temperatures than the c(4×4). In the MBE reactor, we observed with RHEED the (2×4) at temperatures as low as ≈500°C; pictures of RHEED patterns recorded at this temperature can be seen in Figure 36. Here again, in this figure arrows representing the RHEED electron beams are shown incident onto a schematic representation of the real space surface, along with the diffraction patterns produced in each direction. The $[\bar{1}10]$ direction (i.e. with the electron beam in the $[110]$

azimuth) displays 2-fold periodicity, and the $[110]$ direction (i.e. with the electron beam in the $[\bar{1}10]$ azimuth) displays 4-fold periodicity. Note that in the $[110]$ direction, the middle quarter order spots, the $(0,\pm\frac{1}{2})$ and $(0,\pm1\frac{1}{2})$ have a low intensity.

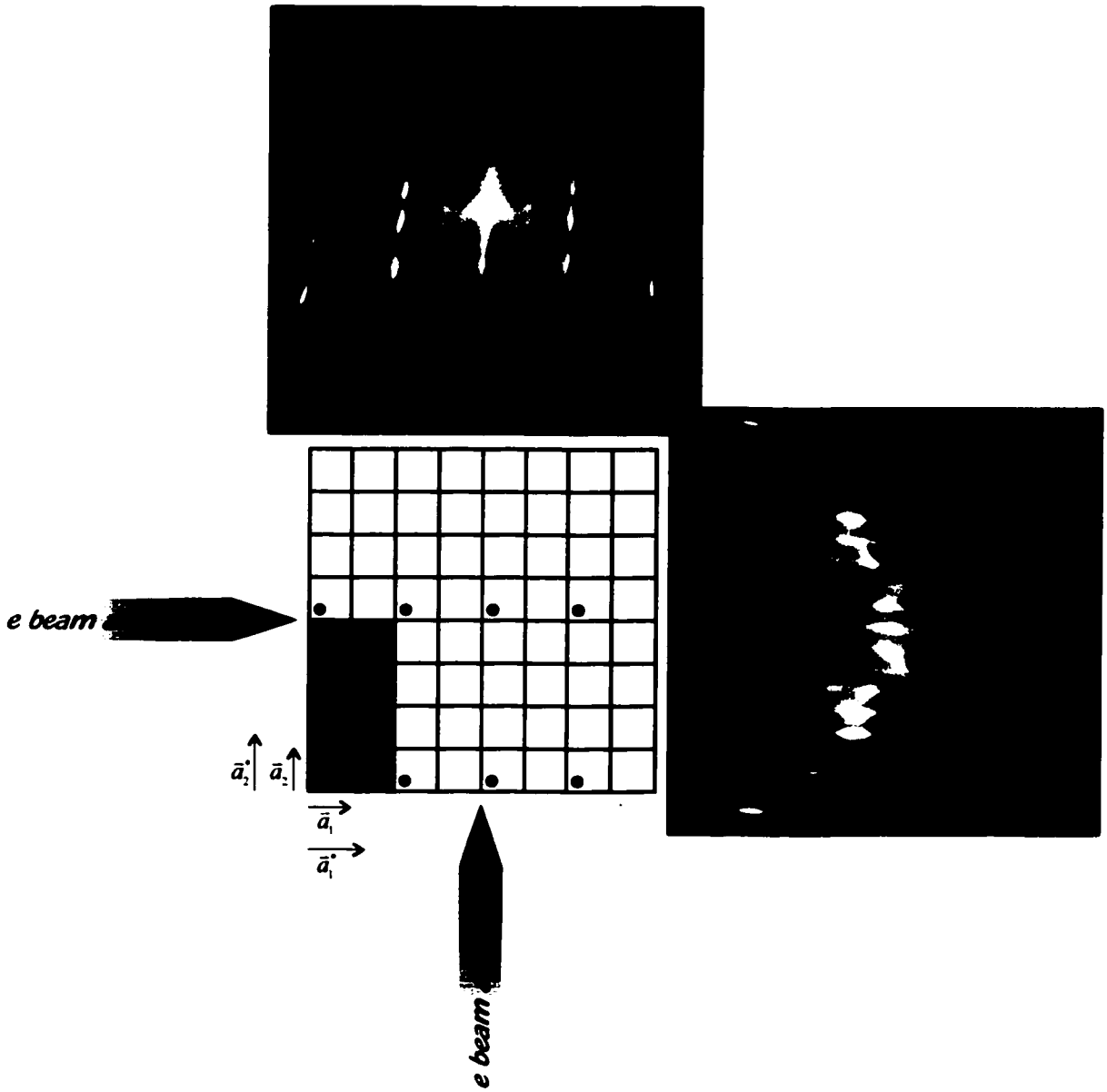

Figure 36. RHEED patterns for the (2×4) GaAs (001) surface reconstruction. The electron beams are shown incident on a schematic representation of the surface structure (with the primitive surface unit cell shown as a shaded box). The RHEED patterns are placed around the schematic opposite their respective electron beam direction. The streaks are labelled at the bottom of each RHEED pattern.

Figure 37 is a LEED pattern recorded after flash-annealing to T≈500°C and cooling to room temperature that displays a (2×4) reconstruction. The spots visible in this LEED pattern are identified in Figure 38. Almost all spots of the (2×4) reconstruction are visible. The half order spots in the $[\bar{1}10]$ direction, the (±½,0) are asymmetrical and greatly broadened.

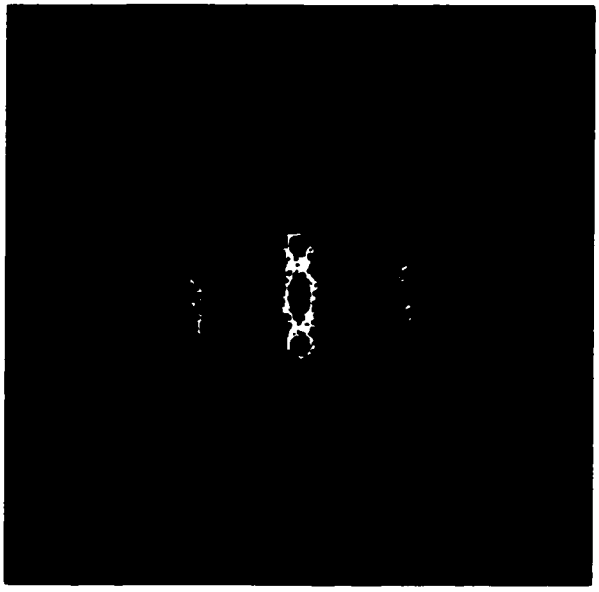

Figure 37. Log map of the LEED intensity for the GaAs (001) (2×4) reconstruction. The colour scale was adjusted to facilitate the identification of the diffraction spots. Because of the surface symmetry, the $[110]$ direction (vertical) and the $[\bar{1}10]$ (horizontal) direction do not display the same periodicity.

(-1,1¼)		(0,1¼)		(1,1¼)
(-1,1)	(-½,1)	(0,1)	(½,1)	(1,1)
(-1,3/4)		(0,3/4)		(1,3/4)
(-1,2/4)		(0,2/4)		(1,2/4)
(-1,1/4)		(0,1/4)		(1,1/4)
(-1,0)	(-½,0)	(0,0)	(½,0)	(1,0)
(-1,-1/4)		(0,-1/4)		(1,-1/4)
(-1,-2/4)		(0,-2/4)		(1,-2/4)
(-1,-3/4)		(0,-3/4)		(1,-3/4)
(-1,-1)	(-½,-1)	(0,-1)	(½,-1)	(1,-1)
(-1,-1¼)		(0,-1¼)		(1,-1¼)

Figure 38. Schematic identifying the LEED spots in Figure 37.

The two following sets of RHEED patterns were obtained at T≈560°C (Figures 39, 40) and T≈570°C (Figure 41 and 42) respectively. At these temperatures, the surface still displays a (2×4) reconstruction, but the relative intensity of the quarter order spots differ greatly from one another and

from the set in Figure 36. In Figure 40, all quarter order spots are visible and have similar intensity. In Figure 42 the central quarter order spot is very faint similarly to Figure 36, but the overall intensity distribution in these two figures differ greatly. In the literature [97], there are reports suggesting that this may be due to a different surface reconstructions having the same periodicity or to differences in the length scale of the ordering on the surface.

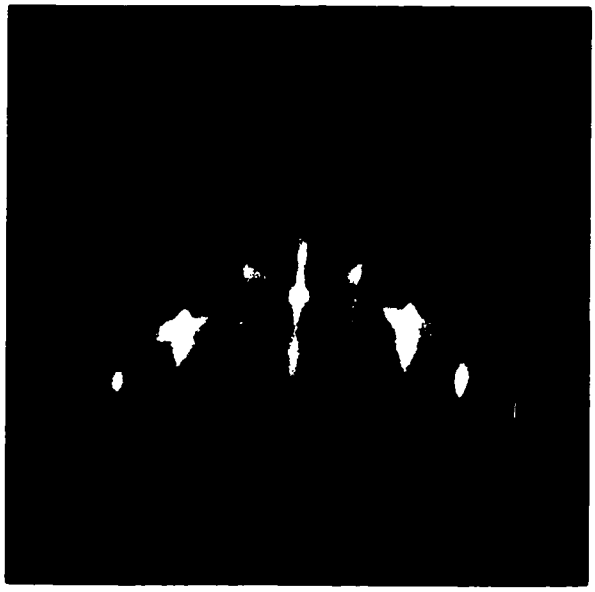

Figure 39. (2×4) GaAs (001) surface reconstruction, RHEED pattern of the $[\bar{1}10]$ (i.e. e-beam along the $[110]$). Compare to Figure 36.

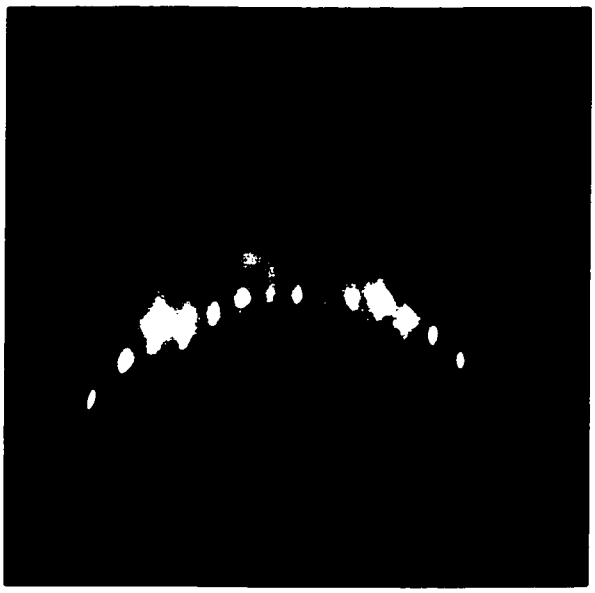

Figure 40. (2×4) GaAs (001) surface reconstruction, RHEED pattern of the $[110]$ (i.e. e-beam along the $[\bar{1}10]$). Compare to Figure 36.

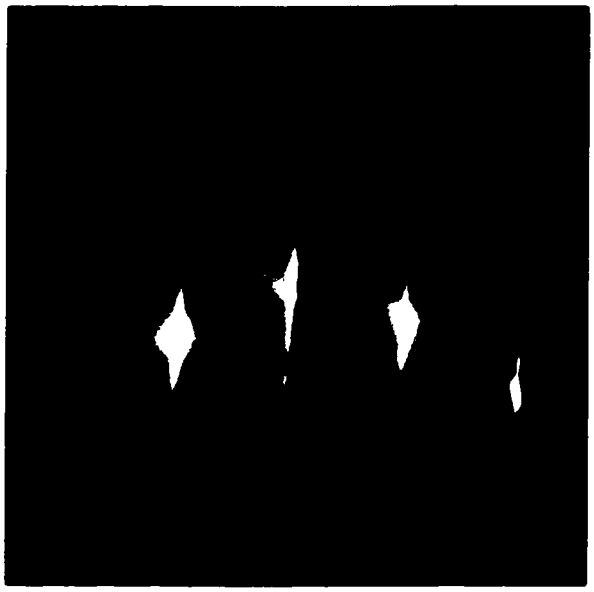

Figure 41. (2×4) GaAs (001) surface reconstruction, RHEED pattern of the $[\bar{1}10]$ (i.e. e-beam along the $[110]$). Compare to Figure 36.

Figure 42. (2×4) GaAs (001) surface reconstruction, RHEED pattern of the $[110]$ (i.e. e-beam along the $[\bar{1}10]$). Compare to Figure 36.

6.5.3 Unreconstructed, Intermediate Phase Going from (2×4) to (4×2)

Figures 43 and 44 are pictures of RHEED patterns recorded at T≈610°C As pointed out earlier, only the first order diffraction spots are visible in both directions, that is the (-1,0), (0,0) and the (1,0), and the (0,-1), (0,0) and (0,1). This indicates that the surface is unreconstructed, or in other words, that the surface termination presents the same periodicity as the bulk structure.

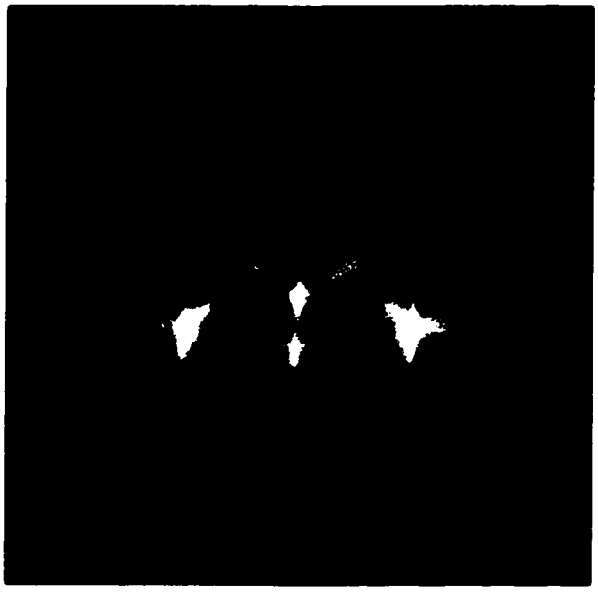

Figure 43. (1×1) GaAs (001) surface reconstruction, RHEED pattern of the $[\bar{1}10]$ (i.e. e-beam along the $[110]$). Compare to Figure 36.

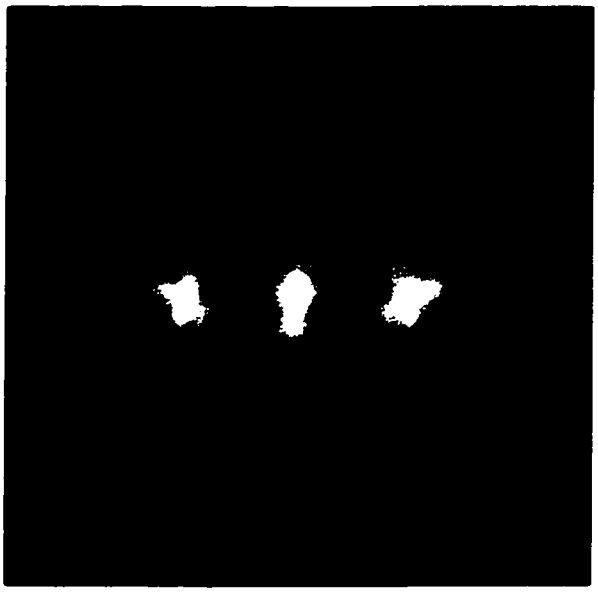

Figure 44. (1×1) GaAs (001) surface reconstruction, RHEED pattern of the $[110]$ (i.e. e-beam along the $[\bar{1}10]$). Compare to Figure 36.

The (4×2) surface reconstruction is a gallium rich surface structure occurring at higher temperatures (Figure 31). Its surface reconstruction has the same periodicity as the arsenic-terminated (2×4), but the alignment of the unit cell is rotated by 90°. We show no pictures of RHEED patterns recorded of this reconstruction[19], but the general appearance of the pattern would be similar to the sets of RHEED patterns discussed in the previous section but with the $[\bar{1}10]$ and $[110]$ directions interchanged. The qualitative difference in the RHEED patterns of the (2×4) and (4×2), outside of the interchanged periodicity along the two main crystallographic directions, is that the streakiness of the RHEED spots is more pronounced for the (4×2). In fact, Figures 41 and 42 were recorded after going briefly into the unreconstructed phase (approaching the (4×2)) and back; the

[19] Growing on GaAs exhibiting the (4×2) reconstruction would within seconds lead to the formation of metallic gallium precipitates on the surface. This would irreversibly damage the surface morphology and would render the substrate unusable in a growth procedure.

streaks are sharper (i.e. comparing the width of the streaks in Figures 39 and 41) because the reconstruction is better annealed after going to the higher temperature. For the same reason, the (4×2) displays similarly sharp streaks.

6.6 Real-time RHEED Monitoring of the Deposition of InAs on GaAs (001)

Figures 45 (a) to (f) display image frames taken from a RHEED movie of InAs deposition on GaAs (001) at T = 500 °C and $P_{As4} = 5.0P_0$ with the electron beam in the $[\bar{1}10]$ azimuth. The time and coverage at which each frame was recorded is indicated in the respective caption. All such RHEED movies were recorded using a 5 mm square sample indium mounted onto a two inch silicon wafer. This was done in order to minimise in the sampling area of the RHEED electron beam the effects of thermal gradients and flux gradients (as those described in Chapter 7 in the production of the InAs coverage graded samples).

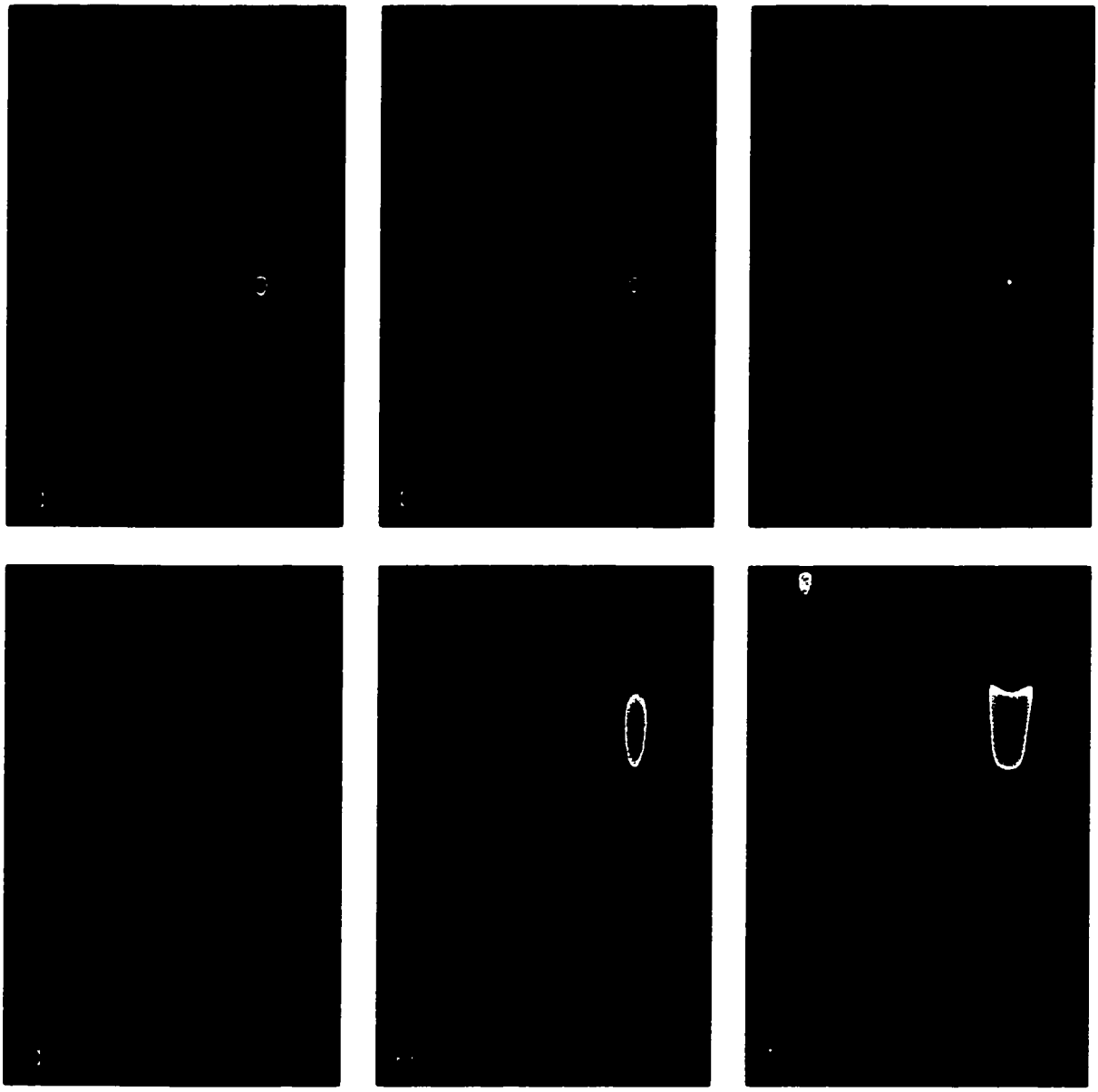

Figure 45. Frames from a RHEED movie of the deposition of InAs on GaAs: (a) 0 sec, 0 ML; (b) 1 sec, 0.08 ML; (c) $t_{(QDs)}$ - 0.5 sec, 1.86 ML, (d) $t_{(QDs)}$ + 0.5 sec, 1.94 ML, (e) $t_{(QDs)}$ + 2.0 sec, 2.06ML, and (f) $t_{(QDs)}$ + 4.0 sec, 2.21 ML.

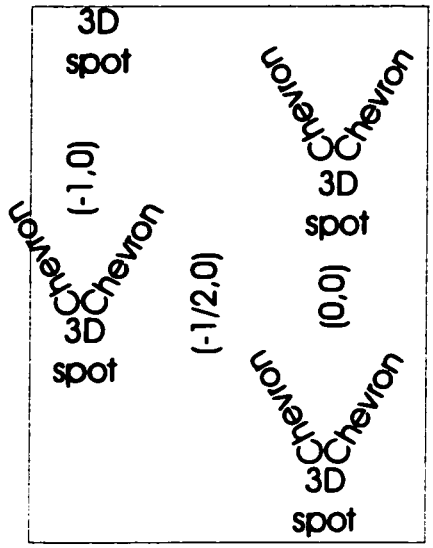

Figure 46. Schematic identifying the RHEED spots in Figure 45.

All the spots visible in each image of Figure 45 are identified in Figure 46. In Figure 45 (a), the InAs deposition is initiated as the GaAs surface displays the c(4×4) reconstruction; this figure, like Figure 33 displays only the half order spot, the (0,-½) in the $[1\,1\,0]$ direction of the c(4×4) reconstruction. In Figure 45 (b), early on in the deposition, the GaAs surface becomes unreconstructed (perhaps showing faint signs of the c(4×4)) at InAs coverages less than a tenth of a monolayer. Because of the layer by layer growth mode, at coverages nearing one monolayer, the GaAs can be considered to be completely covered by strained InAs. As shown in Figure 45 (c), at $\theta = 1.86$ ML the InAs surface remains unreconstructed throughout most of the deposition process as shown by the absence of any spot other than the (0,0) and the (-1,0). Also in the same figure, it can be seen that the intensity of the specular (0,0) spot is reduced. In Figure 45 (d), $\theta = 1.94$ ML the surface is still unreconstructed, and just above the specular spot a broad streak of low intensity starts to form. The appearance of this streak coincides with the onset of 3D growth, and is actually a "3D" diffraction spot due to transmission of the electron beam through the nucleating Stranski-Krastanov

islands, the QDs. In Figure 45 (e), at $\theta = 2.06$ ML chevrons begin to be visible on the 3D spot. As deposition proceeds and coverage continues to increase beyond the 2D to 3D critical coverage, the chevrons and the 3D spots continue to increase in intensity as can be seen in Figure 45 (f). These chevrons are indicative of faceting of the surface of at least a considerable fraction of the QDs in the ensemble [15].

Using RHEED movies such as the one described above, the (T, P) parameter space of InAs growth on GaAs(001) was mapped out for both As_2 and As_4 for a fixed InAs growth rate (0.02 nm/s). Figures 47 and 48 show plots of the variation in the time of transition from 2D layer by layer growth of the wetting layer to 3D growth of QDs; the same data is plotted as a function of substrate temperature in Figure 47 and arsenic pressure in Figure 48. The large error bars are primarily due to the difficulty in identifying the point of 2D to 3D transition (uncertainty of $\sim \pm 0.5$ sec); they also include a contribution due to the identification of the start of the InAs deposition (uncertainty of $\pm$ one movie frame spacing $\approx$ 0.1 sec). Over the ranges explored, the changes in pressure and temperature lead to variations in transition time of approximately 5% and 20% respectively. The variation due to pressure is almost entirely within the error bars, whereas the variation due to temperature is greater than the error bars. This will be further discussed in Chapter 9.

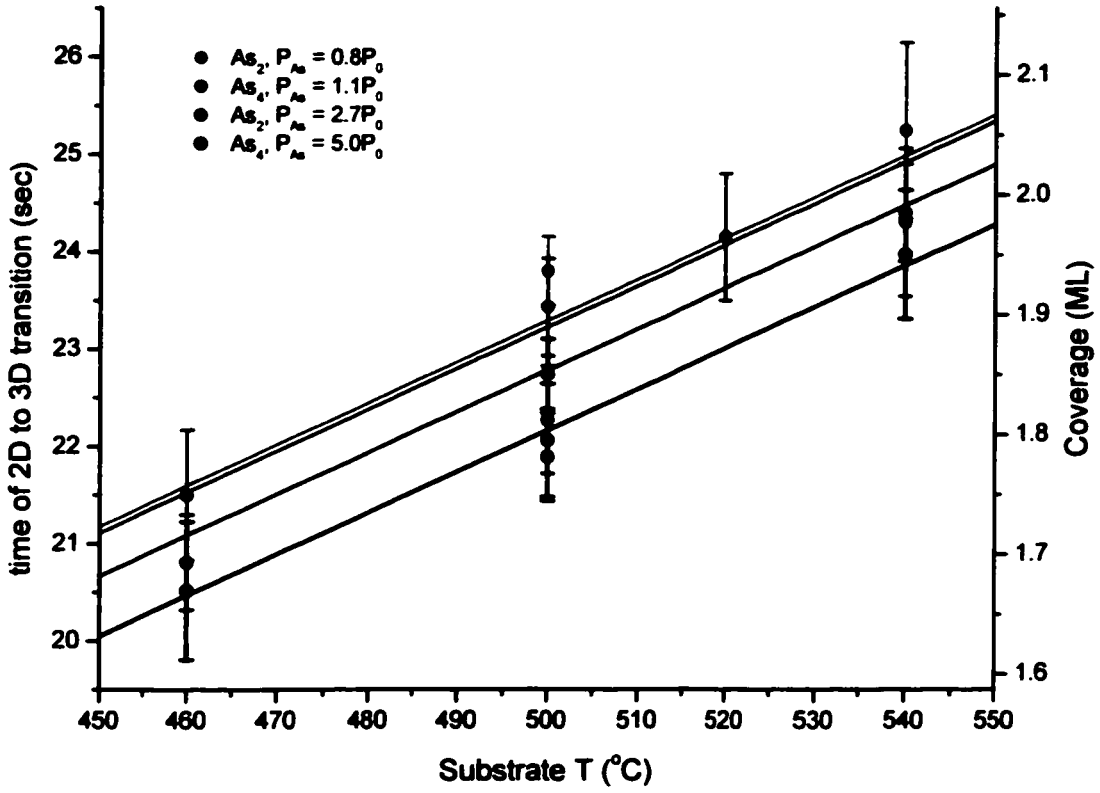

Figure 47. Dependence of the timing of the 2D to 3D transition on the substrate temperature used during the deposition of the InAs. A double linear regression, $t_{2D\text{-}3D} = (2.4 \pm 1.8)s + (0.042 \pm 0.004)s \cdot °C^{-1} \times T - (0.27 \pm 0.06)s \cdot P_0 \times P$, performed on the entire data set provides "lines to guide the eye."

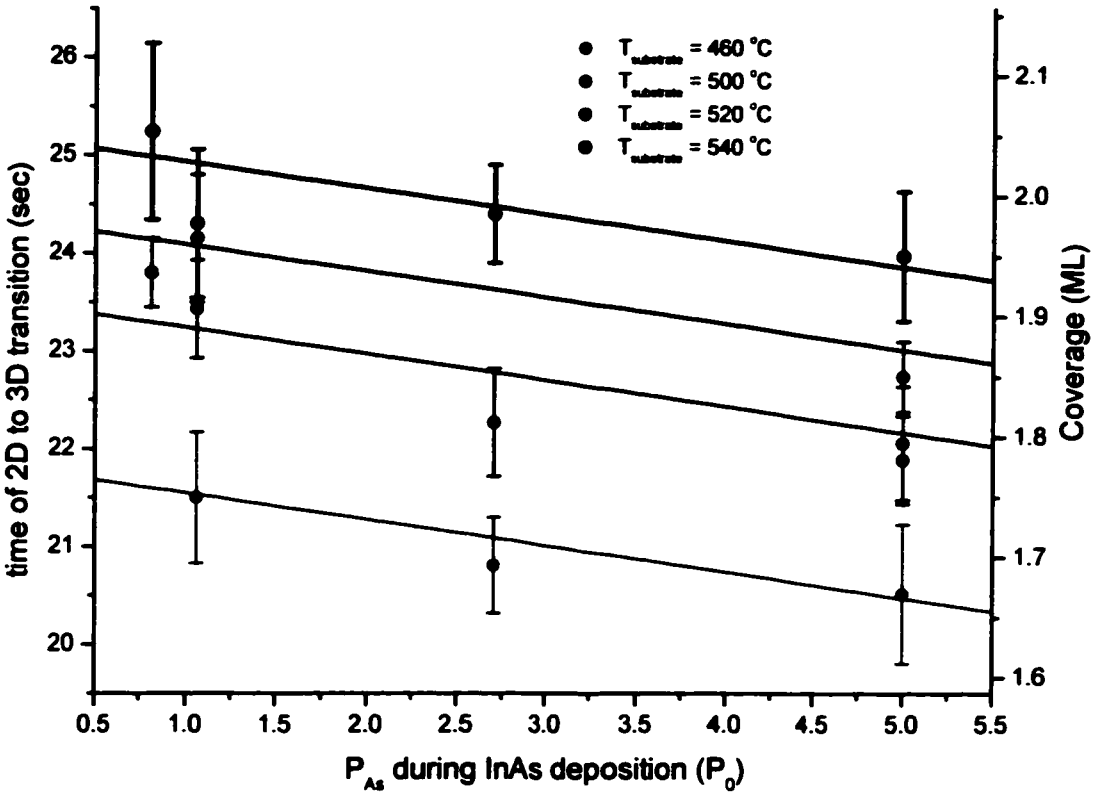

Figure 48. Dependence of the timing of the 2D to 3D transition on the arsenic pressure used during the deposition of the InAs. A double linear regression, $t_{2D\text{-}3D} = (2.4 \pm 1.8)s + (0.042 \pm 0.004)s \cdot °C^{-1} \times T - (0.27 \pm 0.06)s \cdot P_0 \times P$, performed on the entire data set provides "lines to guide the eye."

7 Arsenic Pressure Effect on the Dependence of Quantum Dots on InAs Coverage, Characterisation by PL

In this chapter we present the characterisation measurements of the set of three samples having an InAs coverage gradient across the substrate. We also introduce the characterisation technique that was used in the study of this set of samples, photoluminescence (PL) spectroscopy. Based on these measurements, we shall discuss in Chapter 9 the InAs coverage dependence of the properties of quantum dot (QD) ensembles formed at three arsenic pressures.

7.1 Description of Three InAs Coverage Graded Samples

The three InAs coverage graded samples (Series #1) presented in this chapter were grown following the structure depicted on the left hand side of Figure 21. As explained in Section 5.3, a 500.0 nm GaAs buffer was deposited at 0.2 nm/s and a temperature of ~600 °C. Following this, 1.9 monolayers (ML) of InAs were deposited at 0.02 nm/s at ~515 °C; as shown in Section 4.1.1 this amount of InAs is nearly equal but slightly greater than the critical coverage necessary to form QDs. The samples were then annealed *in situ* during a 60 sec growth interruption at the same temperature. As discussed in Sections 4.1.2 and 4.1.3 this InAs deposition temperature and anneal time allow the QD ensemble to evolve sufficiently to display a a well resolved excited state structure in PL. Subsequently the samples were indium-flushed using a 5.0 nm partial cap of GaAs and a temperature ramp up to ~600 °C. Following this, 95 nm of GaAs were deposited at this temperature, thereby

completing the cap. As discussed in Section 4.1.4, an indium flush is a controlled discontinuous capping procedure that reduces the QDs in height [38].

For each sample a different As_2 pressure was used throughout the deposition and anneal of the InAs, as well as during the indium flush. The rotation of the sample was paused during the InAs deposition yielding an indium flux gradient across each sample. This gradient is due to the spatial anisotropy in the indium flux due to the angular distribution of the evaporation from the effusion cell and the angle of the effusion cell with respect to the wafer [88]. Each graded sample thus provides a virtual set of samples with different InAs coverages. For the lower As_2 pressure sample, the As_2 pressure was returned to the nominal value for GaAs growth during the later stages of the indium evaporation after the effects of the indium flush on the QDs are completed.

The trends that will be observed with this set of samples are due to the InAs coverage variation when comparing different areas on each sample, and to the difference in arsenic pressure when comparing one sample to another.

7.2 Photoluminescence

PL is the most frequently used characterisation technique in the study of QD samples. This is because the main applications of such samples are foreseen to involve the production or detection of light. We will therefore discuss this technique in considerable detail.

With the assistance of the author, the PL measurements were performed by Karin Hinzer[20] at IMS/NRCC. The analysis of the spectra was carried out by the author.

7.2.1 Technique

Following the perturbation caused by an impinging light beam (usually a laser), an electron that has been promoted to the conduction band can recombine with a hole state in the valence band. If enough recombination events occur in the active region of a sample, the sample produces detectable luminescence. Important information can be obtained by mapping this luminescence intensity as a function of energy (or wavelength). This can be done by collecting the light emitted by the layer and directing it to the entrance slit of a spectrometer. The light spectrum can then be dispersed by a grating and each wavelength subsequently focussed onto a detector.

Figure 49 (a) shows, on a band structure diagram, the series of events triggered by the absorption of a photon in a bulk structure, which the GaAs above and below the QDs in Figure 21 can be assumed to be. First, an electron is promoted to the conduction band at the instant of absorption. If the energy of the photon absorbed is higher than the bandgap, the electrons and holes are created with some excess kinetic energy, they will thermalise to the band edge by optical phonon emission and subsequently recombine radiatively to emit a photon of lower energy [see 98, and references therein]. The resultant spectrum will show an emission line at an energy roughly equal to the bandgap with a FWHM strongly dependent on temperature and excitation intensity because of the continuous dispersion relationship.

---

[20] Present address: Nortel Networks, Ottawa, Canada K1Y 4H7.

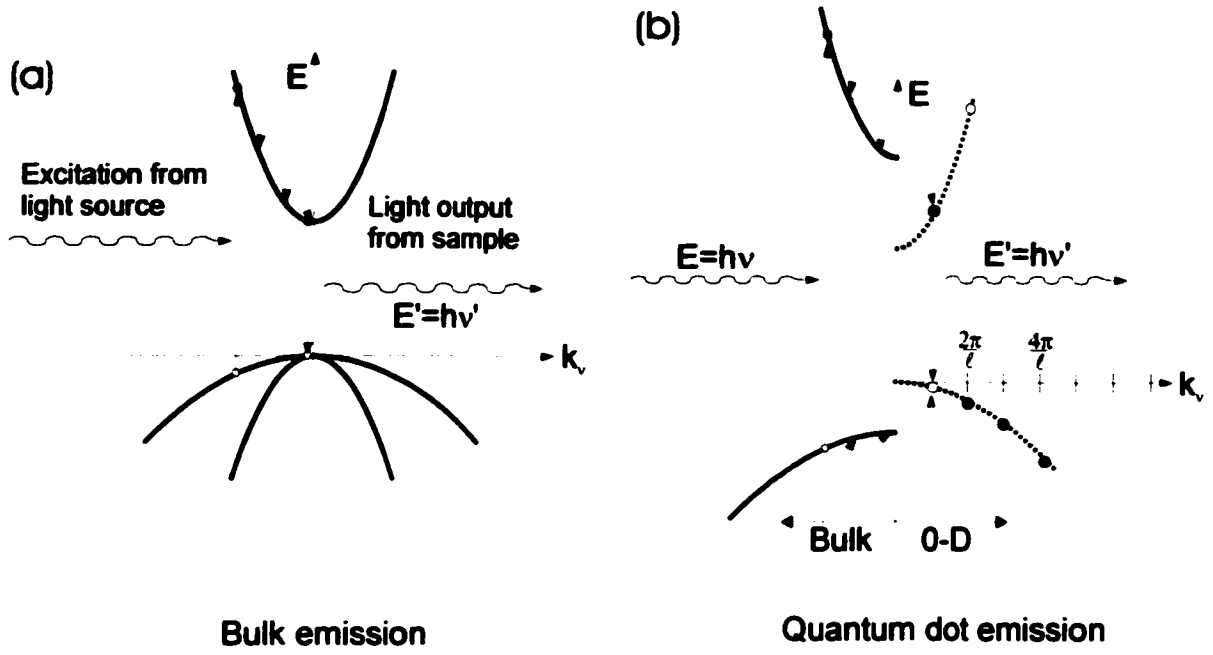

Figure 49. Bulk (a) and QD (b) sample response under the action of the excitation source.

Figure 49 (b) shows in k-space the course of events produced by non-resonant excitation in the type of QD samples represented in Figure 21. Non-resonant excitation is excitation at an energy above the confinement barrier and not at an energy equal to a level in the QD structure. The carriers are therefore created in the bulk barrier material. While the carriers thermalise to the band edge (in k-space), they diffuse closer to the QDs (in position-space). At this point they relax from the energy continuum of the bulk to the discrete states of the QD ensemble, such as those described by the QD model in Section 2.3. The combined intensity of excitonic recombinations occurring within each QD in the ensemble containing one or more electron-hole pair is then recorded by the PL setup described in the following section. Each QD in the ensemble contributes sharp lines to form an overall PL spectrum containing emission peaks that are broadened due to the composition and size inhomogeneity of the QD ensemble.

7.2.2 Experimental Setup

Figure 50 shows a schematic of a PL set-up. In the case of the PL measurements performed for this thesis, the wavelength selection was obtained by the use of a grating in the spectrometer stepwise rotated sending different wavelengths onto an exit slit positioned in front of the detector. The intensity of the narrow wavelength range selected by the slit is measured by the detector and recorded by a computer. The grating of the spectrometer is rotated through a range of positions until the desired spectrum is obtained. This type of PL experiment, in which the detector is not position sensitive[21], is called scanning spectrometer PL.

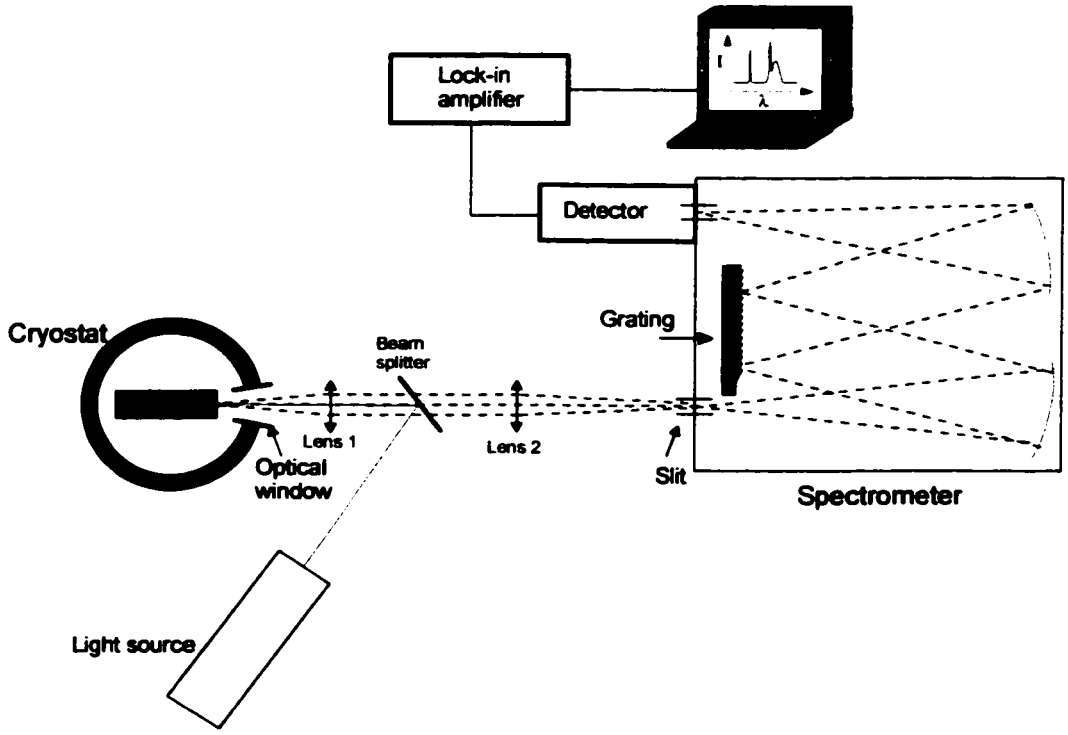

Figure 50. Experimental layout of a PL setup.

[21] A charge coupled device (CCD) which simultaneously detects a range of wavelengths, each pixel (position) on the CCD detecting a different wavelength, would be an example of a position sensitive detector.

The specific apparatus used in the characterisation of our samples consisted of a liquid nitrogen-cooled optical cryostat for measurements at T = 77 K. At this temperature, the thermal energy available to excite the carriers out of the QDs is approximately 7 meV, which is much smaller than the potential confining the carriers to the QD states[22] described in the QD model in Section 2.3. The 532 nm line of a Millennia V Nd:YVO_4 laser by Spectra-Physics was used as the excitation source. The light beam was modulated by a chopper, and focussed onto the sample surface to a 50 μm diameter circular spot. The spot size and shape were verified using an imaging CCD camera system. A CVI DK240 ¼-m double-grating monochromator equipped with a 600 grooves/mm grating dispersed the light onto a EO-817L North Coast Scientific nitrogen-cooled Ge photodetector, allowing for detection between 700-1800 nm. This spectrometer, with the above mentioned grating, has a dispersion of $\Delta\lambda$ = 3.2 nm per mm of displacement at the detection slit. The slits were usually opened to a width of 1 mm. The detected signal was amplified with a Stanford Research Systems SR810 DSP lock-in amplifier. The uncertainty of the detected signal can be determined by evaluating the intensity changes in the featureless regions of any given spectrum.

The main point to retain with regards to the characterisation of the samples in this study is this: PL is the process by which a material emits a photon after recombination of thermalised photo-created electron-hole pairs. The energy or wavelength of the emitted photons provides us with information on the energy levels in the source structure, in this case, QDs.

[22] The energy spacing between the s-level and the wetting layer in our samples varies approximately from 200 to 400 meV. The band offset distributes this value between the conduction and valence bands so that the potential confining the electrons, for instance, is approximately 140 to 210 meV.

7.2.3 How the Properties of Quantum Dot Ensembles Are Interpreted from PL Spectra

In explaining how the properties of QD ensembles can be deduced from PL spectra, this section relies on the subject matter covered in Chapter 2, for the general effects of QD size on energy levels, and in Section 4.1, for the experimental evidence linking specific features in PL spectra to real QD ensembles. Particularly, Section 4.1 is directly relevant because it is from this past work that the techniques for "reading" the PL spectra of QD ensembles were derived. At IMS/NRC, hundreds of QD samples have been produced by MBE and studied, leading to the following general observations:

From the relative intensity of the wetting layer (WL) emission to that of the QD emission, we get information on the QD density. This is because, as shown in Section 4.1.1, the greater the number of QDs, the lesser the probability that excitons will recombine in the WL. Barring lower probability non radiative recombinations (such as the Auger process and non-radiative recombinations occurring at defects), practically all recombinations occur in the WL and QDs because of the lower bandgap in these regions. Assuming a structure containing a great number of QDs, say approximately $100/\mu m^2$ or more, then essentially all carrier recombinations are observed to occur in the QDs and no intensity will be detected from the WL. At lower densities, the WL intensity will be measurable, and the WL intensity will increase relative to the intensity of the s-level of QDs a function of decreasing QD density.

From the position of the WL peak, we obtain a measure of the effective thickness of the WL. As shown in Figure 15 in Section 4.1, the WL thickness can be derived approximately from the layer-by-layer growth phase of the SK growth mode. With this, it is possible to get a rough estimate of the

thickness of the WL in a given InAs/GaAs sample. The use of the relationship described in Figure 15 assumes that the mechanisms, such as alloying of the deposited InAs with the surrounding GaAs, affect similarly the WLs of the samples being compared; this assumption is reasonable as long as the growth conditions were kept nominally alike. Although absolute values of WL thickness must be considered highly uncertain, it is at least possible to establish a trend of WL thickness evolution from one sample to another in a set of samples that were grown similarly.

From the position of the QD levels, particularly the s-level and the intersublevel spacing, we get information on the size of the QDs. As shown experimentally in Section 4.2, larger QDs emit at longer wavelengths. Because capped QDs have a low aspect ratio, the confinement of the carriers is dominated by the height of the QDs, so that it is the height of the QDs that primarily controls the position of the s-level; this is predicted by the QD model in Section 2.3. Furthermore, the width of the QDs controls primarily the inter-sublevel spacing; this is apparent in the QD model because of the 2D-harmonic oscillator term in equation 24. The lack of definitive information on capped QDs restricts the application of QD models such as the one presented in Section 2.3. As we have suggested in Chapter 4, and as we will discuss in Chapter 9, based on our results, the capping procedure, even in the case of continuous capping, significantly modifies the QDs structurally and/or compositionally. It is therefore very difficult to know accurately the composition and size of QDs from which PL spectra are obtained.

7.2.4 Measurements: PL of Quantum Dots as a Function of Coverage at Three Arsenic Pressures

The photoluminescence measurements for these graded samples are shown in Figure 51. Each box represents a sample produced at a different arsenic pressure, and each spectrum was measured at a different point along the InAs coverage gradient. In each box, InAs coverage increases from bottom to top. All spectra were normalized to the same maximum intensity and offset for clarity. The As_2 pressure at which the InAs was deposited and annealed for each sample is written in units of P_0 (as discussed in Section 5.3.4) in the upper left hand corner of each box. In Figure 51a the s-level position is almost independent of InAs coverage but the WL redshifts with increasing coverage. In Figure 51b both the s-level and WL positions show little dependence in InAs coverage. In Figure 51c the s-level PL position is strongly dependent in InAs coverage and the WL blueshifts with increasing coverage. The range indicated in Figure 51a around 1090 nm is the expected s-level position after an indium flush at 5.0 nm [59]. That the s-level emission falls outside of this range for the $1.0P_0$ sample shall be an important point in the discussion in Chapter 9.

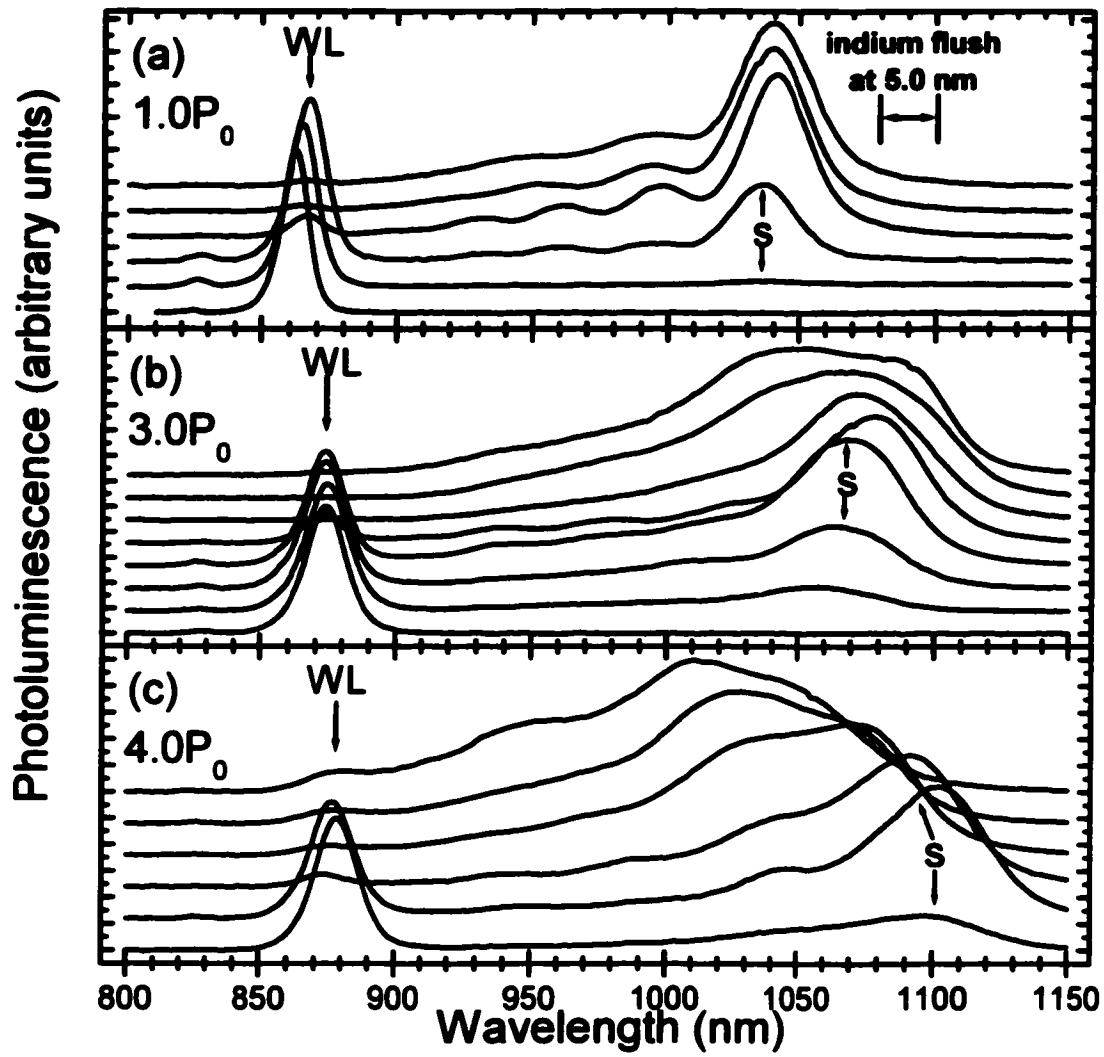

Figure 51. PL spectra for Series #1, three samples having a graded InAs coverage. The WL and s-level recombination peaks are indicated. The arsenic pressure used during the deposition and anneal of the InAs is indicated in each box. In (a) the expected position for the s-level emission is indicated (relevant to all three boxes/samples). From ref. [14].

For all three As_2 pressures shown in Figure 51, the WL luminescence is reduced relative to the s-level intensity as InAs coverage increases. This indicates that the QD density increases with increasing coverage [31]. Moreover, there are considerable differences in the WL peak position from one As_2 pressure to another. The redshift of the WL observed with increasing coverage at P_{As2} =

$1.0P_0$ (Figure. 51a), unlike the trends at the two higher As_2 pressures, is opposite to the results of a previous study (see Section 4.1.1) [31]. This redshift suggests that, at low As_2 pressures, the material deposited after the 2D to 3D transition tends to go into the WL, increasing its thickness. Although some material does go towards increasing the QD density, which is probably due to the dynamic nature of the WL [31], very little or no additional material appears to go towards increasing the size of the QDs. Such a stabilization of the QD properties at low As_2 pressures is beneficial for the reproducible tailoring of the QD energy levels.

The dependence of the QD emission lines on InAs coverage differs greatly depending on the arsenic pressure that was used during the deposition and anneal of the InAs. At $P_{As2} = 4.0P_0$ the QD emission structure blueshifts with increasing InAs coverage, at $P_{As2} = 3.0P_0$ it redshifts, and at low arsenic pressure, $P_{As2} = 1.0P_0$, there is some sort of stabilisation of the QD emission line position. Although these three samples were otherwise grown identically, the resulting PL peaks behave very differently as a function of InAs coverage when the As_2 pressure is changed.

It is important to note that all three samples were indium-flushed according to the same procedure, and yet the PL peaks of the QDs produced at $P_{As2} = 1.0P_0$ are blueshifted considerably more than those of the two higher pressure samples. The range indicated in the upper-right-hand corner of Figure 51(a) shows where, based on the study of the effects by Fafard and Wasilewski [38,59], the QD emission from the s-level should be for QD ensembles formed at coverages near the 2D to 3D critical coverage that have been indium-flushed with a 5.0 nm partial GaAs cap. The s-level of the $P_{As2} = 3.0P_0$ and $4.0P_0$ PL spectra recorded at the point of near critical coverage (sixth curve

from the bottom in Figure 51(b) and the fourth curve from the bottom in Figure 51(c)[23]), fall within this range. The s-level emission of the $P_{As2} = 1.0P_0$ sample, at all coverages falls at the same wavelength and is well outside of the expected range. The effect of the indium-flush is to reduce the height of the QDs, which is seen in PL by a blueshift of the QD emission with respect to similar non-indium-flushed QDs. The dependence of the effect of the indium flush on QD size, which is suggested by the observation that the effect of the indium flush is more pronounced in the case of the $P_{As2} = 1.0P_0$ sample, shall be of importance in our discussion of capping effects in Chapter 9.

[23] These curves are selected based on the fact that in the case of each sample these are the lowest InAs coverage curves that do not display a (considerable) WL emission. As will be seen in Chapter 8, samples produced at a coverage similar to those used for the samples in Chapter 8, which is similar to the InAs coverage used in the indium-flush studies of Fafard and Wasilewski, do not display a WL emission.

8 Arsenic Pressure Effect on Quantum Dots at a Single InAs Coverage, Characterisation by SEM, AFM and PL.

In this chapter we present the characterisation measurements of the set of nine samples having uniform InAs coverages that were deposited at different arsenic pressures. These samples have two layers of quantum dots (QDs), one buried in GaAs and one on the open surface of the samples. We also introduce the characterisation techniques that were used in the study of this set of samples, scanning electron microscopy (SEM) and atomic force microscopy (AFM). Photoluminescence was also used in the characterisation of these samples, but the technical details were covered in the previous chapter. Based on these measurements, we shall discuss in Chapter 9 the arsenic pressure dependence of the properties of QD ensembles formed with the same deposited InAs coverage.

8.1 Description of Nine Samples Having a Uniform InAs Coverage

The nine samples having a uniform InAs coverage (Series #2) presented in this chapter were grown following the structure depicted on the right hand side of Figure 21. As explained in Section 5.3, a 600.0 nm[24] GaAs buffer at 0.2 nm/s and a temperature of ~600 °C. Following this, 1.9 monolayers (ML) of InAs were deposited at 0.02 nm/s at ~515 °C. The samples were then annealed *in situ* during a 60 sec growth interruption at the same temperature. The samples were then capped with 100 nm of GaAs at ~515 °C , burying the QDs that had formed during the anneal. These are the same nominal InAs coverage, InAs deposition temperature, and anneal time used to produce the

[24] The 100nm difference in buffer thickness between the first and second set of samples is inconsequential.

graded samples presented in Chapter 7. For each sample a different As_4 pressure was used throughout the deposition and anneal of the InAs, and subsequently returned to the nominal value for GaAs growth. For the purpose of performing scanning electron microscopy (SEM) and atomic force microscopy (AFM), uncapped QDs were grown on the surface at the nominal growth conditions of the buried QDs. These 'surface-QDs' are inactive in PL.

Unlike the samples described in Chapter 7, the nine samples presented in this chapter (Series #2) were rotated throughout the growth in order to produce uniform coverages throughout the growth structure. In the case of these nine samples, the trends observed are due to the difference in arsenic pressure when comparing a sample to another within this series as well as to one from Series #1.

In the next two sections, we present the surface microscopy of these samples that was performed using SEM and AFM. These are real space measurement techniques (as opposed to LEED and RHEED which we have discussed earlier). In the case of MBE-grown structures, SEM and AFM can offer considerable information on post growth characteristics of exposed surfaces. In order to maintain surface morphology for the ex-situ characterisation, the heater power was cut off after the annealing of the surface InAs layer, and the arsenic flux was cut off after the sample reached a sufficiently low temperature (~350°C). The SEM and AFM measurements were performed a few weeks after growth. Through this time, they were stored in nitrogen purged cabinets. This should have kept oxidation and contamination to a minimum, and we have no evidence that the features of interest (size, width and density) of the QDs are in any way affected. With the assistance of the

author, the AFM images were acquired by Simona Moisa[25], and the SEM images were acquired by Jeff Fraser[26] at IMS/NRCC. The analysis of the images was carried out by the author.

8.2 Scanning Electron Microscopy

8.2.1 Technique

SEM can provide information on surface topography and composition with high resolution and excellent depth of focus at high magnification. In this technique, a focussed beam of electrons is scanned over a selected scan area on a surface. Backscattered and secondary electrons are then detected, and their intensity is mapped to form an image of the scan area. The imaging process, which occurs in-vacuo can be broken down into four steps: (1) production of electrons (electron gun), (2) formation of stable electron beam (electronic lens system), (3) beam-sample interaction (secondary electrons, back scattered electrons, X-ray signal), and (4) detection (including image formation). What is of primary interest for understanding this technique are the electron-sample interactions. These can be elastic or inelastic. Inelastic scattering of incident electrons is due to interactions with atomic nuclei which can lead to the production of X-ray photons, or to interactions with atomic electrons which can lead to the production of "secondary electrons" (for instance by the Auger process, as discussed in Section 6.2). Elastic scattering of incident electrons is due to interactions with the Coulomb field of the atomic nuclei; electrons which are "backscattered" at a sufficiently shallow depth are available for detection, and "forward-scattered" electrons must undergo further

[25] IMS/NRCC, Building M-50, 1200 Montreal Rd, Ottawa, Ontario, K1A 0R6.
[26] *Ibid.*

interactions if they are to lead to a detectable signal. The total near-surface volume from which a useful signal of scattered electrons is detected defines the "interaction volume."

Within the interaction volume, secondary electrons come from a smaller volume (nearer to the surface) than do the backscattered electrons, and therefore imaging secondary electrons will produce higher resolution images. Secondary electron emission increases as the angle between the beam direction and the surface normal increases; this produces topographical contrast in the images. This is due to the surface intersecting a greater area in the interaction volume, therefore allowing for the escape of a greater number of electrons. Backscattered electron emission increases with the atomic number of the material contained within the interaction volume. Secondary electrons provide topographic detail, backscattered electron provide compositional or crystallographic contrast, and the X-ray signal provides quantitative micro-analytical detail. In our measurements, the secondary electron signal was used in the imaging process.

The detectable electrons will have an angular distribution from the point of interaction, and the presence of inelastic interactions means that they will be spread out in energy from 0 eV up to the elastic peak energy. The secondary electrons dominate the spectrum below a few tens of eV, above which the backscattered electrons dominate up to and including the elastically scattered electron peak.

The incident electron beam is scanned stepwise over the target area, stopping at each point for a specified dwell time. The electron signal is measured using a scintillator producing a proportional (amplified) electrical signal. Electron beam current is used to control signal strength, and the scan area on the surface is used to control the magnification factor. Signal to noise ratio is

a primary concern. Although noise can be introduced by the lens system, the two main sources of noise in the image are the statistical nature of the signal emission from each point in the scan at the sample surface, and the amplification system in the detection system.

In principle, maximum resolution is determined by the diameter of the electron beam. In practice, the resolution is limited by the width of the final probe, which is the interaction volume of the electrons in the near surface region of the sample. This interaction volume varies, both in width and depth[27], as a function of material composition and incident beam energies. Therefore, the resolution is a function not only of beam size, but also beam energy and atomic number of the constituents of the sample surface, and signal to noise will contribute to the limiting of the final practical resolution. In the case of our measurements, the smallest resolvable feature is ~ 3nm.

8.2.2 Experimental Setup

The specific apparatus used in the characterisation of our samples consisted of a cold field emission scanning electron microscope, model Hitachi S-4700 type II. The images were acquired using a 5.0 kV electron beam energy, using a digital raster pattern, at a working distance of ~ 5 mm. The image contrast is due to topography, and no signal processing was done.

[27] Related to electron penetration depth in Section 6.1.

8.2.3 The SEM Images

Figure 52 contains SEM images of the surface QDs on three samples covering the range of arsenic pressures investigated. The only image processing which was done on the recorded images is a "Histogram Stretch". This is a procedure that linearly fits the range of recorded intensity data in the raw image over the entire greyscale consisting of 256 tones (8 bits); highest electron intensity is therefore mapped as white, and lowest intensity as black. This does not distort the images, and in fact does not in anyway affect the analysis procedure except for one practical point: This manipulation renders the features of each image more easily visible, and therefore allows for the visual identification of QDs in the scan area.

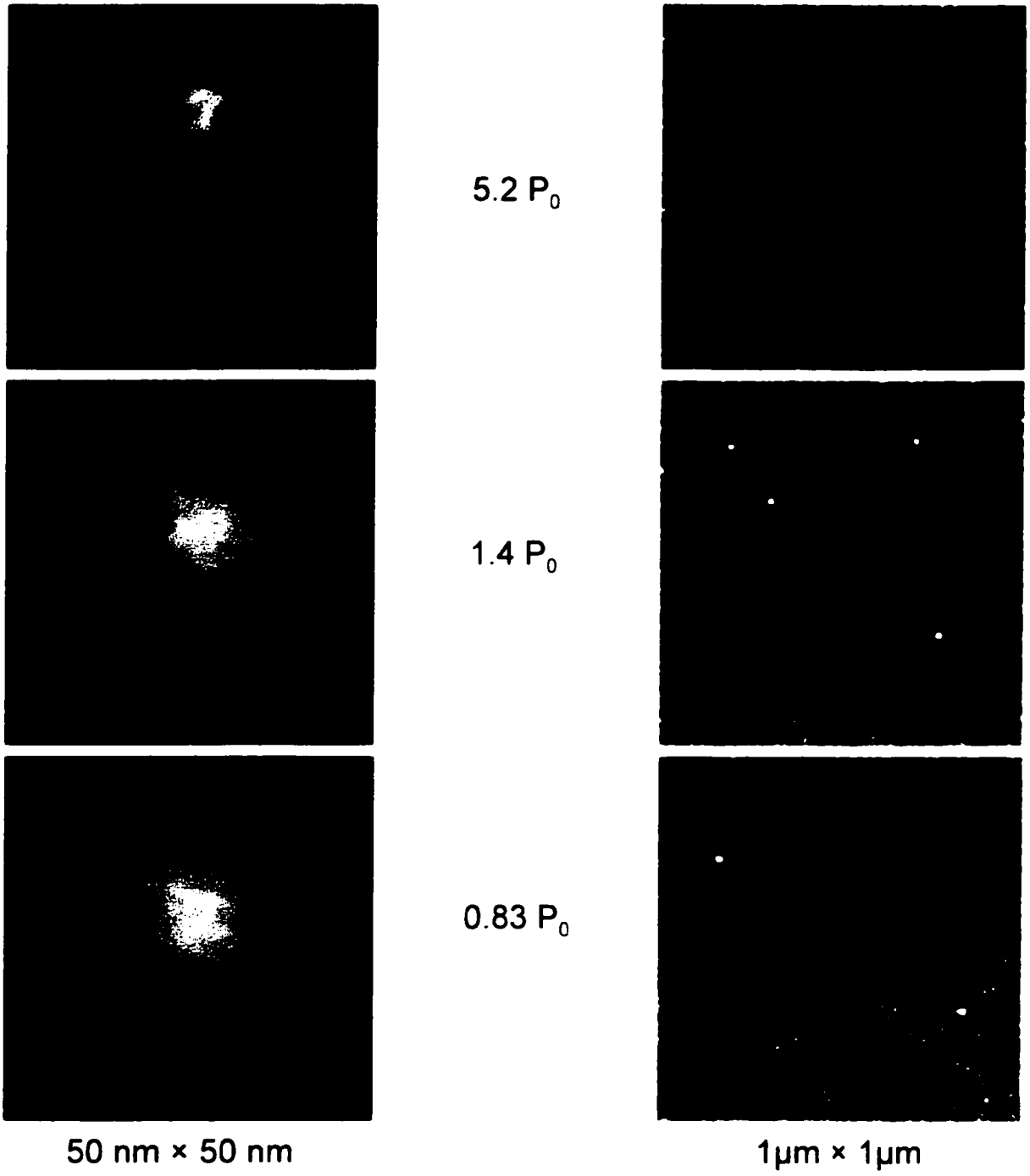

Figure 52. Examples of SEM images showing the size and density of uncapped QDs as a function of arsenic pressure used during the deposition and anneal of the InAs.

The width of each QD was determined by taking line profiles through the centre of each QD along 4 directions at 45° from one another. To reduce noise in the profiles, the line width used was chosen to be 10% of the width of the QD.[28] The error bars on the QD widths in Figure 54 are the standard deviation of the set of average widths (averaged over direction) for all the measurable QDs from the images from each sample. For the $P_{As4} = 0.83P_0$ sample, 16 widths were measured; for the $P_{As4} = 1.4P_0$ sample, 20 widths; for the $P_{As4} = 2.0P_0$ sample, 40 widths, for the $P_{As4} = 2.5P_0$ sample 28 widths; and for the $P_{As4} = 5.2P_0$ sample, 48 widths[29].

The QD density was determined by counting the QDs in all large area images (order of a few μm^2) for each sample, and dividing the total by the total area of the group of images. Because of the limited number of images, it was more efficient to do this counting "by eye" than to do it using an image analysis package. The relative value of the error bars on the QD densities in Figure 54, $\Delta n/n$, is equal to one over the square root of the total number of QDs counted for each point on the graph. For the $P_{As4} = 0.83P_0$ sample, 17 QDs were counted over 2 images; for the $P_{As4} = 1.4P_0$ sample, 18 QDs over 1 image; for the $P_{As4} = 2.0P_0$ sample, 182 QDs over 3 images, for the $P_{As4} = 2.5P_0$ sample, 414 QDs over 5 images; and for the $P_{As4} = 5.2P_0$ sample, 140 QDs over 1 image.

Already, from Figure 52 it can be seen qualitatively that the QDs produced at higher arsenic pressure are smaller and have a higher density. We leave quantitative measurements for Section 8.4 where they shall be presented along with similar measurements from AFM images.

---

[28] If after measuring the width of the QD, it was revealed that the line width used was different than 10% of this measurement, the procedure was repeated using a line width equal to 10% of the true width.

[29] Because of the very low QD density of the lower pressure samples, it was difficult to obtain high counts of QDs, thereby providing poor statistics for the width and height measurements. Fortunately, there is a "compensating effect" due to the fact that these samples have very sharp QD size distributions, as conclusively evidenced by the sharp PL emission lines seen in Figure 56.

8.3 Atomic Force Microscopy

8.3.1 Technique

AFM is an important tool for the characterisation of surface morphology. Although its design is based on STM, AFM does not make use of a tunnelling current between the probe and surface. This makes it possible for AFM to be used in the characterisation of weakly conducting materials such as undoped semiconductor samples. AFM images are obtained by measuring the force on a sharp probe scanned in near contact with a surface. The usual AFM probe consists of a sharp tip attached to a cantilever arm having a very small spring constant (≈ 1 N/m). The possibility of scanning artifacts is considerable. The finite size and shape of the probe render some of the finer details of the surfaces studied unresolvable: unless they are much larger than the probe, raised features are made to appear wider than their actual size and depressed features are made to appear smaller.

AFM images include convolution effects of the probe shape. If, for instance, the probe is somehow dirty (e.g. after picking up a nanoscopic speck of debris on a surface), the new effective shape of the probe (probe+debris) will be "reproduced" in the details of the image. Correcting for the convolution effects would require precise knowledge of the size and shape of the tip; as shall be discussed in the following section, this was not necessary in our analysis. Other possible distorting effects include electrostatic attraction between the probe and surface contributing to the deflection of the cantilever and nonlinearities in the probe actuation mechanism. Nonlinearities in the actuation

mechanism are compensated for by proper calibration of the instrument. For our measurements, electrostatic effects and probe contamination effects were readily identified, and avoided by scanning samples containing certain reference or expected features[30].

There are three modes of operation: constant force imaging or contact mode, variable force imaging or non-contact mode, and tapping mode. In general, for all three modes a feedback voltage is mapped as a function of position on the sample surface, thereby creating an image of the surface topography. Our measurements were obtained by using the tapping mode, which we presently describe. For the sake of completeness, we also briefly describe the two other modes.

In the contact mode, a low constant force is applied to the cantilever and the probe is scanned across the surface. A feedback mechanism adjusts the distance from the surface so as to keep the cantilever force constant. The deflection of the cantilever, as measured using a laser reflected off the cantilever, is mapped as a function of position producing an image of the surface topography. This mode is particularly susceptible to the image distorting effects mentioned earlier.

In the non-contact mode, the probe is kept a small constant distance above the surface. The attractive Van der Waals force acting between the probe and surface is detected and mapped as a function of position. This mode is less susceptible to the image distorting effects mentioned earlier, but because the Van der Waals force is very weak, the images produced are inherently lower resolution than in contact mode.

---

[30] In tapping mode (described on following page) contaminated tips will display a characteristic "double peaked" frequency response curve. This can be used to eliminate bad tips.

In the tapping mode, the mode that was used for our measurements, the cantilever is made to oscillate at or near its resonant frequency using a piezoelectric crystal. The frequency of oscillation typically ranges from 50 kHz to 500 kHz. As the probe is lowered closer to the surface and its motion brings it into intermittent contact with the surface, its oscillation is dampened. A feedback mechanism adjusts the probe-surface separation in order to maintain the oscillation amplitude constant. The feedback voltage is mapped as a function of position, producing an image of the surface. This mode greatly reduces the effect of friction, adhesion, electrostatic attraction and other image distorting effects. The tapping mode is particularly useful in the imaging of soft, adhesive or fragile materials. Furthermore, this mode causes less surface damage than the contact mode.

8.3.2 Experimental Setup

The specific apparatus used in the characterisation of our samples consisted of a Digital Instruments - Nanoscope IIIa Atomic Force Microscope operating in tapping mode and using an etched silicon probe tip (force constant: 20 - 100 N/m; resonant frequency: 200 - 400kHz; nominal tip radius of curvature: 5 - 10nm; cantilever length: 125μm; cantilever configuration: single beam; reflective coating: uncoated; tip half angle: 17° side, 25° front; 10° back). Specifically, our AFM images were acquired using probes ~ 10 nm in radius operating at ~ 320 kHz (which is approximately 10% under their resonant frequency).

8.3.3 The AFM Images

Figure 53 contains AFM images of the surface QDs obtained from the same three samples as the SEM images presented in Figure 52. The only image processing which was performed on the AFM images is a long range polynomial background subtraction. This does not distort the QD images since the background curvature is approximately two orders of magnitude less than that of the QDs.

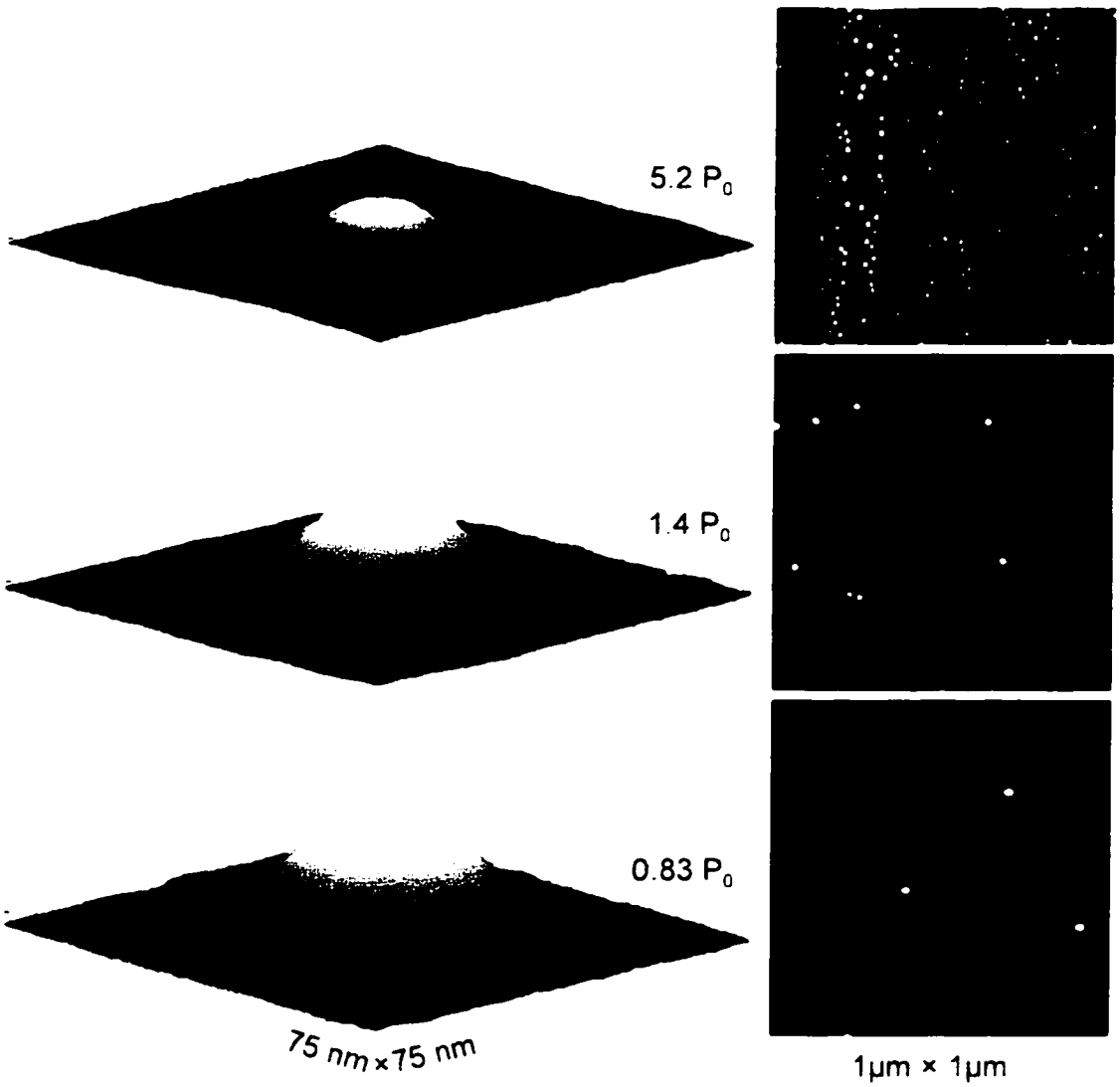

Figure 53. Examples of AFM images showing the size and density of uncapped QDs as a function of arsenic pressure used during the deposition and anneal of the InAs.

The height of each QD was determined by measuring the elevation difference between the top most point on each QD and the base nearby each QD in the topographical images recorded of each sample. The error bars on the QD heights in Figure 54 are the standard deviation of the set of heights for all the measurable QDs from the images from each sample. For the $P_{As4} = 0.83P_0$ sample, 5 heights were measured over 2 images; for the $P_{As4} = 1.4P_0$ sample, 9 heights over 2 images; for the $P_{As4} = 2.0P_0$ sample, 3 heights over 1 image, for the $P_{As4} = 2.5P_0$ sample, 4 heights over 1 image; and for the $P_{As4} = 5.2P_0$ sample, 8 heights over 2 images.

The height measurements performed with AFM probes are not plagued with the image distorting effects discussed in Section 7.3.1. Width measurements are, and determining absolute widths of QDs[31] by AFM would require a deconvolution of the probe shape. It is interesting to note that the widths measured by AFM were greater than those measured by SEM by a factor of approximately two. This is reasonable, considering that the QD widths are of the order of 10 nm, and the AFM probe tips used were ~ 10 nm in size. To first order, the convolution of these adds their values, thereby approximately doubling the QD widths.

We verified that the QD densities in the AFM images were consistent with those seen in the SEM images. The counting of the QDs was performed following the same procedure, and the results were not significantly different.

[31] General trends can be identified in spite of this effect.

8.4 Measurements: Width, Height, and Density of the Quantum Dots

Figure 54 summarises the surface microscopy measurements of the uncapped QDs as a function of the As_4 pressure used during the QD deposition and anneal which is varied over a range of one order of magnitude, from $0.6P_0$ to $5P_0$. The QD density increases two orders of magnitude (2 to 100 QD/μm^2). Most of this increase occurs over approximately half of the pressure range, after which the QD density levels off. There is insufficient data in the upper half of the pressure range to conclusively ascertain a change of slope in the evolution of the QD density as a function of pressure. The QD height and width reduce by factors of almost three (11 to 4 nm) and two (32 to 16 nm) respectively. Although not as pronounced, here also the change in these two parameters occurs mostly over the lower half of the pressure range.

The change in aspect ratio (height:width) from approximately 1:3 at $P_{As4} = 0.6P_0$ to approximately 1:4 at $P_{As4} = 5P_0$ is barely outside of the uncertainty, but QDs formed at higher pressures do seem to have a slightly lower aspect ratio.

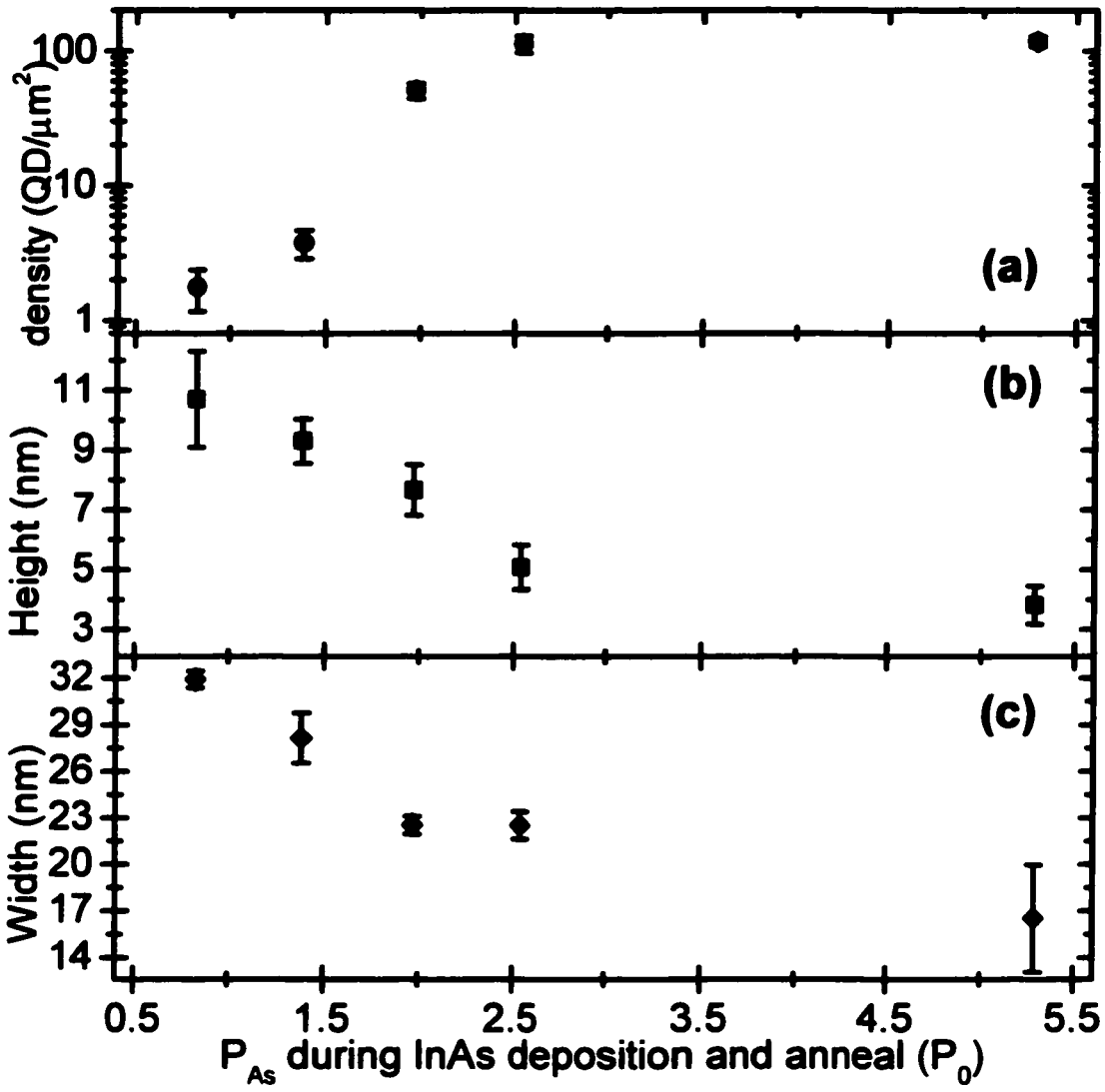

Figure 54. Results of surface microscopy of uncapped QDs (Series #1): The widths and densities were determined by SEM and the heights were measured by AFM. From ref. [14].

A quantity that will be of interest in our discussion when comparing to the incorporation-diffusion length (IDL) is the average inter-QD distance. It can be estimated as the inverse square root of the QD densities in Figure 54a, decreasing with increasing As_4 pressure from 0.8 μm to 0.1 μm, as shown in Figure 55.

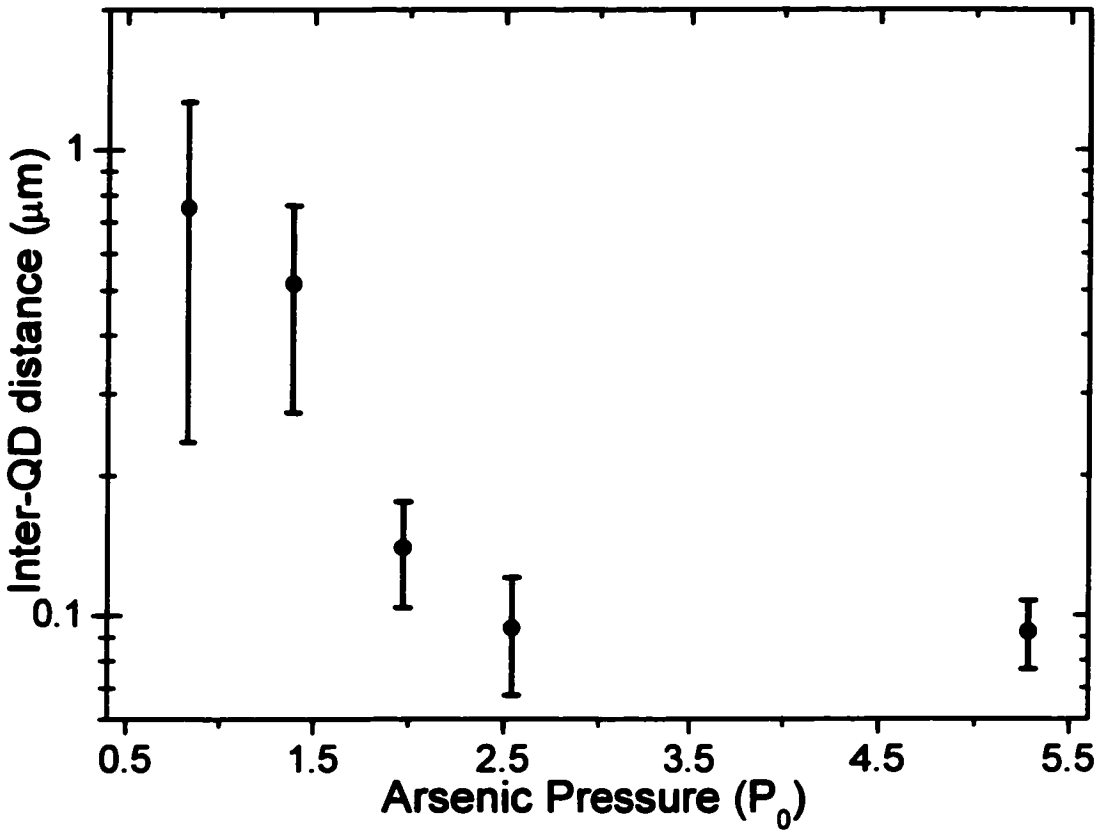

Figure 55. Average inter-quantum-dot distance calculated from the densities determined by the SEM characterisation of the uncapped QDs.

8.5 Photoluminescence

A description of the technique and the setup can be found in Section 7.2.1, and a guide for interpreting the spectra can be found in Section 7.2.3.

8.5.1 Measurements: PL of Quantum Dots as a Function of Arsenic Pressure

Each PL spectrum in Figure 56 comes from a sample produced at a different arsenic pressure (during InAs deposition and anneal). These PL spectra show how the electronic shell structure of the QDs can be adjusted by varying the arsenic pressure. In Figure 56a, the reduced wetting layer (WL) intensity relative to the QD intensity in the samples produced at As_4 pressures greater than $1.4P_0$ is due to the substantially increased QD density [31]; this is verified by SEM. The WL emission line redshifts from approximately 862 nm to 869 nm as the As_4 pressure increases from $0.59P_0$ to $2.5P_0$, and at $1.2P_0$ it is at 866 nm. At $P_{As4} = 5.2P_0$ no WL emission is detected. In the spectra in Figure 51 displaying a comparable ratio of WL to QD intensity, the WL redshifts from 866 nm at $P_{As2} = 1.0P_0$ to 873 nm at $P_{As2} = 4.0P_0$. The positions of the WL emission line near $P_{As2/As4} = 1P_0$ obtained from both figures are equal, and even though the values near $P_{As2/As4} = 3P_0$ differ slightly, the redshift of the WL with increasing arsenic pressure is observed in both figures. Therefore, from both series of samples we see that higher arsenic pressures favor either a thicker WL or a reduction in the alloying of the (nominally pure) InAs WL with the underlying GaAs.

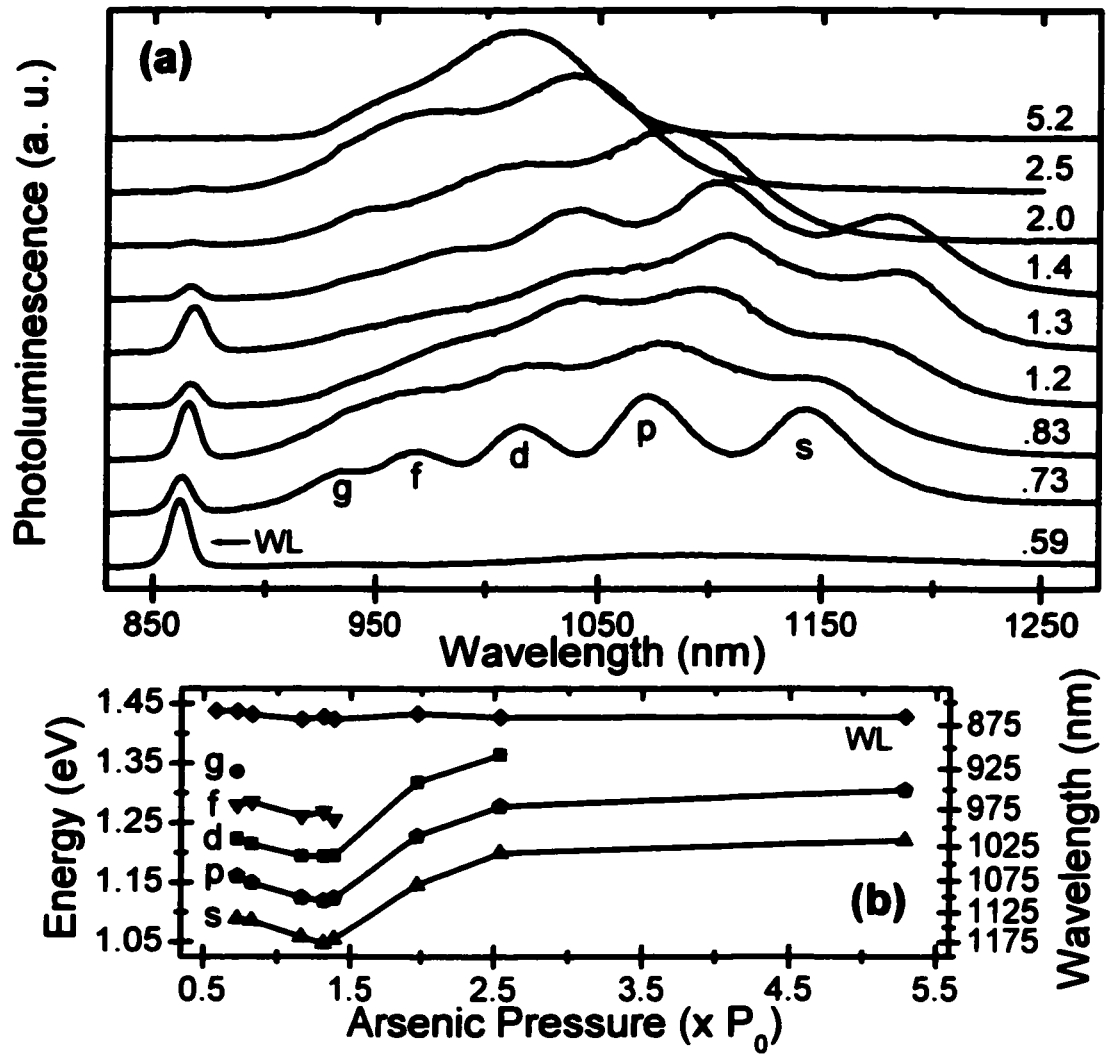

Figure 56: PL spectra for the 9 samples having a uniform InAs coverage (Series #2). (a) Complete set of spectra. The As_4 pressure at which the InAs was deposited and annealed for each sample is written in units of P_0 on the right hand end of each curve. The WL and QD recombination peaks are indicated. All spectra were normalized to the same maximum intensity and offset for clarity. (b) Energy level evolution with As_4 pressure. The state filling spectroscopy was obtained with PL at 77K, exciting above the GaAs barrier using a power of a few kW/cm^2. From ref. [14].

As the As_4 pressure is raised from $0.59P_0$ to $1.3P_0$, the QD emission lines redshift by as much as 40 nm, and as the pressure is further raised to $5.2P_0$ the shift in PL reverses, and the emission lines

blueshift by more than 170 nm. This trend is observed for all the resolved electronic shells. Note that for low As_4 pressures, five confined shells are observed, but for high As_4 pressures, as the emission lines are blueshifted, the total number of electronic shells is reduced from five to three. As the As_4 pressure is raised, the full width at half maximum almost doubles, going from ~35 nm to ~70 nm, while the intersublevel spacing increases only slightly (Figure 56b); this leads to poorly-resolved shells for the samples grown at high As_4 pressures. All these observations, including the strong shifts in PL are solely due to the variation of the arsenic pressure. All other growth parameters were kept constant.

9 Discussion and Conclusion

In this final chapter, after an introduction, we will discuss the microscopy measurements performed on the uncapped quantum dots (QDs) and the PL measurements of the capped QDs presented in Chapter 8. We shall explain the role of the diffusion mediated transfer of adatoms in the stabilisation of the QD sizes and densities. Following this, we shall discuss the low arsenic pressure samples of which the PL measurements do not follow the trend expected based on the microscopy measurements presented in Chapter 8, and we shall also discuss the trends observed in the graded samples of Chapter 7. Combining the observations from both sets of samples will lead us to propose how QDs are modified during capping procedures. Finally, we will summarise the important points of this discussion.

9.1 Interpretation

9.1.1 Introduction

In Chapter 8, we presented surface microscopy measurements and PL measurements of QDs displaying well-resolved excited state structures. This well-resolved excited state structure allows for the clear identification of the trends in the QD ensembles as a function of arsenic pressure. The microscopy data show that the average inter-QD distance reduces as a function of increasing arsenic pressure used during the deposition and anneal of the InAs. In Section 9.1.2 and 9.1.3, we discuss

this trend in inter-QD distance, and the trends in QD width and height in correlation with the trends seen in PL spectra.

In the deposition procedure used in our experiments, the InAs deposition flux is interrupted at the point of 2D to 3D transition. Because of this, the adatoms diffusing on the surface during the evolution of the QDs are adatoms of the wetting layer and adatoms that have detached from the periphery of already existing QDs. At the point of 2D-to-3D transition, as the QDs nucleate following the layer by layer growth stage of the Stranski-Krastanov (SK) growth mode, adatoms must leave the wetting layer to contribute to the QD ensemble. The PL measurements of coverage graded samples, such as Figure 15 support this assertion. Indium atoms will have to leave binding sites incorporated into the wetting layer surface, in step edges, or in kink sites, as described in Section 3.1. They will then move through more weakly bound adatom sites on the surface on the way to final states of lower energy. As discussed in Section 3.3, there is a thermodynamic drive in the system for the aggregation of the QDs. The system will approach this equilibrium by the diffusion mediated transfer of adatoms. The distance over which these adatoms can travel by diffusion on the surface before incorporation, measured as the IDL by Nishinage for InAs and GaAs, determines an area of exchange with the QD ensemble surrounding each QD. This distance limits the approach of the system to equilibrium.

We will end this introductory section by proposing a scenario for the 2D to 3D transition of InAs grown on GaAs. In Section 6.6, Figure 48, we saw that the time of transition from 2D layer by layer growth of the wetting layer to 3D growth of the QDs decreases with increasing arsenic pressure. We propose that this is consistent with an increase in the trapping or attachment probability

of indium adatoms due to the increase in population of active arsenic species on the surface as the arsenic pressure is increased. For a 2D island to become a 3D island, a new layer must nucleate on top of it; the rate of this nucleation is proportional to the population of adatoms on top of the 2D island [2]. We therefore surmise that an increase in the trapping probability of indium adatoms associated with an increase in arsenic pressure should lead to an increase in the rate of nucleation of new layers. Conversely, decreasing the arsenic pressure, decreases the population of active arsenic species, which decreases the trapping probability of indium adatoms, thereby retarding the 2D to 3D transition. When an area of the wetting layer undergoes the transition to 3D growth, it will consume some of the adatoms within a radius surrounding it that is related to the IDL, thereby preventing other points within this radius from undergoing the 2D to 3D transition. This consumption of adatoms continues after the formation of the 3D island, however, as discussed in Section 3.4, the growth rate of the 3D island is restricted by a strain-induced barrier for adatom incorporation that increases with island size.

9.1.2 The Arsenic Pressure Dependence of the Inter-Quantum Dot Distance

In Figure 55, we determined the inter-QD distance for the nine samples of surface QDs. The key observation that can be made at this point is that these inter-QD distances are consistent with reported values of group III IDL [67-70,99,100]. Nishinaga and coworkers, in a series of studies [67,69,70], obtained IDL values decreasing with increasing As_4 pressure for both GaAs and InAs homoepitaxy. For both systems in comparable pressure ranges, the IDL values ranged from approximately 2 or 3 μm at low As_4 pressures down to approximately 0.7 μm at higher pressures. They performed their measurements in growth conditions, that is temperature and As_4 pressures,

leading to the (2×4) reconstruction of the surfaces. In contrast, the QD ensembles measured for Figure 54a were grown in conditions leading to the c(4×4) reconstruction of the GaAs surface during GaAs growth at 0.2 nm/s at 515 °C (no reconstruction is observed during the InAs growth). Therefore, based on the discussion in Chapter 6, we deduce that our QD ensembles were grown at As_4 pressures higher than those explored by Nishinaga and coworkers. Indeed, the inter-QD distances fall within the range obtained if the IDL results of Nishinaga and coworkers are extrapolated to higher pressures.

As discussed in Section 4.3, the incorporation-diffusion length (IDL) for indium adatoms reduces with increasing group V pressure due to the increase in trapping probability due to the increase in population of active arsenic species on the surface. These same processes should lead to a decrease in inter-QD distance and an associated reduction in QD size with increasing arsenic pressure. The blueshift in PL above $P_{As4} = 1.3P_0$ (Figure 56) can be understood in terms of such a reduction in QD size with increasing pressure (Figure 54). Indeed as discussed in Section 2.4, QD emission lines shift to shorter wavelengths with decreasing QD size. It is also possible, particularly in our higher QD density samples, that the increase in QD density with increasing pressure (Figure 54a) contributes to the blue shift. However, it must be noted that these QD ensembles have QD densities that are one or two orders of magnitude smaller than those discussed in Section 4.1, and because of this a density related effect is unlikely. Regardless, in the case of both a size or a density effect, in the samples presented in Chapter 8, it is the use of higher As_4 pressures during the growth and anneal of the QDs that leads to structural changes in the QD ensemble (reduced QD size and/or increased QD density), such that the emission lines of the QDs produced above $P_{As4} = 1.3P_0$ blueshift with increasing As_4 pressure.

In Section 6.6, using RHEED movies of the deposition of InAs on GaAs, we measured the time of transition from the 2D layer by layer growth to 3D QD growth as a function of growth temperature and arsenic pressure. Over the explored ranges, the variation in this transition time due to the change in arsenic pressure observed using RHEED movies in Section 5.5 is approximately four times smaller than the variation due to the change in growth temperature. Comparing Figures 16 and 56, the shifts in PL of the QD excited state structure due to the variation of the arsenic pressure are greater than the PL shifts due to variations in growth temperature. The shifts in PL observed in Figure 56, the trends seen in the microscopy of the uncapped QDS in Figure 54, and in general the effects attributed to the arsenic pressure in this thesis, are therefore not primarily attributable to changes in timing of the 2D to 3D transition. This change in timing may contribute to the above mentioned effects, either increasing or decreasing their magnitude, but based on this comparison, should not be the principal source of the changes in the QD ensembles leading to the observed PL shifts.

Some mechanism must limit the evolution of QD ensembles towards a lower density of larger QDs; otherwise the five QD ensembles in Figure 54 would have evolved at least to the QD size and density of the QD ensemble produced at the lowest pressure. The kinetic models presented in Section 3.3 attribute the stabilisation of QD ensembles to changes in the barriers for diffusion and attachment/detachment of adatoms due to the dependence of local strain on QD size. In fact, the size-dependence of local strain is the"key ingredient" in both the thermodynamic equilibrium model and the two kinetically limited models presented in Chapter 3. Nevertheless, it is unlikely that local strain would be dependent on the arsenic pressure, as are the trends in the microscopy measurements in Figure 54. We therefore believe that, although the size-dependent strain at the periphery of QDs

is the cause for the sharp size distribution, it cannot explain the arsenic dependent observations made in Chapters 7 and 8. The rate of diffusion mediated transfer of adatoms also plays a role in determining the properties of QD ensembles: The distance adatoms can travel limits the inter-QD distance of QD ensembles formed at coverages near the 2D to 3D critical coverage, such as those presented in Chapter 8.

9.1.3 The Arsenic Pressure Dependence of the Size Distribution of Quantum Dots

In Section 3.3.2.1, in the Dobbs model, we saw that it is the QD size dependent barrier for adatom diffusion E_a that leads to the sharp distribution of QD sizes. As discussed in the previous section, this strain-induced diffusion barrier is not expected to depend on the arsenic pressure. Therefore the arsenic pressure cannot act through such a local strain effect to lead to an arsenic pressure dependence of the QD size distribution. However, the arsenic pressure affects the surface population of active arsenic species, which in turn affects the trapping probability of group III adatoms. Therefore, by increasing the trapping probability of group III adatoms, an increase of the arsenic pressure limits the diffusion process that leads to the sharp distribution of QD sizes.

The role of the arsenic pressure described above is not to act as a cause for the sharp distribution of QD sizes, but to act in affecting the diffusion mechanisms that bring the QD ensemble to a sharp size distribution. Specifically, the adatom trapping probability associated with the arsenic pressure may slow down the evolution of the QDs, after their nucleation, so that the system does not reach as sharp a size distribution as it would at a lower arsenic pressure. Increasing the arsenic pressure should therefore have a somewhat similar effect to decreasing the annealing temperature.

This is indeed observed in the width of the emission peaks in the PL spectra as a function of decreasing temperature in Figure 16 and as a function of increasing arsenic pressure in Figure 56. Furthermore, both an increase in arsenic pressure and a decrease in annealing temperature have an effect on the QD ensemble properties similar to reducing the annealing time; this is evidenced by the spectra for $t_{anneal} \leq 60$s in Figure 17. Conversely, lower arsenic pressures lead to sharper QD size distributions.

9.1.4 Quantum Dot Modification During Capping

As discussed in the previous section, The blueshift above $P_{As4} = 1.3P_0$ is attributable to the reduction in QD size as a function of increasing arsenic pressure seen in Figure 54. But the redshift below $P_{As4} = 1.4P_0$ cannot be explained like this since, for the surface QDs, the reduction in QD size with increasing arsenic pressure is observed over the whole pressure range. The only difference between the surface QDs and the buried QDs is that the buried QDs were overgrown with GaAs to cap them. In our final analysis, we will therefore have to consider the mechanisms in operation during capping to figure out what is going on.

Information on the QD modifying effects of capping can be deduced from the indium flushed samples of Chapter 7. In Section 7.2.4, we showed that the effects of the indium flush procedure on the $P_{As2} = 1.0P_0$ sample had somehow been made more pronounced, increasing the expected blueshift[32] of the QD emission [59], and thereby placing the s-level emission of the $1.0P_0$ sample at

[32] Through most of the previous sections, shifts in PL were noted in function of arsenic pressure when comparing one sample to another, or as a function of InAs coverage when comparing different positions on the coverage graded samples. The blueshift caused by the indium flush is noted by comparing the QDs of a given sample before and after capping.

a shorter wavelength than that of the $3.0P_0$ and $4.0P_0$ samples, as shown in Figure 51. As seen from the microscopy measurements performed on the uncapped QDs of Chapter 8, QDs formed at lower arsenic pressures are larger than those formed at higher arsenic pressures. This should have placed the s-level emission of the $1.0P_0$ at a longer wavelength than that of the $3.0P_0$ and $4.0P_0$ samples, neglecting the effects of the indium flush. Because of this, the increased blueshift of the s-level of the $1.0P_0$ sample cannot be due to initially smaller QDs; it is most probably due to some change in the QD modifying effects of the indium flush. Considering that the primary observed effect of the indium flush is the reduction in height of the QDs, we can propose that the QDs in the $1.0P_0$ sample were reduced in height more substantially.

In the discussion in Chapter 8 of the continuously capped samples, structural information on the buried ensemble is inferred from the surface QDs to explain the blueshift above $P_{As4} = 1.3P_0$. However, we find no trend in Figure 54 that could explain the redshift of QD emission as the As_4 pressure increases from $0.5P_0$ to $1.3P_0$. Based on the size evolution of the surface QDs, the trend in PL from $0.5P_0$ to $1.3P_0$ should be a blueshifting of the QD emission that lines up with the trend above $1.3P_0$. The QDs produced below $1.3P_0$ emit at a much shorter wavelength than an extrapolation of the trend above $1.3P_0$, and the size evolution of the uncapped QDs would suggest. Based on these two mutually consistent observations of Figure 54, not only do the QDs produced below $1.3P_0$ emit at shorter wavelengths than one would expect, the trend in PL from $0.5P_0$ to $1.3P_0$ is also the opposite of what would be expected. Neglecting possible compositional effects, this implies that the capped QDs produced from $P_{As4} = 0.5P_0$ to $1.3P_0$ increase in size with increasing As_4 pressure.

We now note that in both sets of samples, the indium flushed samples of Chapter 7 and the continuously capped samples of Chapter 8, the QDs produced at lower arsenic pressure display relatively blueshifted PL, and that in the case of the indium flushed samples, as explained above, this appears to be due to an enhancement of the QD height reducing effects of this discontinuous capping procedure. As discussed in Section 4.4, the mechanisms that lead to this effect are the strain-induced preferential coverage by the GaAs of the wetting layer leading to a lack of covering of the QDs, and consequently the out-diffusion of QD material (or in-diffusion of capping material) and/or the evaporation of QD material. These mechanisms are not limited to operating during discontinuous capping procedures; they can occur during continuous capping such as was performed on the samples of Chapter 8. Therefore, a plausible explanation for the redshift from $P_{As4} = 0.5P_0$ to $1.3P_0$ in the continuously capped samples of Chapter 8 is that the PL-active QDs, the buried QDs, produced below $P_{As4} = 1.3P_0$ are somehow modified structurally and/or compositionally such that the (initially) larger QDs, those grown at $P_{As4} = 0.73P_0$ for instance, are more substantially modified than the (initially) smaller QDs grown at $P_{As4} = 1.3P_0$, and the degree of modification is negligible for QDs grown at arsenic pressures greater than $1.4P_0$.

9.1.5 Proposed Model for the Size-Dependent Modification of Quantum Dots During Capping

The conclusions drawn in the previous section suggests that the larger QDs produced at lower arsenic pressures are more susceptible to capping effects than are the smaller QDs produced at higher pressures. To formulate a picture of how QDs may be modified during capping, we must consider the strain distribution in QDs and the surrounding material. Figure 57 displays "building block models" of the strain relaxation in QDs. The GaAs immediately under each QD is slightly stretched

by the InAs, and the InAs is compressed by the GaAs. The further an InAs layer is from the GaAs substrate, the more it is relaxed, that is to say that layer by layer the lattice constant of the InAs approaches it's bulk value. Comparing two QDs of the same height, Fig. 57 (a) and (b), it is the QD having the smallest width that is the most relaxed. Comparing two QDS of the same width, Fig. 57 (b) and (c), it is the highest QD that is the most relaxed. Comparing two QDs containing the same amount of material, Fig. 57 (c) and (d), it is the highest QD that is the most relaxed.

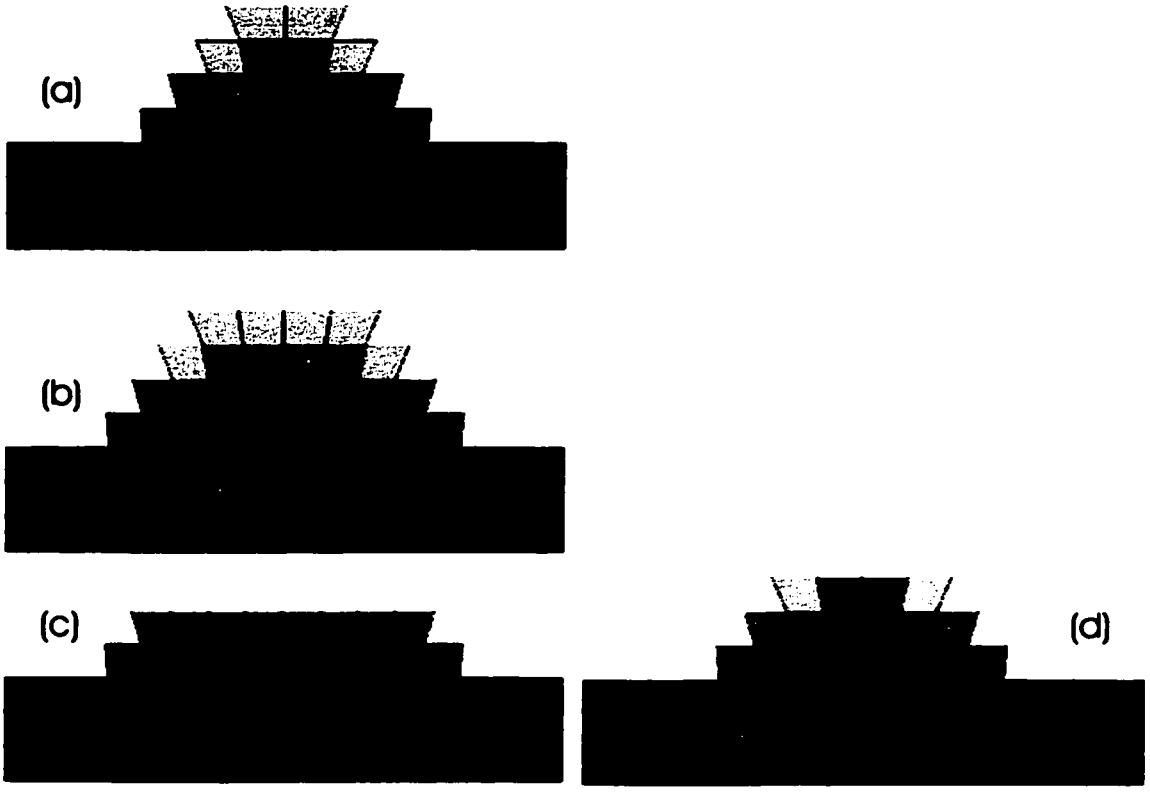

Figure 57. Schematic representation of the lattice deformation in InAs QDs on GaAs. The GaAs is in red, and the InAs is in blue.

Now, if we consider GaAs arriving on this surface to overgrow the QDs, as discussed in Section 4.4 and as described by Wasilewski and coworkers [38], because the lattice constant on the

QDs is close to the InAs bulk value, it is thermodynamically favourable for the GaAs to bind to the wetting layer. In other words, the GaAs does not wet the QDs because if GaAs were to bind to the QDs, it would be strained considerably. The strain to which the GaAs would be subjected if it were to bind to the InAs QDs presumably needs to be reduced before it becomes energetically favorable for the GaAs to overgrow the QDs. Then the QDs remain exposed until, due to changes in the QD ensemble, these more favourable conditions are met.

As soon as the wetting layer is covered, Figure 58, the free bonds available on the surface come from the GaAs. Now, as discussed in Section 3.1, the InAs has a tendency to wet GaAs because InAs adhesion to GaAs is stronger than cohesion of InAs to itself. When GaAs covers the surface between the QDs, this tendency for InAs to wet GaAs is again present. Because of this, InAs starts to diffuse onto the GaAs. This continues until the strain is sufficiently reduced and the GaAs can wet the QDs and cover them. Moreover, since smaller QDs are less relaxed and therefore present less strain to the GaAs, they need not be modified as much as larger QDs before GaAs can cover them. For bigger QDs to reach a sufficient reduction in QD strain, they must loose more material than smaller QDs. Stated differently, larger QDs subject surrounding GaAs to a greater amount of strain, and because of this, larger QDs would presumably need to be modified to a greater extent than smaller QDs before they could be overgrown.

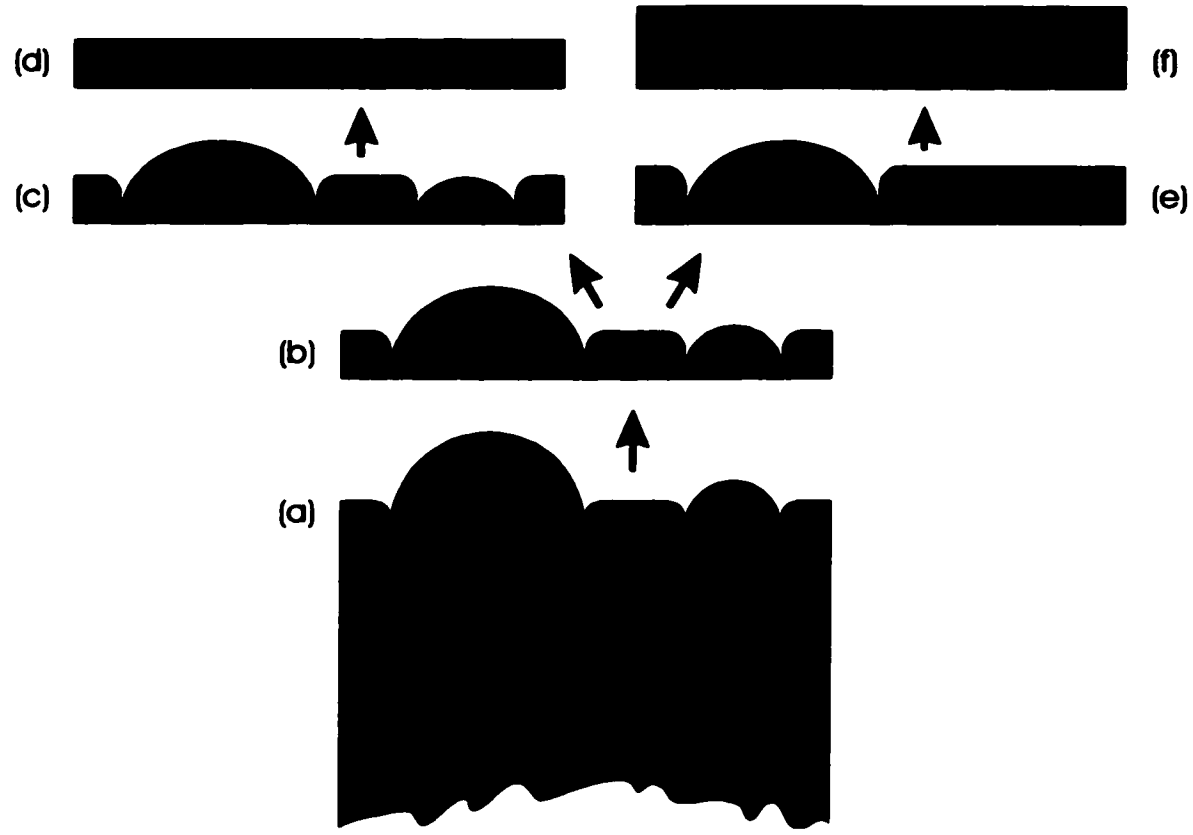

Figure 58. Sequence (a), (b), (c), (d): The effects of the indium flush procedure described in Section 4.1.4. The deposition of the cap is stopped at (c), and the evaporation of the In that has diffused onto the GaAs (not illustrated) occurs in (d). Sequence (a), (b), (e), (f): The proposed model for the modification of QDs during continuous capping procedures. The deposition continues from (a) through (f). The InAs is in blue, and the GaAs is in red.

The QD modifying mechanisms discussed in Section 4.4 can come into effect as soon as GaAs starts to bind to the InAs wetting layer and GaAs bonds become available; their effect does not require an interruption in the deposition of the cap. This could lead to structural and/or compositional modifications of the QDs such as those needed to explain the redshift in PL seen with increasing arsenic pressure up to $1.3P_0$. From the PL measurements, it is not possible to discriminate between a structural modification of the QDs and a chemical modification of the QDs. For this, chemically sensitive microscopy measurements, such as TEM is required. The TEM measurements

of indium flushed QDs in Figure 19 (Section 4.2) have been interpreted [38] as showing a structural modification of the indium flushed QDs. The QD modifying mechanisms operating during a continuous capping procedure are the same as those operating during a discontinuous capping procedure, such as an indium flush. In light of this, Figure 58 has been made to represent the structural modification of the QDs during capping in either case.

9.2 Salient Points

Considering that the three growth control parameters listed in Section 4.2., namely the amount of InAs deposited, the growth temperature, and the anneal time, were identical for all samples and adjusted for optimized QD growth, it is clear that control of these three parameters is not sufficient to engineer predictably QD ensembles. To produce QD ensembles with well-resolved engineered electronic levels, a low arsenic pressure is necessary. Considering the two series of samples, twelve in all, that were studied in this thesis, we believe that the following is happening: For the samples produced using high arsenic pressures, the size evolution of the QDs as a function of arsenic pressure is determined by their size after formation, before they are capped, and for the samples produced using low arsenic pressures, it is a QD modifying mechanism in operation during capping that dominates the size evolution of the QDs as a function of arsenic pressure. It is also possible that the mechanisms discussed in Section 4.3.2. lead to an increased alloying of the QDs with the GaAs cap in the sample produced at an arsenic pressure of $1.0P_0$ in the series of graded samples, such that they include a greater fraction of gallium than the QDs produced at $3.0P_0$ and at $4.0P_0$. Similarly, it is also possible that the redshift seen in the PL spectra below $1.3P_0$ of the series of

samples having a uniform InAs coverage is due to a compositional change caused by an enhancement of the alloying with the underlying GaAs, previously reported for the InAs/GaAs QD system [101]. Such an enhancement might be caused by the increased group III mobility at lower arsenic pressures during the deposition of the InAs.

Alloying mechanisms leading to compositional changes in QDs either before or during capping, and mechanism occurring during capping leading to structural changes in the QDs could act concurrently or consecutively on the same QD ensemble. This study can exclude as an explanation of the blueshifted PL of capped QD samples produced at low arsenic pressures, any mechanism that would lead to structural changes in the QDs before capping; this is based on the surface microscopy of the uncapped QDs.

Considering some of the stated goals of the community researching QDs that were discussed in Chapter 1, namely the attainment of longer wavelengths on GaAs based systems, and an increased control in the production of QDs having specific desired energy levels, the mechanisms acting during capping to modify QDs are limiting. By reducing the size of the QDs or modifying their composition, they make the production of long wavelength QD sources difficult. Because of this, the mechanisms in operation during capping must be better understood.

9.3 Conclusion

RHEED, PL, SEM and AFM were used to demonstrate that the properties of self-assembled InAs/GaAs quantum dots are strongly dependent on the arsenic pressure used during the deposition and anneal of the InAs. The dependence of the quantum dot electronic properties on InAs coverage is altered considerably by changing the arsenic pressure within the range of pressures commonly used in MBE growth. There are clear shifts in the PL spectra of samples grown at different arsenic pressures. These trends are clearly seen due to the controlled production of highly uniform quantum dot ensembles displaying well-resolved excited state structures. At low arsenic pressures, the distribution of material between the wetting layer and quantum dots appears to favour a stabilisation of quantum dot size versus InAs coverage, and therefore of quantum dot emission lines. At high arsenic pressures the quantum dot density increases drastically, the size of the quantum dots decreases, and the excited state structure is rendered difficult to resolve. The effect on emission characteristics of growth conditions modifying quantum dots during capping is observed to be considerable. Finally, both because the arsenic pressure directly affects the quantum dot size and density, and indirectly the extent of the modifications occurring during capping, the arsenic pressure is an essential growth control parameter for the production of high quality quantum dot ensembles having engineered energy states.

References

[1] E. Corcoran and G. Zorpette, in *Scientific American: The Solid State Century*; *Vol. December* (1997), p. 25-33.

[2] I. V. Markov, *Crystal Growth for Beginners.* (Word Scientific, 1995).

[3] L. Goldstein, F. Glas, J. Y. Marzin, M. N. Charasse, and G. Le Roux, Appl. Phys. Lett. **47**, 1099 (1985).

[4] W. J. Schaffer, M. D. Lind, S. P. Kowalczyk, and R. W. Grant, J. Vac. Sci. Technol. B **1**, 688 (1983).

[5] D. Leonard, M. Krishnamurthy, C. M. Reaves, S. P. Denbaars, and P. M. Petroff, Appl. Phys. Lett. **63**, 3203 (1993).

[6] R. G. Thoren, Proc. Society of Photo-Optical Instruments and Optical Engineering (SPIE), 1985, p. 2-9.

[7] M. Bayer, P. Hawrylak, K. Hinzer, S. Fafard, M. Korkusinski, Z. R. Wasilewski, O. Stern, and A. Forchel, Science **291**, 451 (2001).

[8] K. Imamura, Y. Sugiyama, Y. Nakata, S. Muto, and N. Yokoyama, Jpn. J. Appl. Phys. 2 **34**, L1445 (1995).

[9] A. Nakajima, T. Futatsugi, K. Kosemura, T. Fukano, and N. Yokoyama, Appl. Phys. Lett. **70**, 1742 (1997).

[10] Y. Arakawa and H. Sakaki, Appl. Phys. Lett. **40**, 939 (1982).

[11] C. N. Allen, P. J. Poole, P. Marshall, J. Fraser, S. Raymond, and S. Fafard, Appl. Phys. Lett., accepted (2002).

[12] M. V. Maximovet al., Appl. Phys. Lett. **75**, 2347 (1999).

[13] A. Stintz, G. T. Liu, A. L. Gray, R. Spillers, S. M. Delgado, and K. J. Malloy, J. Vac. Sci. Technol. B **18**, 1496 (2000).

[14] B. J. Riel, K. Hinzer, S. Moisa, J. Fraser, P. Finnie, P. Piercy, S. Fafard, and Z. R. Wasilewski, J. Cryst. Growth **236**, 145 (2002).

[15] J. P. McCaffrey, M. D. Robertson, P. J. Poole, B. J. Riel, and S. Fafard, J. Appl. Phys. **90**, 1784 (2001).

[16] J. H. Davies, *The physics of low-dimensional semiconductors* (Cambridge University Press, Cambridge, 1997).

[17] S. Adachi, *Physical properties of III-V semiconductor compounds: InP, InAs, GaAs, GaP, InGaAs, and InGaAsP* (John Wiley & Sons, New York, 1992).

[18] J. A. Gupta, S. P. Watkins, E. D. Crozier, J. C. Woicik , D. A. Harrison, D. T. Jiang, I. J. Pickering, and B. A. Karlin, Phys. Rev. B **61**, 2073 (2000).

[19] K. Iga, *Handbook of Semiconductor Lasers and Photonic Integrated Circuits* (Chapman and Hall, London, 1994).

[20] *CRC Handbook of Chemistry and Physics*, 69 ed. (CRC Press, Boca Raton, Florida, 1988).

[21] I. Vurgaftman, J. R. Meyer, and L. R. Ram-Mohan, J. Appl. Phys. **89**, 5815 (2001).

[22] Y. P. Varshni, Physica A **34**, 149 (1967).

[23] S. Paul, J. B. Roy, and P. K. Basu, J. Appl. Phys. **69**, 827 (1991).

[24] J. R. Chelikowski and M. L. Cohen, Phys. Rev. B **14**, 556 (1976).

[25] A. Wojs, P. Hawrylak, S. Fafard, and L. Jacak, Phys. Rev. B **54**, 5604 (1996).

[26] K. Hinzer, *Optical Properties of GaAs-based Self-Assembled Quantum Dots and Quantum Dot Lasers, Ph.D. thesis* (University of Ottawa, 2002).

[27] S. Raymond, *Zero-Dimensional Properties of Self-Assembled Islands, Ph.D. thesis* (University of Ottawa, 1997).

[28] D. L. Aronstein and C. R. Stroud Jr., Am. J. Phys. **68**, 943 (2000).

[29] S. Fafard, R. Leon, D. Leonard, J. L. Merz, and P. M. Petroff, Phys. Rev. B **50**, 8086 (1994).

[30] M. Zinke Allmang, L. C. Feldman, and M. H. Grabow, Surf. Sci. Rep. **16**, 377 (1992).

[31] S. Fafard, Z. R. Wasilewski, and M. Spanner, Appl. Phys. Lett. **75**, 1866 (1999).

[32] H. T. Dobbs, D. D. Vvedensky, A. Zangwill, J. Johansson, N. Carlsson, and W. Seifert, Phys. Rev. Lett. **79**, 897 (1997).

[33] A. L. Barabasi, Appl. Phys. Lett. **70**, 2565 (1997).

[34] V. A. Shchukin, N. N. Ledentsov, P. S. Kop'ev, and D. Bimberg, Phys. Rev. Lett. **75**, 2968 (1995).

[35] N. N. Ledentsovet al., Phys. Rev. B **54**, 8743 (1996).

[36] V. Holy, G. Springholz, M. Pinczolits, and G. Bauer, Phys. Rev. Lett. **83**, 356 (1999).

[37] S. Fafard, Z. R. Wasilewski, C. Ni Allen, D. Picard, P. G. Piva, and J. P. McCaffrey, Superlattices Microstruct. **25**, 87 (1999).

[38] Z. R. Wasilewski, S. Fafard, and J. P. McCaffrey, J. Cryst. Growth **201-202**, 1131 (1999).

[39] W. Seifert, N. Carlsson, M. Miller, M. E. Pistol, L. Samuelson, and L. R. Wallenberg, Proc. Progress in Crystal Growth and Characterization of Materials, 1996, p. 423-471.

[40] D. Leonard, K. Pond, and P. M. Petroff, Phys. Rev. B **50**, 11687 (1994).

[41] C. W. Snyder, B. G. Orr, D. Kessler, and L. M. Sander, Phys. Rev. Lett. **66**, 3032 (1991).

[42] H. T. Dobbs, A. Zangwill, and D. D. Vvedensky, in *Surface Diffusion: Atomistic and Collective Processes*, edited by M. C. Tringides and M. Scheffler (Plenum, New York, 1997), p. 263.

[43] C. Ratsch, P. Smilauer, A. Zangwill, and D. D. Vvedensky, Surf. Sci. **329**, L599 (1995).

[44] A. Madhukar, Q. Xie, P. Chen, and A. Konkar, Appl. Phys. Lett. **64**, 2727 (1994).

[45] Y. Chen and J. Washburn, Phys. Rev. Lett. **77**, 4046 (1996).

[46] A. Madhukar, P. Chen, Q. Xie, A. Konkar, T. R. Ramachancran, N. P. Kobayashi, and R. Viswanathan, Proc. Low Dimensional Structures prepared by Epitaxial Growth or Regrowth on Patterned Substrates, NATO Advanced Workshop, Ringberg Castle, Germany, 1995, p. 19.

[47] T. R. Ramachandran, R. Heitz, P. Chen, and A. Madhukar, Appl. Phys. Lett. **70**, 640 (1997).

[48] K. H. Schmidt, G. Medeiros Ribeiro, U. Kunze, G. Abstreiter, M. Hagn, and P. M. Petroff, J. Appl. Phys. **84**, 4268 (1998).

[49] M. G. Alessi, M. Capizzi, A. S. Bhatti, A. Frova, F. Martelli, P. Frigeri, A. Bosacchi, and S. Franchi, Phys. Rev. B **59**, 7620 (1999).

[50] R. Leon and S. Fafard, Phys. Rev. B **58**, R1726 (1998).

[51] L. Jacak, P. Hawrylak, and A. Wojs, *Quantum Dots* (Springer-Verlag Berlin Germany, 1998).

[52] R. Leon, C. Lobo, A. Clark, R. Bozek, A. Wysmolek, A. Kurpiewski, and M. Kaminska, J. Appl. Phys. **84**, 248 (1998).

[53] C. Paranthoen, N. Bertru, O. Dehaese, A. Le Corre, S. Loualiche, B. Lambert, and G. Patriarche, Appl. Phys. Lett. **78**, 1751 (2001).

[54] S. Fafard, Z. R. Wasilewski, C. N. Allen, D. Picard, M. Spanner, J. P. McCaffrey, and P. G. Piva, Phys. Rev. B **59**, 15368 (1999).

[55] J. M. Garcia, T. Mankad, P. O. Holtz, P. J. Wellman, and P. M. Petroff, Appl. Phys. Lett. **72**, 3172 (1998).

[56] G. D. Lian, J. Yuan, L. M. Brown, G. H. Kim, and D. A. Ritchie, Appl. Phys. Lett. **73**, 49 (1998).

[57] H. Saito, K. Nishi, and S. Sugou, Appl. Phys. Lett. **74**, 1224 (1999).

[58] V. A. Shchukin and D. Bimberg, Reviews of Modern Physics **71**, 1125 (1999).

[59] S. Fafard, Z. R. Wasilewski, C. N. Allen, K. Hinzer, J. P. McCaffrey, and Y. Feng, Appl. Phys. Lett. **75**, 986 (1999).

[60] L. Chu, M. Arzberger, G. Bohm, and G. Abstreiter, J. Appl. Phys. **85**, 2355 (1999).

[61] H. Yasuda, F. Matsukura, Y. Ohno, and H. Ohno, Appl. Surf. Sci. **166**, 413 (2000).

[62] K. Yamaguchi, K. Yujobo, and T. Kaizu, Jpn. J. Appl. Phys. 2 **39**, L1245 (2000).

[63] N. N. Ledentsov, V. M. Ustinov, V. A. Shchukin, P. S. Kop'ev, I. Alferov Zh, and D. Bimberg, Semiconductors **32**, 343 (1998).

[64] V. G. Mokerov, Y. V. Fedorov, A. V. Guk, Y. V. Khabarov, K. S. Pak, and A. V. Danilochkin, Doklady Physics **45**, 512 (2000).

[65] A. Ohtake and M. Ozeki, Appl. Phys. Lett. **78**, 431 (2001).

[66] R. Leon, C. Lobo, J. Zou, T. Romeo, and D. J. H. Cockayne, Phys. Rev. Lett. **81**, 2486 (1998).

[67] A. Yamashiki and T. Nishinaga, J. Cryst. Growth **198-199**, 1125 (1999).

[68] M. Lopez and Y. Nomura, J. Cryst. Growth **150**, 68 (1995).

[69] T. Nishinaga, X. Q. Shen, and D. Kishimoto, J. Cryst. Growth **163**, 60 (1996).

[70] X. Q. Shen and T. Nishinaga, J. Cryst. Growth **146**, 374 (1995).

[71] A. R. Pratt, R. L. Williams, C. E. Norman, M. R. Fahy, A. Marinopoulou, and F. Chatenoud, Appl. Phys. Lett. **65**, 1009 (1994).

[72] K. R. Evans, C. E. Stutz, D. K. Lorance, and R. L. Jones, J. Vac. Sci. Technol. B **7**, 259 (1989).

[73] Q. Xie, P. Chen, and A. Madhukar, Appl. Phys. Lett. **65**, 2051 (1994).

[74] X. W. Lin, J. Washburn, Z. Liliental Weber, E. R. Weber, A. Sasaki, A. Wakahara, and Y. Nabetani, Appl. Phys. Lett. **65**, 1677 (1994).

[75] T. Saito, J. N. Schulman, and Y. Arakawa, Phys. Rev. B **57**, 13016 (1998).

[76] J. Ahopelto, H. Lipsanen, M. Sopanen, T. Koljonen, and H. M. Niemi, Appl. Phys. Lett. **65**, 1662 (1994).

[77] M. Arzberger, U. Kasberger, G. Bohm, and G. Abstreiter, Appl. Phys. Lett. **75**, 3968 (1999).

[78] H. Saito, K. Nishi, and S. Sugou, Appl. Phys. Lett. **73**, 2742 (1998).

[79] S. Fafard, Appl. Phys. Lett. **76**, 2707 (2000).

[80] K. Nishi, H. Saito, S. Sugou, and L. Jeong Sik, Appl. Phys. Lett. **74**, 1111 (1999).

[81] M. O. Lipinski, N. Y. Jin Phillipp, O. G. Schmidt, and K. Eberl, Proc. International Conference on Indium Phosphide and Related Materials, 2000, p. 215.

[82] I. Kamiya, I. Tanaka, and H. Sakaki, J. Cryst. Growth **201-202**, 1146 (1999).

[83] J. S. Lee, H. W. Ren, S. Sugou, and Y. Masumoto, J. Appl. Phys. **84**, 6686 (1998).

[84] P. J. Poole, R. L. Williams, J. Lefebvre, J. P. McCaffrey, and N. Rowell, Proc. International Conference on Indium Phosphide and Related Materials, 2000, p. 396.

[85] J. M. Garcia, G. Medeiros Ribeiro, K. Schmidt, T. Ngo, J. L. Feng, A. Lorke, J. Kotthaus, and P. M. Petroff, Appl. Phys. Lett. **71**, 2014 (1997).

[86] R. P. Mirin, J. P. Ibbetson, J. E. Bowers, and A. C. Gossard, J. Cryst. Growth **175-176**, 696 (1997).

[87] *Thermo VG Semicon.*

[88] Z. R. Wasilewski, G. C. Aers, A. J. SpringThorpe, and C. J. Miner, J. Vac. Sci. Technol. B **9**, 120 (1991).

[89] F. L. Pedrotti and L. S. Pedrotti, *Introduction to Optics* (Prentice-Hall, Englewood Cliffs, New Jersey, 1987).

[90] B. J. Riel and P. Piercy, Surf. Sci., submitted (2002).

[91] D. P. Woodruff and T. A. Delchar, *Modern Techniques of Surface Science*, 2 ed. (Cambridge University Press, 1994).

[92] A. Zangwill, *Physics at Surfaces* (Cambridge University Press, 1988).

[93] U. Sheithauer, G. Meyer, and M. Henzler, Surf. Sci. **178**, 441 (1986).

[94] Y.-N. Yang, Y. S. Luo, J. H. Weaver, L. T. Florez, and C. J. Palmstrøm, Appl. Phys. Lett. **61**, 1930 (1992).

[95] L. Daweritz and R. Hey, Surf. Sci. **236**, 15 (1990).

[96] Pashley, *in C.T. Foxon, Principles of MBE, Handbook of Crystal Growth, Thin Films and Epitaxy*, Vol. 3A (Elsevier, New-York, 1994).

[97] Q.-K. Xue, T. Hashizume, and T. Sakurai, Appl. Surf. Sci. **141**, 244 (1999).

[98] P. W. M. Blom, P. J. v. Hall, C. Smit, J. P. Cuypers, and J. H. Wolter, Phys. Rev. Lett. **71**, 3878–3881 (1993).

[99] S. Xu Qiang and T. Nishinaga, Jpn. J. Appl. Phys. 2 **32**, L1117 (1993).

[100] M. Hata, T. Isu, A. Watanabe, and Y. Katayama, J. Vac. Sci. Technol. B **8**, 692 (1990).

[101] P. B. Joyce, T. J. Krzyzewski, G. R. Bell, B. A. Joyce, and T. S. Jones, Phys. Rev. B **58**, R15981 (1998).